Nonlinear optical properties of polarized structure induced in oxide glasses(Dissertation_全文)

AUTHOR(S):

Yonezaki, Yoshinori

Nonlinear optical properties of polarized structure induced in oxide glasses

Yoshinori Yonezaki

2008

Contents

General Introduction

When an electric field is applied to a dielectric material, electric dipole moment is induced by displacing charged centers from the metastable positions, the density of which is called polarization $\mathbf{P}$. The material with nontrivial polarization (e.g. ferroelectric materials) is applicable for various electrochemical devices, such as nonvolatile storages, capacitors, actuators, gate insulation films in a field effect transistor, and so forth. The polarization induced by an external field $\mathbf{E}$ can be expressed by an expansion in a series of ascending powers of $\mathbf{E}$ as follows;

$$\mathbf{P} = \varepsilon_0(\boldsymbol{\chi}^{(1)} \cdot \mathbf{E} + \boldsymbol{\chi}^{(2)} \cdot \mathbf{E} \otimes \mathbf{E} + \boldsymbol{\chi}^{(3)} \cdot \mathbf{E} \otimes \mathbf{E} \otimes \mathbf{E} + \cdots)$$

where $\boldsymbol{\chi}^{(n)}$ is the nth-order electric susceptibility given by the (n+1)th-rank tensor. The first term in the right-side of the equation corresponds to linear polarization $\mathbf{P}_{\mathrm{L}}$ and the others to nonlinear polarization $\mathbf{P}_{\mathrm{NL}}$. $\mathbf{P}_{\mathrm{L}}$ and $\mathbf{P}_{\mathrm{NL}}$ are capable of inducing various optical (electromagnetic) effects depending on the order. One of the most popular phenomena is "refraction" mainly characterized by $\mathbf{P}_{\mathrm{L}}$. When light waves penetrate a transparent insulating medium with a finite incident angle, they change the traveling directions at the interface. This phenomenon originates in the interference between the incident light and the

Table 1 Optical phenomena caused by nonlinear optical interaction among electromagnetic waves.

Order	Phenomena	Frequencies for interaction
1	Refraction	$\omega \rightarrow \omega$
2	Second harmonic generation	$\omega + \omega \rightarrow 2\omega$
	Optical mixing	$\omega_1 \pm \omega_2 \rightarrow \omega_3$
	Parametric amplifier	$\omega_1 \rightarrow \omega_2 + \omega_3$
	Pockels effect	$\omega + 0 \rightarrow \omega$
3	Optical Kerr effect	$\omega + \omega - \omega \rightarrow \omega$
	Kerr effect	$\omega + 0 + 0 \rightarrow \omega$
	Third harmonic generation	$\omega + \omega + \omega \rightarrow 3\omega$
	Four-wave mixing	$\omega_1 + \omega_2 + \omega_3 \rightarrow \omega_4$
	DC-SHG	$\omega + \omega + 0 \rightarrow 2\omega$

stimulated radiation by $\mathbf{P}_L$. Similarly, $\mathbf{P}_{NL}$ has an ability to induce unique optical phenomena, such as amplification of optical signals, frequency conversion and a refractive-index change. A part of them is listed in Table 1. These phenomena are generically called “Nonlinear optical effects” or “Nonlinear optical phenomena”, and become central points of discussions especially in the field of optical telecommunication to meet the demands for fast processing of enormous optical signals. In the present telecommunication system, optical signals are once converted to electric ones for handling, so that the processing speed is limited by that for electric signal. To increase the processing speed, it is necessary to handle optical signals without any conversions. The nonlinear optical effect matches the purpose because notable features of the phenomena originate in interactions among electromagnetic fields. Meanwhile, these phenomena are difficult to observe under usual condition because a higher-order nonlinear optical susceptibility is essentially about nine orders smaller than the adjacent lower-order susceptibility. However, recent development of ultra-short pulsed lasers enables an extremely high photoelectric field (above 10^{18} Wcm^{-2}) to be easily available, which encourages many researchers to be engaged in the field of nonlinear optics.

The basic theory of nonlinear optical phenomena was fully established by the 1960s. The theory reveals that vector components of $\mathbf{P}_{NL}$ are restricted by structural symmetries of material. All the even-order nonlinear optical phenomena are, for example, forbidden in the medium with inversion symmetry. As will be described in detail, it is because centrosymmetric material has no odd-functional component in the potential well. This means that the polarization (asymmetric structure) is required for the appearance of even-order nonlinearity. Based on the concepts, is is found that ferroelectric single crystals represented by KH_2PO_4 (KDP), $KTiOPO_4$ (KTP), $LiNbO_3$ (LN), $LiTaO_3$ (LT), $KNbO_3$ (KN), and β-BaB_2O_4 (BBO) exhibited large optical second-order nonlinearity, and now, they are widely used as optical frequency-conversion devices. In most cases, optical device requests transparency, workability and cost performance of the preparation as well as the functionality. The single ferroelectric crystals mentioned above are exactly superior in second-order nonlinearity and transparency, however, a great deal of time and effort is required for the

preparation. In addition, there exist several conditions to be accurately satisfied for practical use (e.g. incident angle). Under such circumstance, oxide glass has attracted much attention as a promising nonlinear optical medium. Oxide glass is characterized by the high transparency in visible range and high chemical and mechanical durability if choosing a good chemical composition. It can be easily obtained in bulk form by a general melt-quenching technique, which realizes large-scale production of nonlinear optical devices. In utilizing oxide glass as nonlinear optical material, there is a serious issue that all the even-order nonlinear processes are forbidden in them because they have macroscopically isotropic structure. However, since Österberg and Marglis firstly observed the second-harmonic generation in GeO_2-SiO_2 glass fibers [1,2], many research groups have been making their efforts to induce an efficient second-order nonlinearity in a variety of oxide glasses, and it has revealed that the nonlinearity is closely related with the polarized structure induced for some reason. In 1991, Myers et al. have succeeded in encoding a large second-order nonlinearity into a fused silica plate by applying high voltage under high temperature condition [3]. The second-order nonlinearity was comparable to that for $LiNbO_3$. Afterward, Fujiwara et al. reported a large second-order nonlinearity in Ge-doped silica glasses induced by ultraviolet poling technique [4]. Nowadays, poling procedures are applied not only to silicate glasses but also to other oxide glasses. Among them, tellurite glass is a promising material from a viewpoint of application because of the low melting point, high refractive index and good infrared transmission. Tellurite glass contains tellurium dioxide (TeO_2) as a network former. The glass network is composed of the structural units with electric dipole moment, such as TeO_3 pyramidal unit, TeO_4 bipyramidal one, and so forth. The anomalous properties of tellurite glass come from a lone pair occupying an apex of the structural units. These asymmetric units are also considered to be advantageous in inducing large $\chi^{(2)}$ because polarized structure is readily achieved if they align themselves. Actually, there are some reports on second-harmonic generation in thermally/electrically poled tellurite glasses [5-11].

In the present study, polarization of isotropic tellurite glass media is attempted by two procedures. The induced polarized structure is indirectly characterized by measuring second-order nonlinearity which is closely related with the asymmetric property of electric

potential. The detailed analysis of the induced second-order nonlinearity also provides the clues for the induction mechanism. This dissertation is composed of three chapters. The first two chapters focus on the electrochemical polarization with the amorphous state remained. This procedure has an advantage that the poled glass keeps its transparency. In the third chapter, space-selective precipitation of ferroelectric crystals is worked on for inorganic oxide glasses using femtosecond laser pulses. The ideas employed in this work are expected to expand the application of glassy material. The contents of each chapter are outlined as follows.

Chapter 1 provides a theoretical background for nonlinear optical effects based on electromagnetic consideration. In section 1.1, the basic concept is explored into the stage of a quantitative evaluation of second-harmonic generation (Maker-fringe theory). In the derivation process, a spatial d-value profile is taken into account for reflecting the $\chi^{(2)}$ nonuniformity in a thermally/electrically poled sample. Using the obtained theoretical equations, optical second-order nonlinearity for a single crystalline α-quartz plate and for a thermally/electrically poled tellurite glass plate is estimated. The assumed $\chi^{(2)}$-distribution gives rise to remarkable improvement of fitting between the theory and experimental results. The agreement enables more precise estimation of the polarized area thermal/electrical poling. In section 1.2, the polarization of $15Nb_2O_5{\cdot}85TeO_2$ glass is attempted by sodium-ion doping using a conventional thermal/electrical poling setup. From the dynamic behavior of the SH intensity under high temperature conditions, it reveals that the induced polarization is mainly dominated by the ionic diffusion of the dopant ions. Although the induced second-order nonlinearity is localized beneath the anode-side surface, the magnitude of $\chi^{(2)}$ there exceeds that of α-quartz.

Chapter 2 discusses the optical encoding of second-order nonlinearity into a tellurite glass doped with transition-metal ions. Superimposed ω and 2ω beams (seeding beams) have an ability to generate a spatially oscillating DC field along with the light path. By using the interferenced seeding beams, the internal poling of the glass is examined (optical poling). In section 2.1, polarization of the vanadium-doped tellurite glass is demonstrated. The pseudo-phase-matching structure satisfied by the oscillating DC field gives rise to intense

output SH intensity. The vanadium doping further increases the output. A photochemical reaction of the vanadium ions is closely related with the output enhancement.

In section 2.2, the influence of V, Tb co-doping on the output SH intensity is investigated focusing on a Nb_2O_5-TeO_2 glass. The optically poled sample shows Tb-amount dependence of SH intensity only when vanadium ions coexist. The dependency shows that terbium ions serve as a trap center for the charged species generated at vanadium ions.

Chapter 3 presents experimental results on space-selective precipitation of ferroelectric crystals inside oxide glasses using a near-infrared femtosecond pulsed laser. When Na_2O-BaO-TiO_2-SiO_2 and Li_2O-Nb_2O_5-SiO_2 glasses are irradiated with tightly focused laser-pulses with extremely short duration, polycrystalline $BaTiO_3$ and $LiNbO_3$ appear, respectively. Because they have large second-order nonlinearity, the blue emission, corresponding to the SHG of the incidence, is observed in response to the precipitation. Electron probe microanalysis in the vicinity of the focal point reveals that the laser irradiation allows the radial migration of glass-constituting cations resulting in a ring-shaped precipitated area involving polycrystalline phases.

Finally, the central results and discussion through the whole of this thesis are summarized in the summary section.

References

[1] Y. Sasaki, Y. Ohmori, Appl. Phys. Lett., 39 (1981) p. 466.

[2] U. Österberg and W. Margulis, Opt. Lett., 11 (1986) p. 516.

[3] R. A. Myers, N. Mukherjee, S. R. J. Brueck, Opt. Lett., 16 (1991) p. 1732.

[4] T. Fujiwara, M. Takahashi, and A. J. Ikushima, Appl. Phys. Lett., 71 (1997) p. 1032.

[5] K. Tanaka, K. Kashima, K. Hirao, N. Soga, A. Mito, and H. Nasu, Jpn. J. Appl. Phys., Part 2, 32 (1993) L843.

[6] K. Tanaka, K. Kashima, K. Kajihara, K. Hirao, N. Soga, A. Mito, and H. Nasu, Proc.SPIE, 2289 (1994) p. 167.

[7] K. Tanaka, K. Kashima, K. Hirao, N. Soga, A. Mito, and H. Nasu, J. Non-Cryst. Solids, 185 (1995) p. 123.

[8] K. Tanaka, A. Narazaki, K. Hirao, and N. Soga, J. Appl. Phys., 79 (1996) p. 3798.

[9] K. Tanaka, A. Narazaki, K. Hirao, and N. Soga, J. Non-Cryst. Solids, 203 (1996) p. 49.

[10] A. Narazaki, K. Tanaka, K. Hirao, and N. Soga, J. Appl. Phys., 83(1998) p. 3986.

[11] A. Narazaki, K. Tanaka, K. Hirao, and N. Soga, J. Am. Ceram. Soc., 81 (1998) p. 2735.

Chapter 1 Polarized structure induced by thermal/electrical procedure

1.1 Basic concept of nonlinear optics and theoretical equations for $\chi^{(2)}$ characterization

Nonlinear optical effects are regarded as the interaction between photons via $\mathbf{P}_{NL}$ induced in a material. The first part of this chapter provides a fundamental concept of nonlinear optical physics on the basis of electromagnetic consideration.

1.1.1 Theory

Origin of nonlinear optical phenomena

When an electric field is applied to a dielectric material, dipole moment is induced by displacing charged centers from the metastable positions, the density of which is called "polarization". Macroscopic polarization is mainly composed of the next three contributions;

i) Electronic polarization due to elastic deformation of electron cloud.

ii) Ionic polarization due to elastic deformation of ionic bond lengths or angles.

iii) Orientational polarization due to inelastic deformation of permanent dipole moments.

Each component has the characteristic resonant frequencies where the polarization cannot follow the field alternation. Therefore, the real part of macroscopic dielectric constant shows frequency dependence as shown in Fig. 1.1. Consider the case when visible or near-infrared light is incident. Because the frequencies lie far above those characteristic for lattice vibrations, electrons are the only charged centers which can follow the oscillating field. Therefore, our interest is limited to electronic polarization.

Let E_a be the average electric field experienced by an electron weakly bound to the nucleus and nearby electrons, and E the externally applied field. E_a is estimated to be in

the order of 10^9 V/cm from

$$E_{\mathrm{a}} = \frac{1}{4\pi\varepsilon_0}\frac{e}{a_0^2}, \tag{1.1}$$

where e is the elementary electric charge, ε_0 the dielectric constant of vacuum, and a_0 the Bohr radius. Because E must be much smaller than E_{a} due to the restriction of a dielectric breakdown, the macroscopic polarization can be expressed by an expansion in a series of ascending powers of E about E_{a}, as shown in general introduction. Considering Eq. 1.2, it is clear that P_{NL} originates in the deviation from a harmonic potential about E (or displacement from the metastable position, x).

$$P = \frac{\partial U}{\partial E}, \tag{1.2}$$

where U is the electrostatic potential. Because P is presented by the expansion about E_{a}, the nth-order nonlinear optical susceptibility $\chi^{(\mathrm{n})}$ decreases by a factor of E/E_{a} as n increases. Then, the $\chi^{(\mathrm{n})}$ is related with the adjacent lower-order susceptibility as follows;

$$\chi^{(\mathrm{n})} \approx \frac{\chi^{(\mathrm{n\text{-}1})}}{E_{\mathrm{a}}} \tag{1.3}$$

Consequently, brilliant nonlinear optical effects due to $\mathbf{P}_{\mathrm{NL}}^{(\mathrm{n})}$ become observable only when a very strong field strength, like an extremely high power laser, is applied.

Nonlinear electromagnetic interactions inside materials

Planar lightwaves travel inside a transparent (no dispersion) isotropic medium to satisfy the propagation-equation given by

$$\nabla\times\nabla\times\mathbf{E}_{\omega} + \frac{n^2}{c^2}\frac{\partial^2\mathbf{E}_{\omega}}{\partial t^2} = -\mu\frac{\partial^2\mathbf{P}_{\mathrm{NL}\omega}}{\partial t^2}, \tag{1.4}$$

where n and μ are the linear refractive index and the magnetic permeability of the medium, respectively. The parameter c is the speed of light in vacuum. $\mathbf{E}_{\omega}$ and $\mathbf{P}_{\mathrm{NL}\omega}$

are an external electric field and nonlinear polarization, respectively. The propagation-equation is constructed for each frequency in consideration. Equation 1.4 indicates that the oscillating nonlinear polarization becomes the source of the electromagnetic wave with the same frequency. In order to solve the equations, it is necessary to obtain the expression P_{NL} for the frequency in interesting.

The frequencies interacting with incident ω_1 and ω_2 light through $\mathbf{P}^{(2)}$ are derived by inserting Eqs. 1.5 and 1.6 into Eq. 1.7.

$$\mathbf{E}(t)_{\omega_1} = \mathbf{E}_{\omega_1 0}\left\{\exp(i(\mathbf{k}_{\omega_1}\cdot\mathbf{r}-\omega_1 t))+\mathrm{c.c.}\right\} \tag{1.5}$$

$$\mathbf{E}(t)_{\omega_2} = \mathbf{E}_{\omega_2 0}\left\{\exp(i(\mathbf{k}_{\omega_2}\cdot\mathbf{r}-\omega_2 t))+\mathrm{c.c.}\right\} \tag{1.6}$$

$$\mathbf{P}^{(2)} = \boldsymbol{\chi}^{(2)}\cdot\mathbf{E}\otimes\mathbf{E} \tag{1.7}$$

$\mathbf{k}_{\omega_n}$, $\mathbf{r}$, and t are the wave vector for ω_n, space coordinates and time, respectively. The substitution clarifies that $\mathbf{P}^{(2)}$ has the frequencies of $\omega_1+\omega_2$ and $\omega_1-\omega_2$, which means that when ω_1 and ω_2 beams are incident into a nonlinear material, $\omega_1+\omega_2$ and $\omega_1-\omega_2$ waves are generated as a result of $\mathbf{P}^{(2)}$-interaction.

Next, we consider the output intensity of the synthesized $\omega_3(=\omega_1+\omega_2)$ beam when ω_1 and ω_2 beams are normally incident into a flat medium. It is assumed that z-axis is taken in the propagating direction, and the ω_3 beam is polarized along x-direction in Cartesian coordinate. Electric-field components $\mathbf{E}_{\omega_3}:(E_{\omega_3,\mathrm{x}},E_{\omega_3,\mathrm{y}},E_{\omega_3,\mathrm{z}})$ is then represented by

$$E_{\omega_3,\mathrm{x}} = E_{\omega_3}(z)\exp\left\{i(k_{\omega_3}z-\omega_3 t)\right\}, \tag{1.8}$$

$$E_{\omega_3,\mathrm{y}} = E_{\omega_3,\mathrm{z}} = 0. \tag{1.9}$$

From Eqs. 1.4, 1.8 and 1.9, we obtain the next differential equation.

$$\frac{\partial E_{\omega_3}}{\partial z} = \frac{i\chi_{\text{eff}}^{(2)}\omega_3^2}{4k_{\omega_3}c^2} E_{\omega_1}(z)E_{\omega_2}(z)\exp(i\Delta kz) \tag{1.10}$$

$$\Delta k = k_{\omega_1} + k_{\omega_2} - k_{\omega_3}, \tag{1.11}$$

where $\chi_{\text{eff}}^{(2)}$ is an effective second-order susceptibility in which three-dimensional information of $\boldsymbol{\chi}^{(2)}$ is contracted. By integrating Eq. 1.10 in the dimension of the medium thickness L, the output intensity of the generated sum-frequency wave I_{ω_3} is obtained as follows.

$$I_{\omega_3} = \frac{\omega_3^2 \chi_{\text{eff}}^{(2)^2} I_{\omega_1} I_{\omega_2} L^2}{8\varepsilon_0 n_{\omega_1} n_{\omega_2} n_{\omega_3} c^3} \text{sinc}^2\left(\frac{\Delta kL}{2}\right) \tag{1.12}$$

When only ω lightwave is incident ($\omega_1 = \omega_2$), $P^{(2)}$ is given by the sum of the static component and the 2ω oscillating component. The former corresponds to optical rectification (OR) and the latter to second-harmonic generation (SHG). By transforming Eq. 1.12, the output second-harmonic (SH) intensity is obtained as follows:

$$I_{2\omega} = \frac{2\omega^2 d_{\text{eff}}{}^2 I_\omega^2 L^2}{\varepsilon_0 n_\omega^2 n_{2\omega} c^3} \text{sinc}^2\left(\frac{\Delta kL}{2}\right) \tag{1.13}$$

Here, d_{eff} is an effective second-order nonlinear coefficient (or effective d-value). The d-value is used only when Kleinman symmetry condition is satisfied. It is related with $\chi_{\text{eff}}^{(2)}$ as follows.

$$d_{\text{eff}} = \frac{\chi_{\text{eff}}^{(2)}}{2} \tag{1.14}$$

Since an electric field and polarization have vector character, second-order nonlinearity is represented by third-rank tensor **d** with 27 components. However, d_{ijk} and d_{ikj} are inseparable, therefore, d-tensor is generally contracted to 3×6 matrix d_{il}. Response of subscript i and l to Cartesian coordinate is shown in Table 1.1. The contracted notation

reduces the number of independent component to 18 (Eq. 1.15). The independent components are further reduced by the symmetries of the material in interest. In the next part, a brief description about the relation is provided.

$$\begin{pmatrix} P_{\mathrm{x}}^{(2)} \\ P_{\mathrm{y}}^{(2)} \\ P_{\mathrm{z}}^{(2)} \end{pmatrix} = \begin{pmatrix} d_{11} & d_{12} & d_{13} & d_{14} & d_{15} & d_{16} \\ d_{21} & d_{22} & d_{23} & d_{24} & d_{25} & d_{26} \\ d_{31} & d_{32} & d_{33} & d_{34} & d_{35} & d_{36} \end{pmatrix} \begin{pmatrix} E_{\mathrm{x}}^{\ 2} \\ E_{\mathrm{y}}^{\ 2} \\ E_{\mathrm{z}}^{\ 2} \\ E_{\mathrm{y}}E_{\mathrm{z}} \\ E_{\mathrm{z}}E_{\mathrm{x}} \\ E_{\mathrm{x}}E_{\mathrm{y}} \end{pmatrix} \tag{1.15}$$

Table 1.1 Notation conversion of subscripts in second-order nonlinear susceptibility d_{il}.

	1	2	3	4	5	6
i	x	y	z	-	-	-
l	xx	yy	zz	yz(zy)	zx(xz)	xy(yx)

Structural symmetry and association rule for d-tensor components

Because polarization and applied electric fields have directional character, they are given by vectors in Cartesian coordinate system. Each component of $\mathbf{P}^{(2)}$ is derived from

$$P_{\mathrm{i}}^{(2)} = \sum_{\mathrm{j,k}} \sum_{\omega_{\mathrm{m}},\omega_{\mathrm{n}}} \chi_{\mathrm{ijk}}^{(2)} E_{\omega_{\mathrm{m}}\mathrm{j}} E_{\omega_{\mathrm{n}}\mathrm{k}} \,. \tag{1.16}$$

As is clear from Eq. 1.16, $\boldsymbol{\chi}^{(2)}$ includes 27 (= 3^3) components. However, the symmetric character of a target material associates or nulls some of them [1]. Here, let us introduce a new Cartesian coordinate frame (α, β, γ) which is related with the initial Cartesian frame (i, j, k) by an arbitrary combination of rotation and inversion symmetry transformation $\mathbf{A}$ (3×3 matrix). The $\chi^{(2)}$-component $\chi_{\alpha\beta\gamma}^{(2)}$ in the new frame are then described with $\mathbf{A}$ that

$$\chi_{\alpha\beta\gamma}^{(2)\prime} = \sum_{\mathrm{i,j,k}} A_{\alpha\mathrm{i}} A_{\beta\mathrm{j}} A_{\gamma\mathrm{k}} \chi_{\mathrm{ijk}}^{(2)} \,, \tag{1.17}$$

where prime means the expression in the new frame. If operation **A** is allowed in the space group of a concerned medium, $\boldsymbol{\chi}^{(2)}_{\alpha\beta\gamma}{}'$ remains unchanged in both coordinate frames so that

$$\chi^{(2)}_{\alpha\beta\gamma}{}' = \chi^{(2)}_{\alpha\beta\gamma}, \tag{1.18}$$

because physical quantities observed before and after the operation should be unchanged. From the Eqs. 1.17 and 1.18, the extinction or association rule for $\chi^{(2)}_{\mathrm{ijk}}$s can be obtained. For example, when a target material has centrosymmetric structure (inversion symmetric operation is allowed), Eq. 1.17 is transformed to

$$\chi^{(2)}_{\alpha\beta\gamma}{}' = \sum_{\mathrm{i,j,k}} (-\delta_{\alpha\mathrm{i}})(-\delta_{\beta\mathrm{j}})(-\delta_{\gamma\mathrm{k}})\chi^{(2)}_{\mathrm{ijk}} \,. \tag{1.19}$$

Using Eqs. 1.18 and 1.19, the next equation is provided which works out in all the material with inversion symmetry,

$$\chi^{(2)}_{\alpha\beta\gamma} = -\chi^{(2)}_{\alpha\beta\gamma} \,. \tag{1.20}$$

This equation shows that $\chi^{(2)}_{\mathrm{ijk}}$, namely, second-order polarization $P^{(2)}_{\mathrm{i}}$ becomes zero (Similarly, even-order nonlinear susceptibilities also become zero.), and that any second-order nonlinear optical phenomena are forbidden in a macroscopically centrosymmetric medium. This property is also understood from the viewpoint of potential-energy change against electron displacement. As shown in Eq. 1.2, the 2*n*th-order nonlinear polarizations originates in the (2*n*+1)th-order E term in the electrostatic potential. However, centrosymmetric materials should not have an odd-functional component in its potential. This is because the media with inversion symmetry exhibit no even-order nonlinear polarization.

d-component evaluation for transparent material; Maker-fringe method

The tensor components of **d** can be evaluated by monitoring the incident-angle dependence of SH intensity (Maker-fringe method) because incident angle θ affects the interactive length, the propagating direction, and the magnitude of effective second-order nonlinearity. This part provides visceral explanation for the Maker-fringe method.

Let it be assumed that an intense laser beam is incident into a medium with an angle θ. The intensity of SH wave can be calculated by considering the contributions from $P^{(2)}$ induced at each point of the light path [1]. When an incident field is given by Eq. 1.5, 2ω-component of $P^{(2)}$ satisfies the next equation.

$$P_{2\omega}^{(2)} \propto \sin(2k_{\omega}x - 2\omega t) \tag{1.21}$$

It is found from the equation that the source of SH wave is spatially dominated by k_{ω} (namely, the wave vector of the incidence). Then, the generated wave is called “bound harmonic wave”, as compared with “free harmonic wave” which is spatially dominated by $k_{2\omega}$. Because the intensity of the free harmonic wave is much weaker than the bound harmonic wave, the contribution from the free harmonic wave can be ignored. When an incident plane wave propagates an infinite-sheet medium with thickness L as illustrated in Fig. 1.2, the contribution from $P_{2\omega}^{(2)}$ at a slab $\mathrm{d}x$ to output harmonic field at the exit surface $\mathrm{d}E_{2\omega}$ is provided by

$$\mathrm{d}E_{2\omega} \propto \sin\{2k_{\omega}\cos\alpha \cdot x - 2\omega(t - t')\}\mathrm{d}x \tag{1.22}$$

where t' is the period for the harmonic radiation generated at the slab arriving at the exit face.

$$t' = \frac{\dfrac{L}{\cos\theta_{2\omega}} - x}{v_{2\omega}} = \frac{k_{2\omega}}{2\omega}\left(\frac{L}{\cos\theta_{2\omega}} - x\right) \tag{1.23}$$

$v_{2\omega}$ is the phase velocity of the SH wave in the medium. From these equations, the total

harmonic field is available as follows.

$$E_{2\omega} = \int_0^{\frac{L}{\cos\theta_{2\omega}}} \mathrm{d}E_{2\omega} \propto \frac{L}{\cos\theta_{2\omega}} \frac{\sin\Psi}{\Psi}, \tag{1.24}$$

where

$$\Psi = \frac{L}{2}\frac{4\pi}{\lambda_\omega}\left(n_\omega \cos\theta_\omega - n_{2\omega}\cos\theta_{2\omega}\right). \tag{1.25}$$

λ_ω means the wavelength of the incident beam in vacuum. n_ω and $n_{2\omega}$ are the refractive indices for ω and 2ω beams, respectively. In the case of normal incidence, Eq. 1.25 is transformed to

$$E_{2\omega} = \int_0^L dE_{2\omega} \propto \frac{\lambda_\omega}{(n_\omega - n_{2\omega})} \sin\left\{\frac{L}{2}\frac{4\pi}{\lambda_\omega}(n_\omega - n_{2\omega})\right\}. \tag{1.26}$$

From the comparison of Eqs. 1.13 and 1.26, the output SH intensity $I_{2\omega}$ is as in Eq. 1.27.

$$I_{2\omega} = \frac{\omega^2 \chi_{\mathrm{eff}}^{(2)^2} I_\omega^2 L^2}{2\varepsilon_0 n_\omega^2 n_{2\omega} c^3 \cos^2\theta_{2\omega}} \frac{\sin^2\Psi}{\Psi^2}. \tag{1.27}$$

Equation 1.27 shows that $I_{2\omega}$ oscillates with θ increasing. This oscillation was firstly observed for α-quartz, and since then, known as Maker fringes after the discoverer [2]. The magnitude and the period of the oscillation reflect d_{eff} and the thickness of SHG-active region. Therefore, the d-tensor components can be evaluated by analyzing Maker-fringe pattern circumstantially. Equation 1.27 is modified for practical use as

$$I_{2\omega} = \frac{2\omega^2 d_{\mathrm{eff}}^2}{\varepsilon_0 n_\omega^2 n_{2\omega} c^3 \cos^2\theta_\omega} I_\omega^2 t_\omega(\theta)^4 T_{2\omega}(\theta) R(\theta) B(\theta) L^2 \left(\frac{\sin\Psi}{\Psi}\right)^2, \tag{1.28}$$

where $t_\omega(\theta)$ and $T_{2\omega}(\theta)$ comprise the Fresnel transmission factors for a fundamental and the SH waves, respectively. $R(\theta)$ represents the multiple reflection coefficient, and B is the beam-size correction factor. Maker-fringe pattern is formed by the multiplication of a fringe part and an envelope function. The former is mainly dominated by L/l_c, $n_\omega - n_{2\omega}$ and the spatial profile of d-value, and the latter by the magnitude of d_{il} and other correction

factors. Other important information derived from the Maker-fringe pattern is discussed later. The setup for measuring Maker-fringe pattern is described in the experimental part of section 1.2.

Thermal/electrical poling treatment

As described previously, SHG is forbidden in amorphous media, so electrostatic asymmetry has to be induced for adding second-order nonlinearity. An easy way to do that is "poling" operation which is literally an operation to induce polarized structure by using an electric field. In section 1.2, thermal/electrical poling is attempted for a tellurite glass sample. In thermal/electrical poling, a large voltage is applied to a medium under a raised temperature. Since glass matrix becomes flexible under high temperature, polarized structure can be easily induced by electric field. The induced structure is frozen-in by cooling down with the voltage maintained. The induced structure is metastable under room temperature because the thermal energy is not enough for the relaxation of the induced structure.

In uniaxially poled material (e.g. thermally/electrically poled glass), second-order nonlinear tensor **d** is expressed with only one independent component due to its anisotropy ($C_{\infty v}$ symmetry) as follows.

$$\mathbf{d} = \begin{pmatrix} \bullet & \bullet & \bullet & \bullet & 2d_{31} & \bullet \\ \bullet & \bullet & \bullet & 2d_{31} & \bullet & \bullet \\ d_{31} & d_{31} & 3d_{31} & \bullet & \bullet & \bullet \end{pmatrix} \tag{1.29}$$

When SHG measurement is carried out under *pp*-polarization condition, d_{eff} is given by Eq. 1.30.

$$\begin{aligned} d_{\text{eff}} &= 2d_{31}\sin\theta_{\omega}\cos\theta_{\omega}\cos\theta_{2\omega} + (d_{31}\cos^2\theta_{\omega} + d_{33}\sin^2\theta_{\omega})\sin\theta_{2\omega} \\ &= d_{31}(2\sin\theta_{\omega}\cos\theta_{\omega}\cos\theta_{2\omega} + \cos^2\theta_{\omega} + 3\sin^2\theta_{\omega}\sin\theta_{2\omega}) \end{aligned} \tag{1.30}$$

1.1.2 Validity of Maker-fringe equations

Introduction

The previous part dealt with Maker-fringe method as a general method for quantifying d-value. In this part, focusing on α-quartz and thermally/electrically poled $15Nb_2O_5 \cdot 85TeO_2$ glass, it is checked whether the theoretical Maker-fringe curve shows good agreement with the actual angle dependence of SH intensity data. The α-quartz is a commonly used standard for evaluating d-value. Therefore, the degree of agreement between the theoretical pattern and α-quartz data is regarded as an indicator of the validity. The thermally/electrically poled $15Nb_2O_5 \cdot 85TeO_2$ glass is a sample treated in the whole part of this thesis. Because the nonlinearity is not uniform within the poled sample, it is required to check whether the Maker-fringe equation is applicable for the poled material or not. In the last half of this part, the Maker-fringe equation is modified to be applicable for both crystals and poled materials.

Experimental

· Sample preparation

α-quartz

A commercially-available Y-cut α-quartz plate with the thickness of 1.046 mm was used. The α-quartz is a low-temperature form of SiO_2 polymorph. For α-quartz, coordinate axes are conventionally taken as in Fig. 1.4. The space group ($P3_121$, No. 152, D_3^4) makes its d-tensor components as in the following:

$$\mathbf{d} = \begin{pmatrix} d_{11} & -d_{11} & 0 & d_{14} & 0 & 0 \\ 0 & 0 & 0 & 0 & -d_{14} & -2d_{11} \\ 0 & 0 & 0 & 0 & 0 & 0 \end{pmatrix} \tag{1.31}$$

The independent components are well-known; $d_{11} = 0.335$ pm/V and $d_{14} = 6.67 \times 10^{-3}$ pm/V. "Y-cut" means that the α-quartz plate is sliced so as the surfaces perpendicular to y-axis to

emerge.

Thermally/electrically poled $15Nb_2O_5 \cdot 85TeO_2$ glass

A precursor glass with $15Nb_2O_5 \cdot 85TeO_2$ composition in molar ratio was prepared from reagent-grade Nb_2O_5 (purity 99.9 %) and TeO_2 (purity 99.9 %) powder. The raw materials were mixed thoroughly, and melted in a platinum crucible at 850 ˚C for 15 min in air. The melt was poured into a mold made of graphite and cooled to room temperature. The glass thus obtained was annealed for 15 min at 400 ˚C, 20 ˚C higher than its glass transition temperature determined from differential thermal analysis (Fig. 1.5), and cut into a plate by means of a saw pasted with diamond powder. The surfaces were polished to obtain a rectangular plate 1.00 mm thick. The polished was thermally/electrically poled with the procedure explained in the next section.

Thermal/electrical poling

Figure 1.6 shows a schematic illustration of the thermal/electrical poling apparatus. After cleaning the surfaces with ethanol, a glass sample was sandwiched in between two commercially available sodium borosilicate cover glasses 0.15 mm thick, and contacted with electrodes made of stainless steel. The set sample was heated to an aimed temperature (235-300 ˚C) in an electric furnace, and then, the voltage of 3 kV was applied for 15 min with raised temperature kept constant. After the sample was cooled to room temperature, the voltage was removed. It should be noted that the actual voltage applied to the sample was less than 3 kV because of the cover glasses. The point group and d-tensor representation for an uniaxially poled glass is already discussed.

· Optical absorption spectroscopy

To evaluate the attenuation effects for relevant electromagnetic waves, the optical absorption spectrum in the visible range was measured for the thermally/electrically poled $15Nb_2O_5 \cdot 85TeO_2$ glass samples at room temperature using a spectrophotometer Hitachi 330.

· Complex refractive index

For α-quartz, ordinary index n_o and extraordinary index n_{eo} are known to be 1.534143 and 1.542931 for 1064 nm, and 1.546857 and 1.556102 for 532 nm. These values were used for making a theoretical Maker-fringe pattern. For the $15Nb_2O_5 \cdot 85TeO_2$ glass, the corresponding values have not been reported yet. Therefore, ellipsometry was attempted at room temperature. Data collection was performed in reflection mode using a high precision goniometer-spectrometer system M-2000, Woollam. For avoiding the backside reflection, one surface of the sample was blackened with a permanent marker. The Stokes parameters Ψ and Δ were measured across the UV-vis wavelength range (250-700 nm) with incident angle fixed at 74.5°. The measured Ψ and Δ were converted to complex refractive indices using Gaussian oscillator model which involves the contribution from strongly inhomogeneous broadening.

· SHG measurement

Angle dependence of SH intensity was measured using a Maker-fringe configuration [3] shown in Fig. 1.7. As an incident light, *p*-polarized fundamental wave of a pulsed neodymium-doped yttrium-alminum-garnet (Nd:YAG) laser (Spectra Physics, GCR-11), which operated in a Q-switched mode with 10 Hz repetition rate, was used. The average laser power was 600 mW. The transmitted *p*-polarized SH wave generated in a sample was detected with a photomultiplier connected to a monochromator (Hamamatsu Photonics, R955) after passing through IR-cut filters. Rotation axis was z-axis for the α-quartz, and the direction perpendicular to the polarized direction for the poled glass samples.

Results

· Optical absorption spectrum for thermally/electrically poled $15Nb_2O_5 \cdot 85TeO_2$ glass plate

Optical absorption spectrum for the poled $15Nb_2O_5 \cdot 85TeO_2$ glass sample is shown in Fig. 1.8. All the poled samples showed similar spectra regardless of the poling temperature. The optical absorption spectra assure sufficient transparency at the vis-IR wavelengths longer

than 450 nm. Accordingly, there is no problem to apply the Maker-fringe equations for the evaluation of second-order nonlinearity.

· Complex refractive index

The result of ellipsometry is shown in Fig. 1.9. The above diagram (a) presents the measured Stokes parameters Ψ and Δ, and the below (b) is the simulated dispersion for the complex refractive index $n + ik$. The obtained values were used for making a theoretical Maker-fringe pattern.

· Maker-fringe pattern

Figure 1.10 shows the Maker-fringe patterns for the α-quartz (a) and the $15Nb_2O_5 \cdot 85TeO_2$ glass sample poled at 290 ˚C (b). The dashed line drawn in the figure is the fitted theoretical pattern derived from Eq. 1.28. The α-quartz exhibits a few fringes in response to the increase in incident angle. The actual data is well duplicated by the theoretical pattern within the margin of error. As for $15Nb_2O_5 \cdot 85TeO_2$ glass, although the poling process makes the sample SHG-active, no fringe is seen in the pattern. With increasing incident angle, SH intensity increases, shows a peak top, and then decreases. The whole pattern shapes were not so different among the poled samples regardless of the poling temperature. For the poled samples, the theoretical pattern does not agree well with the actual SH intensity data. The theoretical pattern shows a steep increase at lower angle than the experimental data. Because the SH intensity diminished after polishing out the anode-side surface by a few tens of microns, the induced second-order nonlinearity was found to be localized at around the anode-side surface.

Discussion

i) α-quartz

Clear fringes are recognized in the Maker-fringe pattern. These fringes originate in the elongation of $P^{(2)}$-interactive length in response to the increase in incident angle. A fast

elongation is expected for such materials in which non-zero d-value sprawls over a distance much longer than the coherent length l_c (Fig. 1.11(a) and (b)). In α-quartz, l_c is calculated to be 41.840 μm under the condition of vertical incidence, which is much less than the sample thickness L. The large L/l_c gives rise to the appearance of many fringes.

Since the actual data is sufficiently duplicated by a theoretical pattern derived with the given parameters, Maker-fringe theory is considered to be valid for the α-quartz.

ii) Thermally/electrically poled $15Nb_2O_5 \cdot 85TeO_2$ glass

As opposed to α-quartz, no fringe is seen in the Maker-fringe patterns for thermally/electrically poled $15Nb_2O_5 \cdot 85TeO_2$ glasses. The absence of fringes implies that $P^{(2)}$-interaction was localized at around the anode-side surface, as shown in the Fig. 1.11(c) or (d). Such localization is clearly different from the case of α-quartz in which the whole region is $P^{(2)}$-active. The disagreement between the experimental data and the theoretical also comes from the inhomogeneous d-value profile. Originally, Eq. 1.28 assumes a homogeneous medium with a step d-value profile. According to Myers et al., SHG-active region induced by thermal/electrical poling is inhomogeneously located only beneath the anode-side surface [4]. Therefore, an appropriate profile should be taken into account for the analysis. Proctor et al. [5] simulate a charge distribution and the corresponding electric field profile inside a voltage-applied glass plate by assuming mobile cations and immobile anions. This model provides for rapid changes in $\mathbf{E}_{dc}$ at each end of the sample. In addition, the magnitude of $\mathbf{E}_{dc}$ is much larger at the anode-side surface than at the cathode-side surface. This result is not inconsistent with the fact that the nonlinearity is only observed on the anode-side surface. Therefore, it is appropriate to assume a similar field distribution or a spatially decaying distribution of d-value for thermally/electrically poled materials. In the present case, based on the results of Myers et al. and Proctor et al., an exponentially decay profile (Eq. 1.32, Fig. 1.11 (d)) is employed for expressing the inhomogeneous distribution.

$$d_{\text{eff}} = d_{\text{eff}}(0)\exp(-\gamma x) \tag{1.32}$$

$d_{\mathrm{eff}}(0)$ and γ^{-1} are hypothetical d-value at the anode-side surface and a characteristic length of spatial d-value decay which is an indicator of SHG-active layer thickness, respectively. The theoretical Maker-fringe pattern is then modified as follows:

$$I_{2\omega} = \frac{2\omega^2 \left[d_{\mathrm{eff}}(0)\right]^2 {I_\omega}^2}{\varepsilon_0 {n_\omega}^2 n_{2\omega} c^3} \exp(-\alpha L') \times \frac{1 + \exp(2\delta L') - 2\exp(\delta L')\cos(\Delta k L')}{\delta^2 + (\Delta k)^2}$$
$$L' = \frac{L}{\cos\theta_{2\omega}} \qquad (1.33)$$
$$\delta = \frac{\alpha}{2} - \gamma$$

where α is the absorption coefficient at 2ω frequency. When $\gamma = 0$, Eq. 1.33 is equivalent with Eq. 1.28. By fitting Eq. 1.33 to the experimental data, it is possible to determine $d_{\mathrm{eff}}(0)$ and γ^{-1}. The $d_{\mathrm{eff}}(0)$ is converted to $d_{33}(0)$ with the next equation when the sample with $C_{\infty \mathrm{v}}$ symmetry is rotated on an axis perpendicular to the symmetric axis.

$$d_{\mathrm{eff}}(x) = \frac{2}{3} d_{33}(x) \sin\theta_\omega \cos\theta_\omega \cos\theta_{2\omega} + d_{33}(x)\left(\frac{1}{3}\cos^2\theta_\omega + \sin^2\theta_\omega\right)\sin\theta_{2\omega} \quad (1.34)$$

Because $d_{\mathrm{eff}}(0)$ gives rise to the confusion due to the incident angle dependency, $d_{33}(0)$ is used as a measure of the induced second-order nonlinearity from here. The fitting curve obtained from the modified equation is provided in Fig. 1.10(b) with the dotted line. In making the theoretical pattern, the optical absorption at ω and 2ω was ignored. The gentle increase in SH intensity is well given by the modified pattern. The good agreement shows that the d-value distribution presented by Eq. 1.32 is more realistic.

Conclusion

In this part, a general concept of nonlinear optics, especially of second-order nonlinear interactions, is briefly explained from the viewpoint of electromagnetics. By associating with geometrical consideration, the classical wave equations are expanded to a general Maker-fringe equation, which well duplicates the incident angle dependence of

second-harmonic intensity generated in a uniform medium. However, the fringe theory does not work in inhomogeneously $\chi^{(2)}$-distributing media. For such case, the Maker-fringe equation is appropriately modified by building the d-value distribution onto the classical wave equations.

References in Section 1.1

[1] P. A. Franken and J. F. Ward, Rev. Mod. Phys., 35 (1963) p. 23.

[2] P. D. Maker, R. W. Terhune, M. Nisenoff, and C. M. Savage, Phys. Rev. Lett., 8 (1962) p. 21.

[3] J. Jerphagnon and S. K. Kurtz, J. Appl. Phys., 41 (1970) p. 1667.

[4] R.A. Myers, N. Mukherjee, and S. R. J. Brueck, Opt. Lett., 16 (1991) p. 1732.

[5] T. M. Proctor, Paul M. Sutton, J. Am. Ceram. Soc., 43 (1960) p. 173.

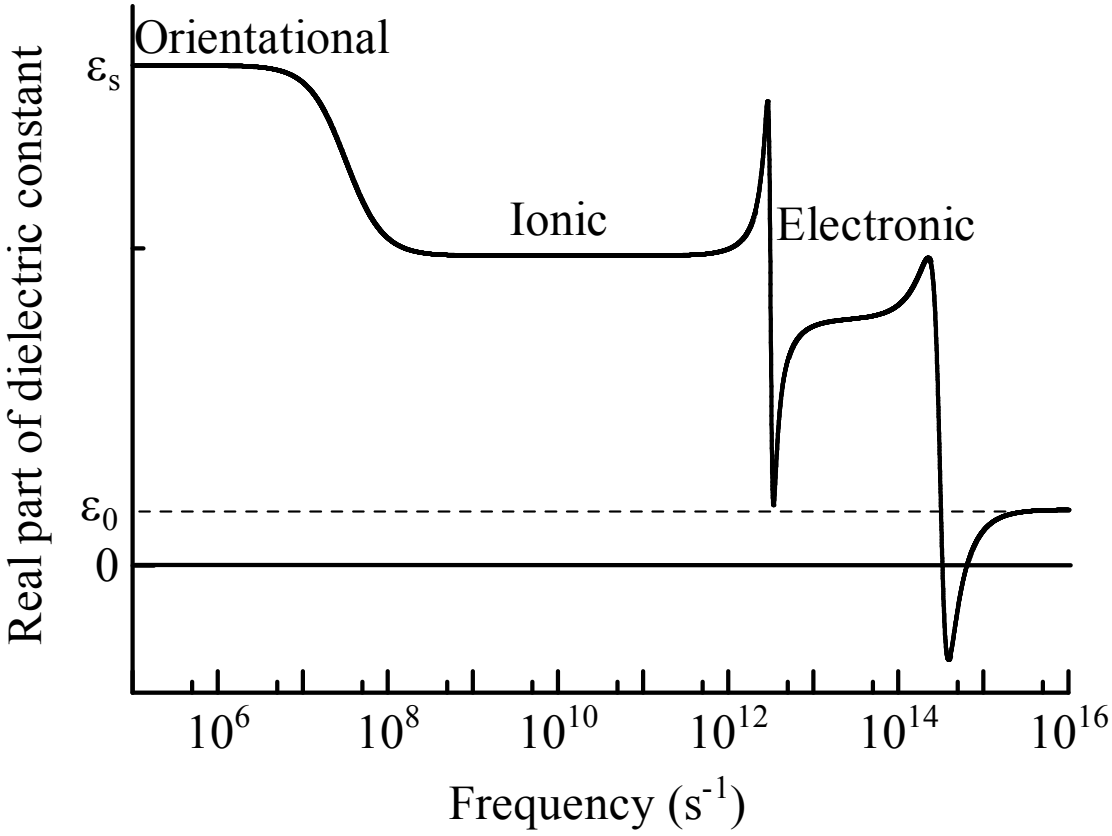

Figure 1.1 Frequency dependence of real part in complex dielectric constant.

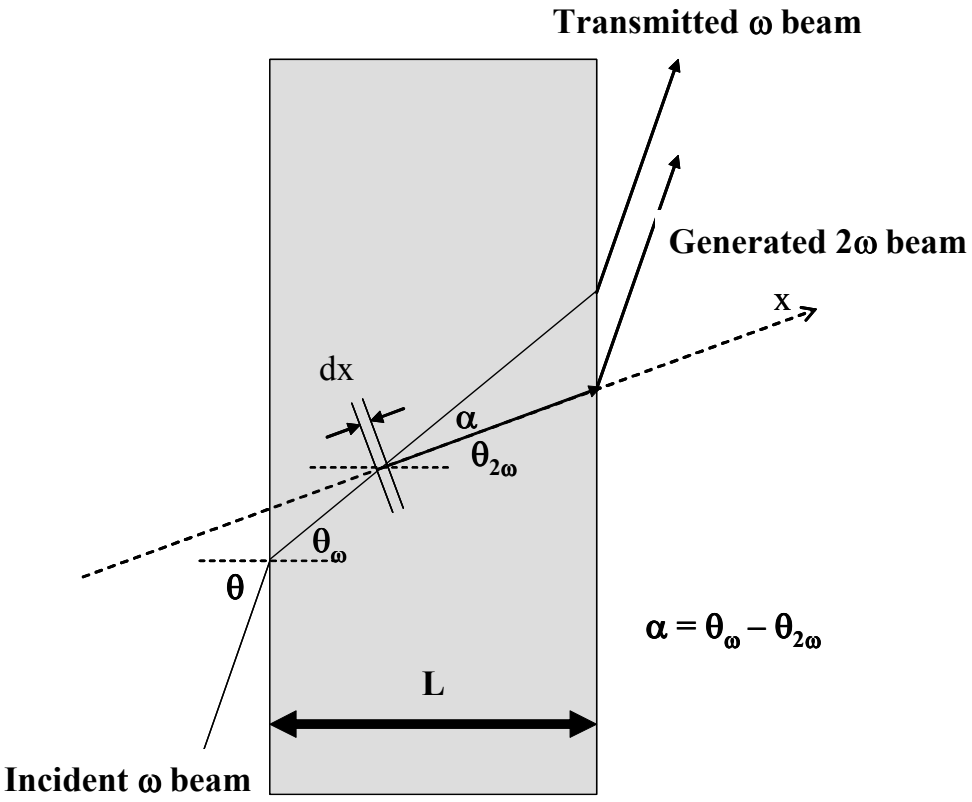

Figure 1.2 Geometric model for Maker-fringe theory.

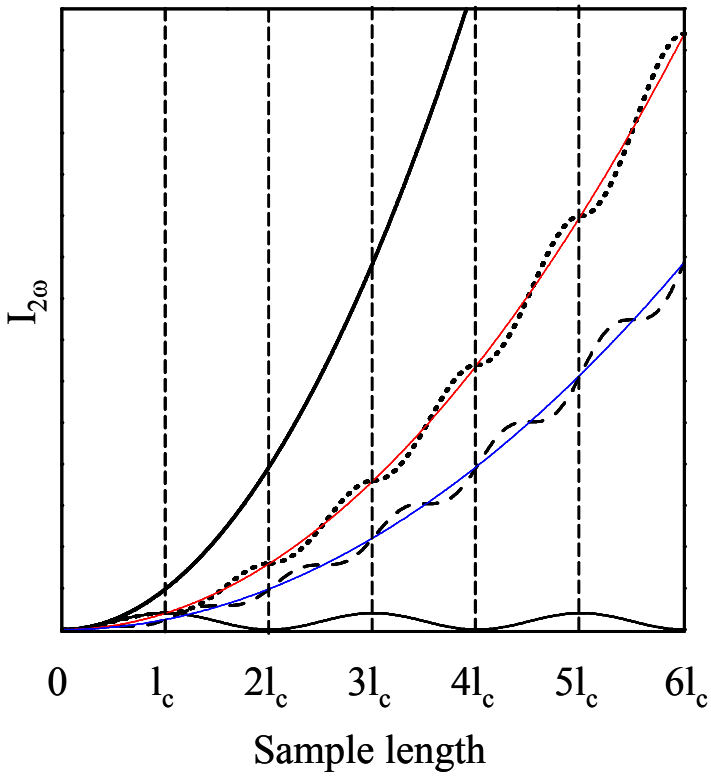

Figure 1.3 Second-harmonic intensity transition against $P^{(2)}$-interactive length. Thin solid line corresponds to a general nonlinear material in which $n_{\omega} \neq n_{2\omega}$, thick solid line phase-matched material, dotted line pseudo-phase matched material in a stepwise way, and dashed line optically poled material. These curves are calculated on the assumption that all samples has a same d_{eff}.

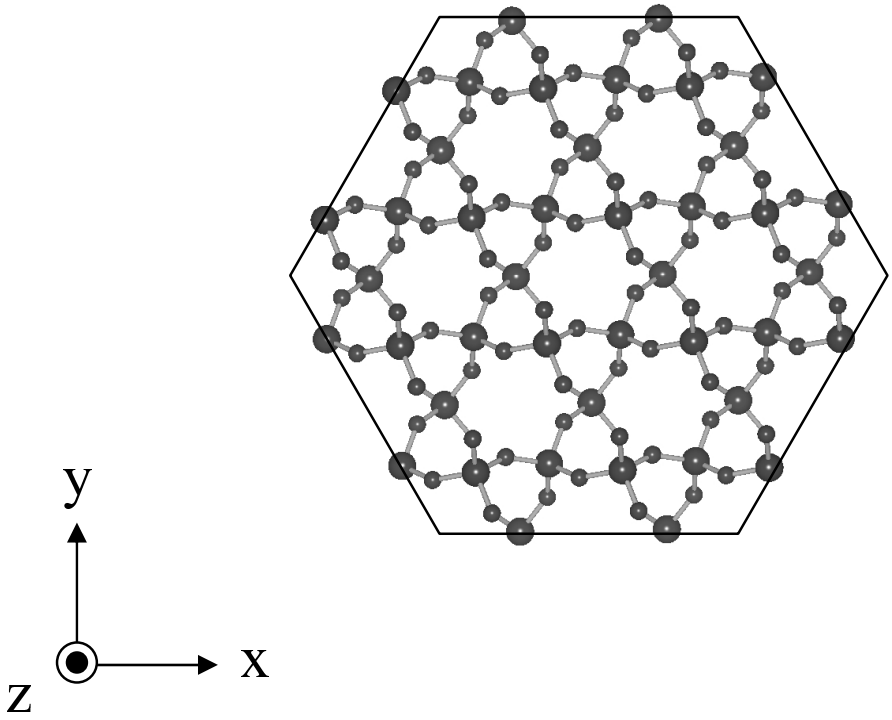
y
x
z

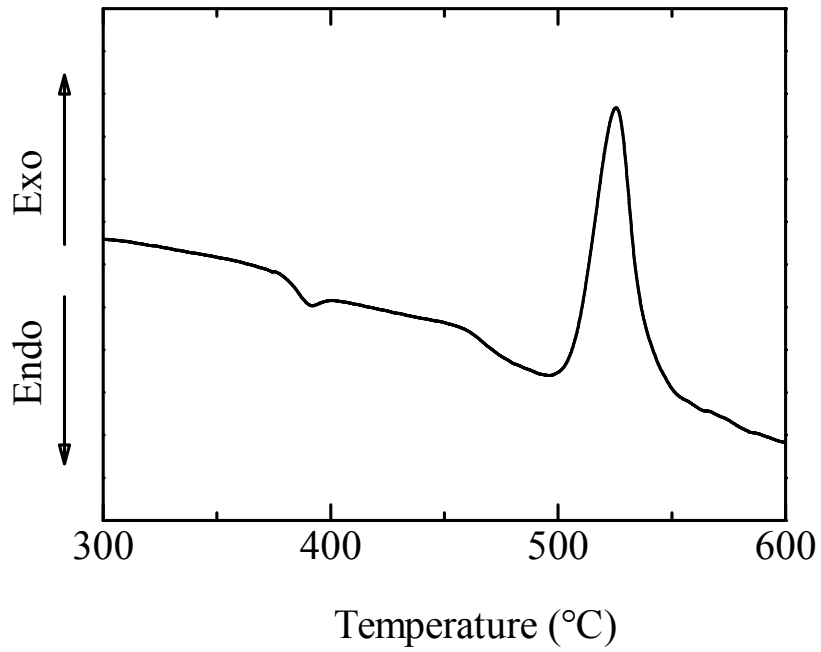

Figure 1.5 DTA curve for $15Nb_2O_5 \cdot 85TeO_2$ glass.

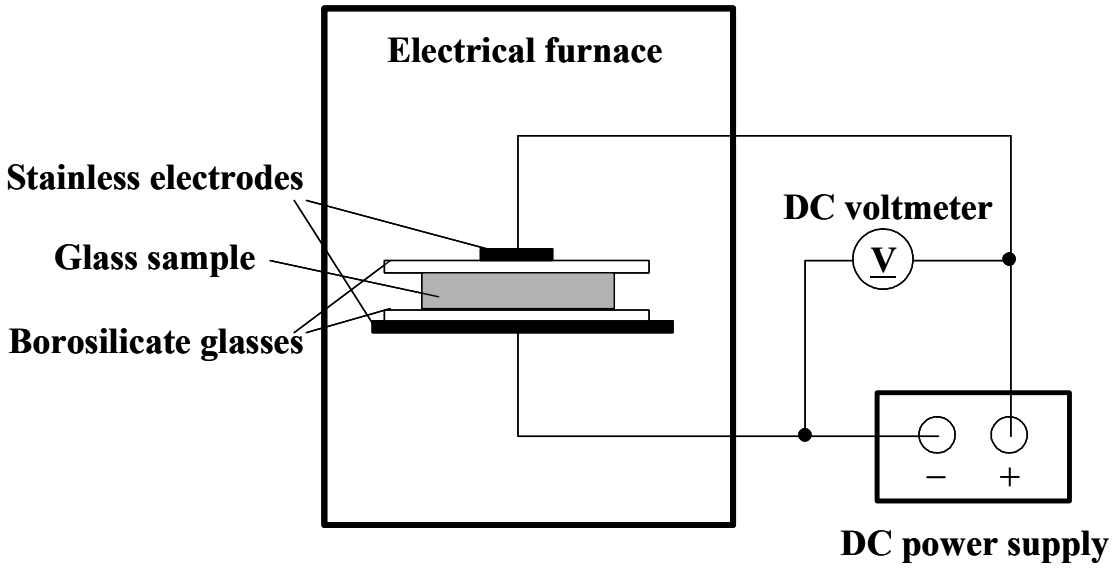

Figure 1.6 Schematic illustration of the setup for thermal/electrical poling.

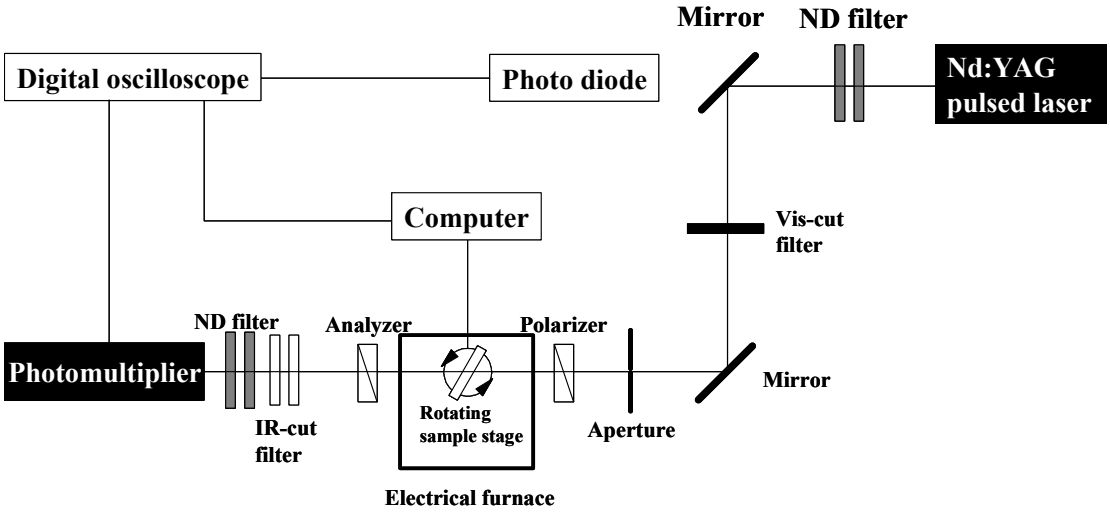

Figure 1.7 Schematic illustration of the setup for measuring second-harmonic intensity. Maker-fringe configuration was adopted for SHG measurements.

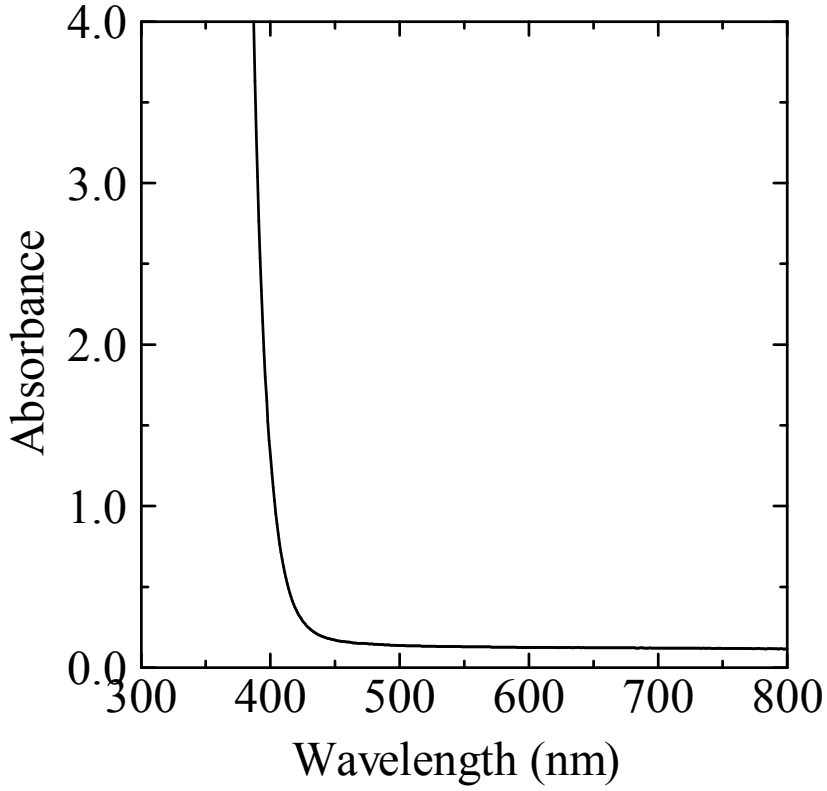

Figure 1.8 Optical absorption spectrum for the $15Nb_2O_5 \cdot 85TeO_2$ glass sample poled at 290 ˚C.

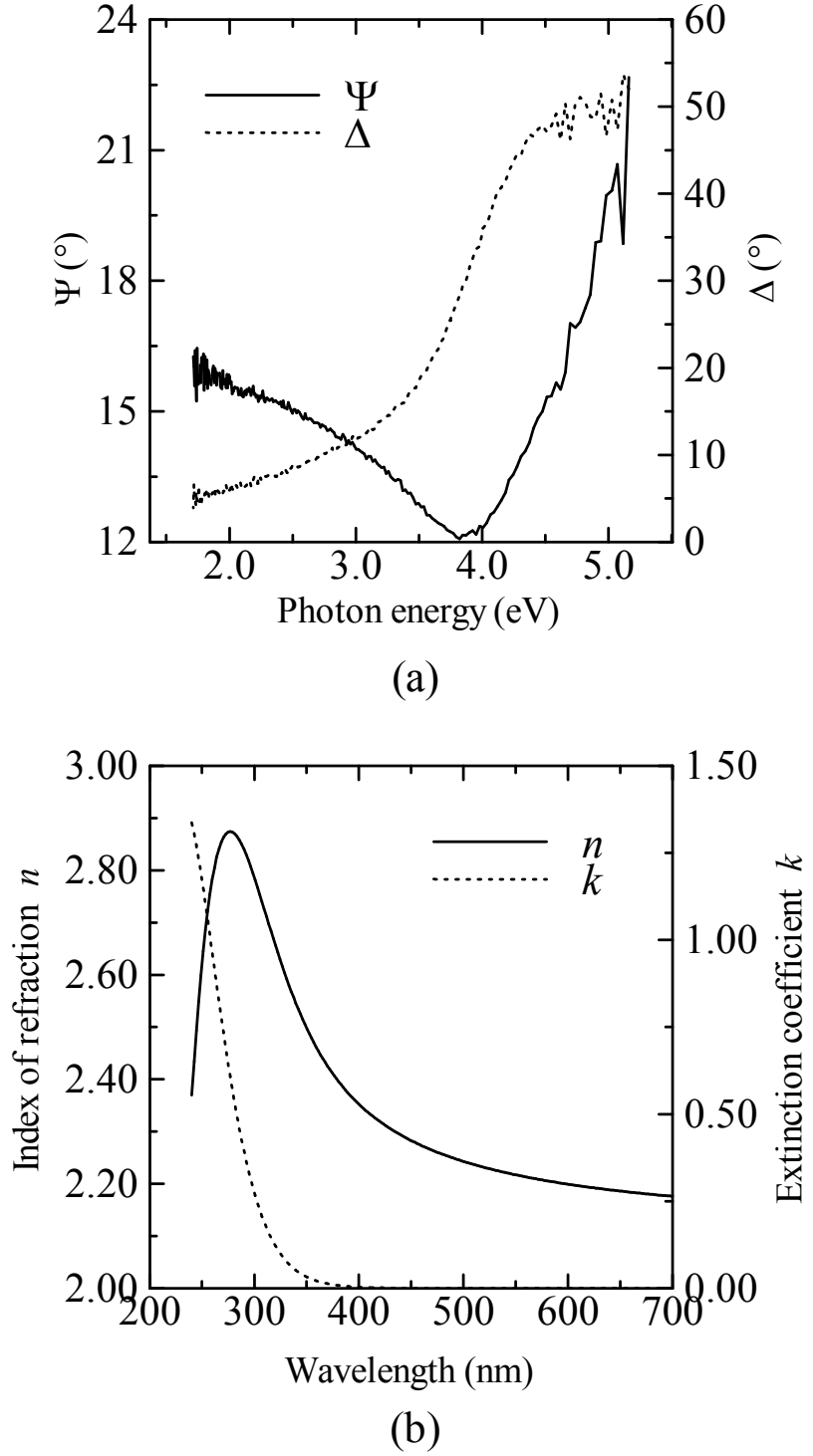

Figure 1.9 The results of Ellipsometry for $15Nb_2O_5 \cdot 85TeO_2$ glass. The above diagram (a) shows the Stokes parameters Ψ and Δ. The below (b) is a simulated wavelength dependence of complex refractive indices $n + ik$.

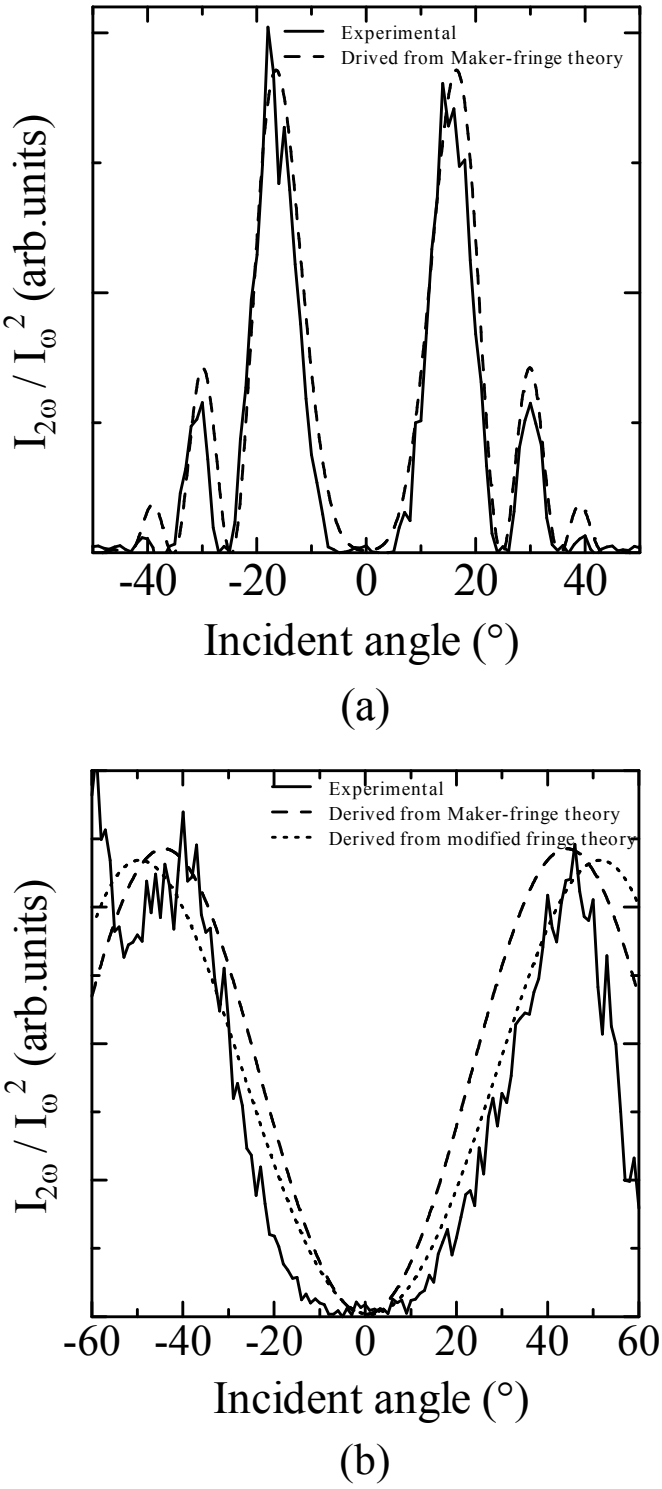

Figure 1.10 Maker-fringe patterns for (a) Y-cut α-quartz plate 1.046 mm thick and (b) the $15Nb_2O_5 \cdot 85TeO_2$ glass sample poled at 290 ˚C, 3 kV for 20 min.

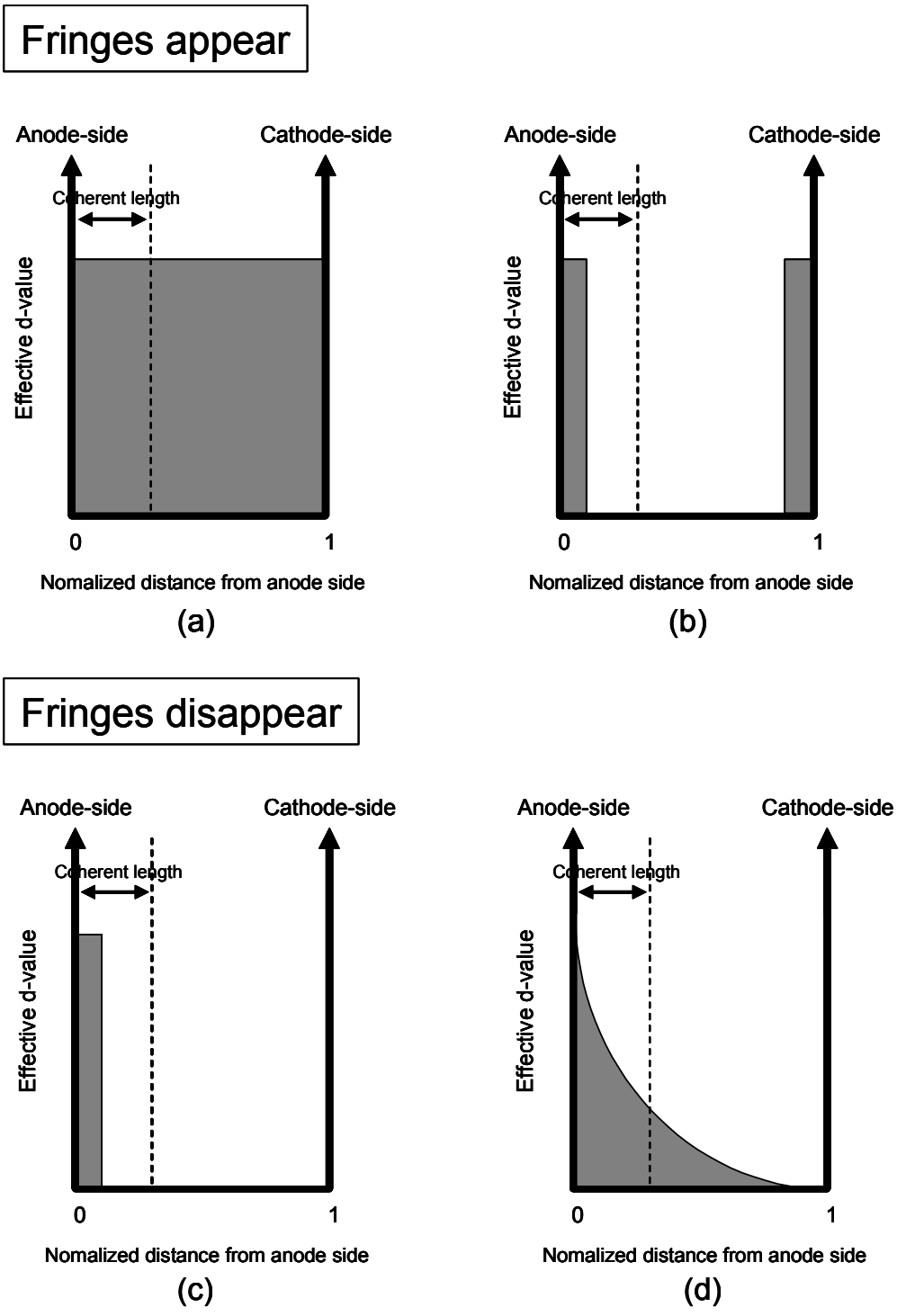

Figure 1.11 The d-value distribution determining the appearance of fringes in Maker-fringe pattern. Cases (a) and (b) lead to the oscillation in SH intensity, and cases (c) and (d) to the absence of fringe.

1.2 Second-harmonic generation in thermally/electrically poled tellurite glasses

Introduction

These days there have been increased interests in photo- and electrically-induced structural change and the resultant characteristic properties. In particular, considerable attention has been paid to poling-induced second-harmonic generation (SHG) in glassy materials. Generally, glassy materials exhibit no even-order nonlinear optical phenomena, nor is SHG allowed in them because of their centrosymmetric structure. Nonetheless, since Österberg and Margulis observed SHG in GeO_2-SiO_2 glass fiber [1], many research groups have been engaged in the investigation on second-order nonlinearity in amorphous media. In 1988, M. V. Bergot et al. discovered SHG from argon-laser-irradiated GeO_2-SiO_2 fiber under electric-field-applied condition [2]. Several years later, Myers et al. have succeeded in inducing large artificial second-order nonlinearity ($\chi^{(2)} = 1.0$ pm/V) into a fused silica plate by applying an intense DC electric field under a high temperature [3]. Such operation is generally called "thermal/electrical poling" and regarded as a useful procedure for $\chi^{(2)}$-induction. Since then, there have been various kinds of poling techniques developed for various oxide glasses [4-7]. It is commonly believed that the SHG-induction mechanism eventuates in the breakdown of the structural inversion symmetry, however, the mechanism of which has not been clarified yet. Stolen et al. and some groups suggested that it was attributed to the alignment of the structural units with dipole moment (e.g. non-bridging oxygen) in glass network [8, 9]. Meanwhile, other groups represented by Anderson et al. pointed out that a locally induced frozen-in space-charge played an important role in $\chi^{(2)}$-induction although they did not specify the charged species. According to them, a large DC field $\mathbf{E}_{dc}$ constructed by poling acts on the inherent $\boldsymbol{\chi}^{(3)}$ of glass to give an effective $\boldsymbol{\chi}^{(2)}$ in accordance with

$$\boldsymbol{\chi}^{(2)}(-2\omega,\omega,\omega) = 3\boldsymbol{\chi}^{(3)}(-2\omega,0,\omega,\omega)\cdot\mathbf{E}_{dc} \tag{1.35}$$

(DC Kerr effect) [10-12]. Narazaki et al. focused on the effect of the space-charge layer, and showed the importance of mobile cations present in a precursor glass for the thermal/electrical $\chi^{(2)}$-encoding [13, 14].

In this section, an efficient poling technique is attempted for a $15Nb_2O_5 \cdot 85TeO_2$ glass plate to induce second-order nonlinearity. In the skillful technique, thermal poling is accompanied by sodium-ion doping. The concept is to construct a charged layer by introducing charged centers from the outside of the glass. The resultant glass shows a detectable SHG dependent on the poling temperature, while as-made sample does not. Observed SH intensity is analyzed from the viewpoint of decay kinetics using a stretched exponential function.

· Tellurite glass

The glass containing TeO_2 as the network former is called tellurite glass. Tellurite glass possesses many interesting physical properties such as low melting point, high chemical durability, good infrared-to-visible transmittance and high refractive index originated in a d-orbital contribution of the Te^{4+} cations situated in the network. These physical properties make the material attractive not only from fundamental viewpoint but also in terms of practical applications. Pure tellurium oxide itself (TeO_2) is known as a conditional glass former, requiring fast quenching to form glass. The network is built up by corner-sharing $[TeO_4]^{4-}$ trigonal bipyramids (tbp, Fig.1.12(a)) with an equatorial position occupied by lone pair electrons, as in crystalline α-TeO_2 (Fig 1.13). The addition of modifier cations induces variation in the structural unit from the $[TeO_4]^{4-}$ trigonal bipyramed to the $[TeO_3]^{2-}$ trigonal pyramid entities (tp, Fig. 1.12(c)) through an intermediate asymmetric structure $[TeO_{3+1}]^{4-}$ (Fig. 1.12(b)), which makes it easier to form glassy state. Such deformation causes a modest increase of nonbridging oxygen (NBO) responsible for a significant change in the physical properties [15]. Since permanent dipole moment is observed in all the structural units, tellurite glass is considered to have an advantage in inducing polarized structure using external stimulation.

Nb_2O_5-TeO_2 glass treated in this study is comprised of $[NbO_6]^{7-}$ unit as a modifier

and $[NbO_4]^{3-}$ unit as a network former in addition to the three units mentioned above. Spectroscopic analysis has shown that the addition of Nb_2O_5 introduces changes in Te-derived structural unit. The Nb_2O_5-TeO_2 glass exhibits a higher refractive index than pure TeO_2 glass. This is because the refractive index is governed by the hyperpolarizability of Nb-O bonds and d-orbital contribution derived from the Nb^{5+} cations in the glass network. The large refractive index makes the Nb_2O_5-TeO_2 glass a potential candidate for optical devices with high performance.

Experimental

· Sample preparation

$15Nb_2O_5 \cdot 85TeO_2$ glass in molar ratio was prepared from reagent-grade Nb_2O_5 and TeO_2 powder (purity was 99.9 %). The raw materials were mixed thoroughly, and melted in a platinum crucible at 850 ˚C for 15 min in air. The melt was poured into a mold made of graphite and cooled to room temperature in air. The glass thus obtained was annealed for 15 min at 400 ˚C, 20 ˚C higher than its glass transition temperature determined by differential scanning calorimetry (Rigaku, DSC-8230B), and was cut into a rectangular parallelepiped by means of a saw pasted with diamond powder. The cut samples were subjected to optical measurements after the surfaces were polished. The thickness of the glass sample was 1.00 mm.

· Thermal/electrical poling treatment (Sodium ion doping)

The schematic illustration of the thermal/electrical poling apparatus is shown in Fig. 1.6. After a glass sample was cleaned with ethanol, it was sandwiched in between two commercially available sodium borosilicate cover glasses 0.15 mm thick and contacted with electrodes made of stainless steel. The cover glasses were used as the sodium-ion source. The glass sample was heated to an aimed temperature (235–300 ˚C) in an electric furnace. After the voltage of 3 kV was applied for 15 min with the raised temperature kept constant, the sample was cooled to room temperature with the voltage maintained. It should be noted

that the actual voltage applied to the glass sample was less than 3 kV because of the cover glasses.

· X-ray photoelectron spectroscopy (XPS)

Incorporation of sodium ions into the poled sample was confirmed by X-ray photoelectron spectroscopy (XPS). XPS measurements were carried out with ULVAC-phi MT-5500 using MgKα X-ray as the excitation source in the pressure range of 10^{-8} to 10^{-9} Pa.

· SHG measurement

SHG measurement was executed using a Maker-fringe configuration. As the incident light, *p*-polarized fundamental wave of a pulsed neodymium-doped yttrium-aluminum-garnet (Nd:YAG) laser (Spectra Physics, GCR-11) which operated in a Q-switched mode with 10 Hz repetition rate was used. A setup for the measurement is shown in Fig. 1.7. A poled sample was placed in an electric furnace placed on the light axis. The *p*-polarized fundamental wave at 1064 nm with 9 ns duration was incident into the sample. The rotation axis of the sample was parallel to the sample surface (namely, perpendicular to the polarized direction). For each incident angle, the *p*-polarized SH light (at 532 nm) transmitted through the sample was detected with a photomultiplier connected to a monochromator (Hamamatsu Photonics, R955) after passing through IR cut filters. Y-cut α-quartz 1.046mm thick (rotating around z-axis) was used as a standard. The decaying behavior in d-value was monitored by measuring the time variation of SH intensity with incident angle fixed at the angle showing the maximum SH intensity.

· Evaluation of second-order nonlinearity

The second-order nonlinearity of the poled sample was estimated by fitting the modified Maker-fringe equation (Eq. 1.33) to an experimental fringe pattern. Optical absorption at the relevant wavelengths (α at 1064 and 532 nm) was ignored based on the optical absorption spectrum.

· AC impedance spectroscopy

To check the electric conduction properties, AC impedance spectroscopy was carried out for $15Nb_2O_5 \cdot 85TeO_2 \cdot 0.5Na_2O$ glass with circular disk shape. The thickness and the circular area were 2.350 mm and 0.7472 cm^2, respectively. After coating graphite electrode on the circular surfaces, the absolute values of impedance $|Z|$ and the phase angle difference θ were measured in the frequency range of 10.0 Hz – 1.000 MHz using a computer interfaced HIOKI chemical impedance meter 3532-80. The conduction properties were characterized in terms of two complex formalisms; impedance Z^* and electric modulus M^*.

Results

· Sodium doping by thermal/electrical poling

Table 1.2 and Fig. 1.14 shows the ratio of Nb/Te and of Na/Te at the anode-side surface which is determined by dividing the sensitivity-corrected peak area for niobium or sodium by that for tellurium. The detected sodium exceeds that of the as-annealed sample. However, such significant change is not seen at the cathode-side surface. As poling

Table 1.2 The amount of Nb/Te and Na/Te atomic ratio at the anode-side surface of thermally/electrically poled $15Nb_2O_5 \cdot 85TeO_2$. They are calculated from the peak area in X-ray photoelectron spectra. These values are normalized with the amount of tellurium for the purpose of comparing the amount among different samples.

	Atomic concentration ratio	
	Nb/Te	Na/Te
As-annealed	0.495	0.048
Poled at 180 ˚C	0.452	0.074
Poled at 220 ˚C	0.450	0.128
Poled at 260 ˚C	0.361	1.091
Poled at 300 ˚C	0.381	0.474
10 μm in depth	0.712	0.191

temperature increases, Na/Te initially increases, takes the peak value at 260 ˚C and decreases, while Nb/Te does not show such a drastic change. The result reveals that sodium is successfully doped into the tellurite glass sample by the thermal/electrical poling.

· Maker-fringe pattern of thermally/electrically poled $15Nb_2O_5 \cdot 85TeO_2$ glass

Figure 1.15 shows the Maker-fringe pattern for the $15Nb_2O_5 \cdot 85TeO_2$ glass sample poled at 260 ˚C. SH intensity dependent on incident angle is observed while the as-prepared glass did not show SHG. General form of the Maker-fringe pattern was not so different among thermally/electrically poled samples except for the magnitude. Figure 1.16 displays the poling temperature dependence of maximum SH intensity. As poling temperature increased, SH intensity increases, takes a peak top, and then decreases. The largest SH intensity is achieved when poling temperature is 260 ˚C. The incident angle corresponding to the maximum SH intensity slightly varied with poling temperature. The shift in the angle means that the thickness of $\chi^{(2)}$-active layer changed. More distinct relationship is described in the next section.

· d-value profile

Figure 1.17 shows the d-value profile ($d_{33}(0)$ and γ^{-1}) for each poling temperature. They were estimated from the Maker-fringe pattern. $d_{33}(0)$ decreases with poling temperature increasing after showing peak value at about 250-260 ˚C. On the other hand, characteristic length γ^{-1} monotonically increases with an increase in poling temperature, and above 270 ˚C, it is apt to be saturated.

· Time decay in SH intensity

Figure 1.18 shows the time variation in SH intensity for the sample poled at 260 ˚C. $I(t)$ is the SH intensity t h after removing the poling voltage. The values shown in the figure indicate the measurement temperature. The decay rate becomes more rapid as the temperature increases, although it is barely observed under the measurement temperature of 50 ˚C within 5 h. Relaxation constants were determined by fitting the stretched exponential

function given by

$$I(t) = I(0)\exp\left[-\left(\frac{t}{\tau}\right)^{\beta}\right] \tag{1.36}$$

to the experimental data, where τ is the most possible relaxation time and β is the parameter representing the distribution of relaxation time. The stretched exponential function is useful to analyze a relaxation phenomenon governed by more than two kinds of relaxation components or a single component with finite distribution. The values of τ and β for each measurement temperature are summarized in Table 1.3. The value of β varies from unity to 0.7. Figure 1.19 shows the measurement-temperature dependence of τ. The natural logarithms of reciprocal relaxation time are plotted against reciprocal temperature. The solid line is drawn by fitting the Arrhenius relation given by

$$\frac{1}{\tau} = \left(\frac{1}{\tau_0}\right)\exp\left(-\frac{E}{RT}\right), \tag{1.37}$$

where T is measurement temperature, R the gas constant, E the activation energy for relaxation, and τ_0 a proportional constant. From the slope of the line, $E = 77$ kJ mol^{-1} is obtained.

Table 1.3 Average relaxation time τ and parameter β in the stretched exponential function (Eq. 2.5) for decay of second-order nonlinearity induced in Na^+-doped $15Nb_2O_5 \cdot 85TeO_2$ bulk glass by thermal poling. The poling was carried out at 260℃.

Temperature (˚C)	τ (h)	β
50	-[a)]	-[a)]
75	19	0.7
100	1.7	0.9
150	0.15	1.0

a) The relaxation time could not be obtained because the decay was very sluggish at least 5 h after ceasing of thermal poling.

· AC impedance spectroscopy

To interpret experimental data sets on AC impedance, it is essential to have an equivalent circuit model. The ionic conduction is, in general, characterized by a series combination of impedance which is represented by a parallel RC circuit as shown in Fig. 1.20. The characterization starts with counting the number of impedance. For a RC parallel circuit, the complex impedance Z^* and the complex electric modulus M^* are given by

$$Z^* = \frac{R}{1 + i\omega\tau} \tag{1.38}$$

$$M^* = i\omega C_0 Z^*, \tag{1.39}$$

where C_0 and τ are the capacitance in vacuum and relaxation time, respectively. The τ is interrelated with R and C as follows;

$$\tau = RC \tag{1.40}$$

Both for Z^* and M^*, each parallel RC element gives a Debye peak in the spectroscopic plots of the imaginary component or a semicircle in the complex plane. The impedance and the electric modulus spectra for the $15Nb_2O_5 \cdot 85TeO_2 \cdot 0.5Na_2O$ glass shown in Fig. 1.21 exhibit only one peak in the imaginary component. Since their peak frequencies are almost identical, the conductivity can be characterized by one relaxation time, namely, by one RC parallel circuit (impedance). In Fig. 1.22, Cole-Cole plots for Z^* are shown for each temperature. A semicircle is formed by sweeping the AC frequency along with Eq. 1.38. The intercept made by the semicircle on the real axis gives the bulk DC resistance R. As temperature increases, DC resistance decreases in response to the shortening in radius of the semicircle. The DC conductivity σ_{DC} derived from R is listed in Table 1.4. The DC conductivity obeys the Arrhenius relation (Eq. 1.41) against reciprocal temperature as in Fig. 1.23.

$$\sigma_{DC} = \sigma_0 \exp\left(-\frac{E_\sigma}{RT}\right) \tag{1.41}$$

The activation energy obtained from the least squares straight line fit is 106.6 kJ/mol.

Table 1.4 DC conductivity of $15Nb_2O_5 \cdot 85TeO_2 \cdot 0.5Na_2O$ glass.

Temperature T (°C)	DC conductivity σ_{DC} ($\Omega^{-1}cm^{-1}$)
290	7.267×10^{-8}
300	4.558×10^{-8}
310	2.983×10^{-8}
320	2.074×10^{-8}
330	1.499×10^{-8}
340	1.092×10^{-8}
350	7.591×10^{-9}
360	5.726×10^{-9}
370	4.166×10^{-9}
380	2.886×10^{-9}
390	1.923×10^{-9}
400	1.327×10^{-9}

Discussion

· $\chi^{(2)}$-induction by thermal/electrical poling

Since SHG diminished after polishing out the positively-biased surface by a few tens of microns, the SHG-active region was situated on the anode-side surface as is reported earlier [3]. The absence of fringes in the Maker-fringe patterns depicts that the thickness of the SHG-active region is less than or comparable with the coherence length. Even if the nonlinearity was added at other places, the magnitude of which would be negligible [16,17].

As shown in Fig. 1.18, SHG attenuates in a few minutes when poled sample is placed in a high temperature condition, which means that the poling-induced state is metastable. The activation energy for the induced polarized state to decay is calculated to be 77 kJ mol^{-1}.

This value is approximately equal to that for DC conduction in sodium-containing $15Nb_2O_5 \cdot 85TeO_2$ glass (Fig. 1.23). These values are also equal to that for monovalent-cationic conduction in $xM_2O \cdot (100\text{-}x)TeO_2$ glass ($M=Na^+$ or Li^+, x=10-30); about 100 kJ mol^{-1} [18,19]. The decay kinetics on SH intensity and XPS indicate the close relationship between doped charged centers (sodium ions) and the second-order nonlinearity induced by thermal/electrical poling. The exponential factor β approaches to unity with increasing measurement temperature, as shown in Table 1.3. The parameter β less than unity probably comes from the nonuniformity of the site for diffusing species and/or interaction among those species; strong affinity or repulsive force among the species results in the discrepancy from unity as well.

Based on the discussion, the $\chi^{(2)}$-induction mechanism of thermal/electrical poling is speculated as follows: At a poling temperature higher than 200 ˚C, a part of sodium ions in the positively-biased cover glass drifts into the sample deeply due to the increase in flexibility of the glass structure and the increase in mobility of sodium ions. After removing the poling field, the implanted sodium ions construct a DC electric field $\mathbf{E}_{dc}$, which acts on the inherent $\chi^{(3)}$ of the glass medium to give an effective $\chi^{(2)}$. When poling temperature does not exceed a threshold, the stiffness of the glass structure prevents the migration of sodium ions and reduces γ^{-1}. Considering that a sodium ion holds a positive charge, it can be explained why the nonlinearity is induced only beneath the anode-side. Precipitate was sometimes observed beneath the cathode-side surface after thermal/electrical poling, it is because electrochemical reduction of tellurium ions occurred for charge compensation. A similar phenomenon was reported in Bi_2O_3-ZnO-B_2O_3 glass [20]. In the report, it was confirmed that the bismuth precipitates did not influence on the output SH intensity.

In order to confirm the correctness of the suggested mechanism, the quantitative discussion is attempted later.

· Critical factor determining output SH intensity

The characteristic length γ^{-1} tends to be elongated with increasing poling temperature (Fig. 1.17). At a high poling temperature, a part of implanted sodium ions drifts

to the cathode deeply due to the increase in the flexibility of stiff glass structure, and as a result of which, SHG-active region expands. By contrast, at a lower poling temperature, the stiffness of the glass structure prevents the immigration of sodium ion, therefore, the characteristic length is constricted. In Fig. 1.24, an output SH intensity is calculated as a function of sample length L (a) and γ^{-1} (b) under the conditions in the experiment. Δk is derived from the relevant wavelengths and the refractive indices of $15Nb_2O_5 \cdot 85TeO_2$ glass. These figures show that SH intensity is almost independent of L and γ^{-1} when

$$\frac{1}{\Delta k} << \gamma^{-1} << L' \tag{1.42}$$

is satisfied. When γ^{-1} exceeds 15 μm, SH intensity becomes nearly constant. The poled samples in the present study also satisfy Eq. 1.42. Therefore, for the samples poled at above 250 ˚C, the critical factor determining the output SH intensity is considered to be d-value or $d_{33}(0)$ because the γ^{-1}s experimentally estimated exceed 15 μm. Then, SH intensity is proportional to $d_{33}(0)^2$. This relationship is valid in this experiment (Compare Figs. 1.16 and 1.17).

· Relationship between $d_{33}(0)$ and doped sodium ions

Assuming that the frozen-in $\mathbf{E}_{dc}$ is built of positive charge of the implanted sodium ions, it is possible to obtain the relationship between the induced $d_{33}(0)$ and the amount of doped sodium ion using Gauss's law;

$$\nabla \cdot \mathbf{E}_{dc} = \frac{\rho}{\varepsilon} \tag{1.43}$$

where ρ and ε mean charge density and dielectric constant of the glass medium, respectively. By applying Gauss' law to Eqs. 1.32 and 1.35, the following relation is derived.

$$d_{33}(0) = \frac{3\chi^{(3)}(\theta_\omega)}{2\varepsilon\left[\exp(-\gamma L)-1\right]} q\,, \tag{1.44}$$

where q is the total charge in unit area and given by

$$q = \int_0^L \rho dz . \tag{1.45}$$

From this equation, it is found that $d_{33}(0)$ is proportional to the amount of implanted charge q. In the present case, $d_{33}(0)$ should be also proportional to Na/Te ratio at the anode-side surface since the characteristic length γ^{-1}s are not so different among the samples poled above 260 ˚C (Fig. 1.17). The Na/Te ratio for the poling temperature of 260 ˚C is 2.30 times larger than that for 300 ˚C. This value is coincident with 3.04, the ratio in $d_{33}(0)$. This fact supports Eq. 1.44. In other words, thermal/electrical poling accompanied by sodium-ion implantation is effective for $\chi^{(2)}$-induction. The discrepancy between those values, i.e. 2.30 and 3.04, probably comes from the $\mathbf{E}_{dc}$ component other than z-direction or a more complicated d-value distribution than the assumed by Eq. 1.32.

When poling temperature is low, sodium ions cannot obtain a thermal energy enough for passing through the interface between the cover glass and the sample. It suppresses charge migration into the sample. As poling temperature increases, the amount of implanted sodium ion increases, and which induces a large $d_{33}(0)$. However, why sodium ions were not fully doped when poling temperature was 300 ˚C is still unclear now.

Conclusion

Sodium ions are successfully doped beneath the anode-side surface of $15Nb_2O_5 \cdot 85TeO_2$ glass plate by a thermal/electrical poling technique using sodium borosilicate cover glasses. The poled glass sample shows SHG, and the intensity depends on the poling temperature. The maximum SH intensity and the maximum $d_{33}(0)$ is simultaneously achieved when poling temperature is 260 ˚C. Then, the SHG-active layer is 3 times thicker than the coherence length when incident angle is 50 ˚.

The activation energy for the decay in SH intensity is 77 $kJmol^{-1}$, which corresponds to DC conduction of sodium ion in alkaline-containing tellurite glasses.

The SH intensity observed is quantitatively interpreted in terms of the amount of doped sodium ion. From the SH intensity simulation, it is considered that the output can be further enhanced by selecting more suitable poling condition. The results obtained here show that the implantation of charged center is potentially available for the design of optical nonlinear devices.

References in Section 1.2

[1] U. Österberg and W. Margulis, Opt. Lett., 11 (1986) p. 516.

[2] M. V. Bergot, M. C. Farries, M. E. Fermann, L. Li, L. J. Ponytz-Wright, P. St. J. Russell and A. Smithson, Opt. Lett., 13 (1988) p. 592

[3] R. A. Myers, N. Mukherjee, S. R. J. Brueck, Opt. Lett., 16 (1991) p. 1732.

[4] A. Okada, K. Ishii, K. Mito, K. Sasaki, J. Appl. Phys., 74 (1993) p. 531.

[5] P. G. Kazansky, A. Kamal, P. St. J. Russell, Opt. Lett., 18 (1993) p.693.

[6] T. Fujiwara, D. Wong, Y. Zhao, S. Fleming, S. Poole, M. Sceats, Electron. Lett., 31 (1995) p. 573

[7] L. J. Henry, B. V. McGrath, T. G. Alley, J. J. Kester, J. Opt. Soc. Am. B, 13 (1996) p. 827.

[8] R. H. Stolen and H. W. K. Tom, Opt. Lett., 12 (1987) p. 585.

[9] B. Lesche, J. Opt. Soc. Am. B, 7 (1990) p. 53.

[10] D. Z. Anderson, Proc. SPIE, 1148 (1989) p. 186.

[11] E. M. Dianov, P. G. Kazansky and D. Yu. Stepanov., Sov. J. Quantum Electron., 19 (1989) p. 186.

[12] P. G. Kazansky and P. St. J. Russel, Opt. Commun., 110 (1994), p. 611.

[13] A. Narazaki, K. Tanaka and K. Hirao, J. Am. Ceram. Soc., 81 (1998) p. 2735.

[14] A. Narazaki, K. Tanaka and K. Hirao, J. Appl. Phys., 83 (1998) p. 3986.

[15] B. Jeansannetas, S. Blanchandin, P. Thomas, P. Marchet, J. C. Champarnaud-Mesjard, T. Merle-Mejean and B. Frit, J. Solid State Chem., 146 (1999) p. 329.

[16] A. L. Calvez, E. Freysz, and A. Ducasse, Opt. Lett., 22 (1997) p. 1547.

[17] L. Skuja, J. Non-Cryst. Solids, 179 (1994) p. 51.

[18] A. Pan and A.Ghosh, Phys. Rev. B, 59 (1999) p. 899.

[19] A. Pan and A. Ghosh, Phys. Rev. B, 60 (1999) p. 3224.

[20] O. Deparis, F. P. Mezzapesa, C. Corbari, P. G. Kazansky, K. Sakaguchi, J. Non-Cryst. Solids, 351 (2005) p. 2166.

(a) **TeO_4 trigonal bipyramid**

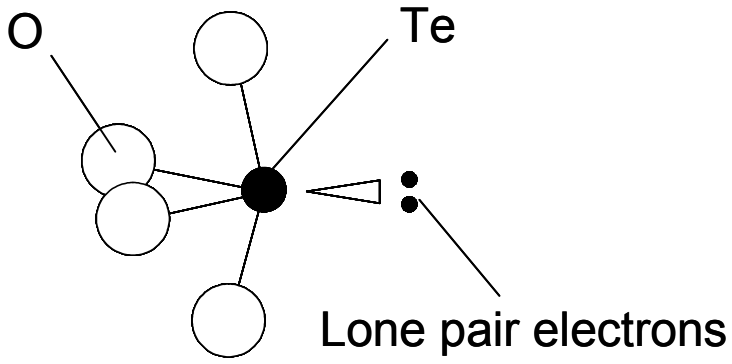

(b) **TeO_{3+1} trigonal pyramid**

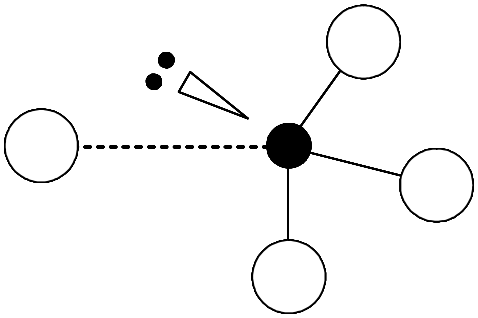

(c) **TeO_3 trigonal pyramid**

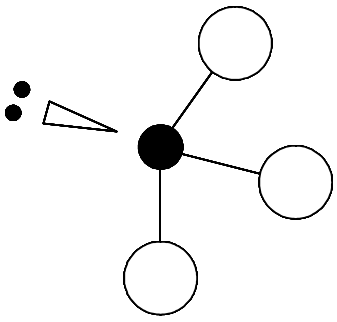

Figure 1.12 Illustration of the structural units for tellurite glass. Tellurium and oxygen atoms are given by closed and open circles, respectively: (a) $[TeO_4]^{4-}$ trigonal bipyramid (tbp), (b) $[TeO_{3+1}]^{4-}$ polyhedron, (c) $[TeO_3]^{2-}$ trigonal pyramid (tp).

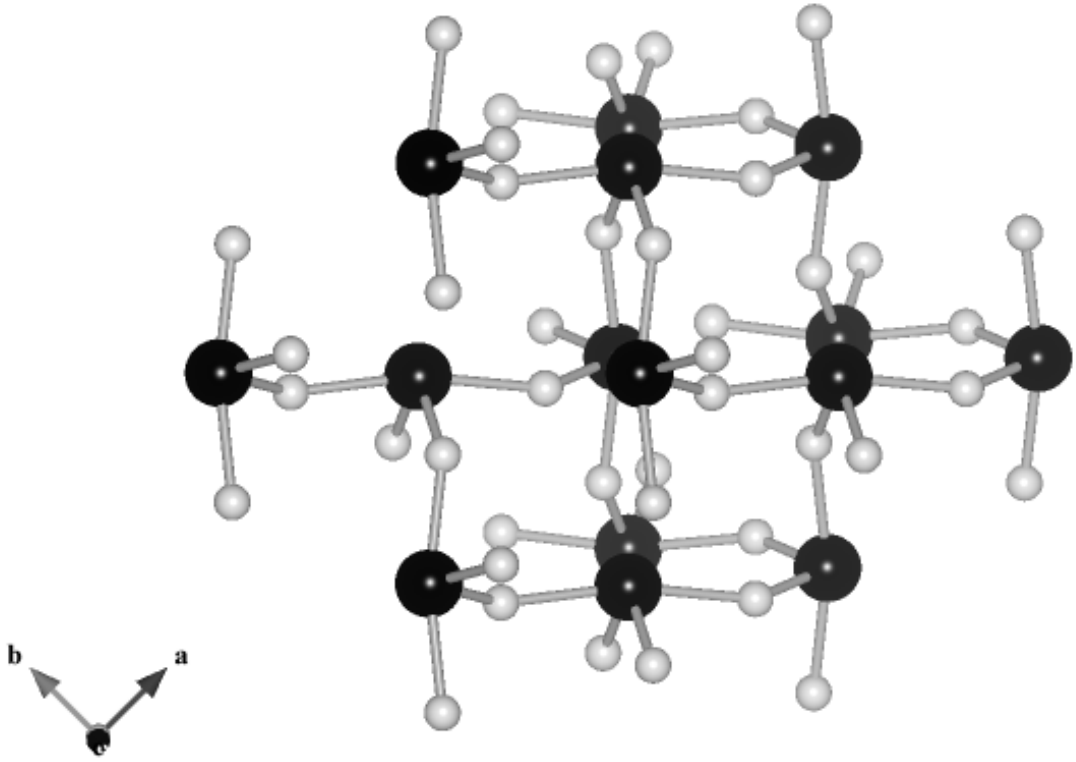

Figure 1.13 α-TeO_2 crystal structure. Black and white balls correspond to tellurium and oxygen atoms, respectively.

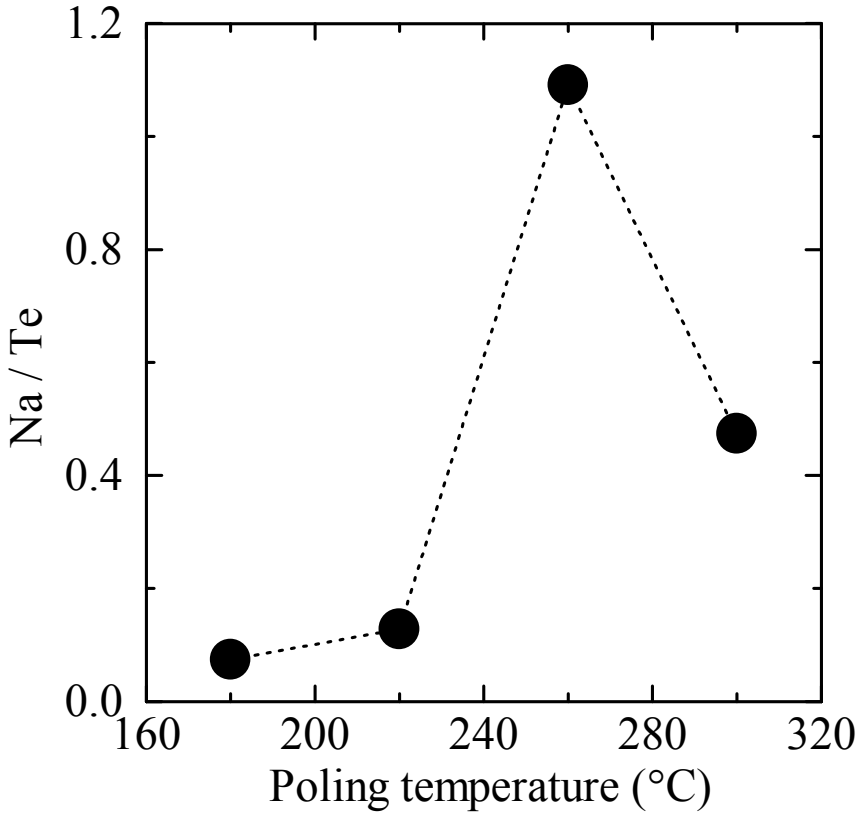

Figure 1.14 Na/Te ratio at the anode-side surface is plotted against poling temperature. They are obtained from XPS spectra.

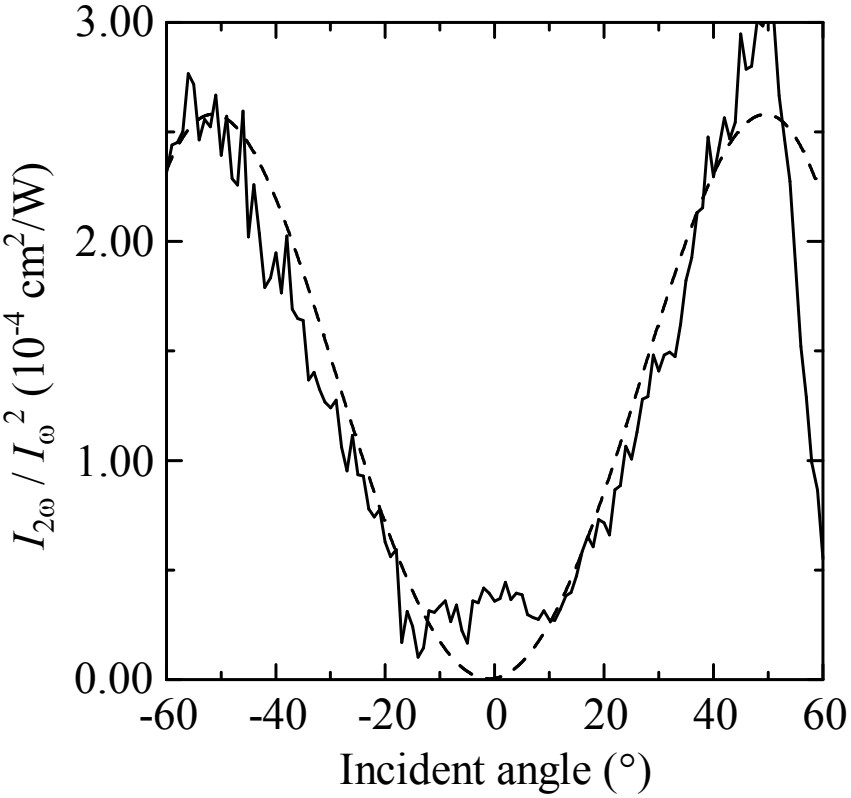

Figure 1.15 Maker-fringe pattern for $15Nb_2O_5 \cdot 85TeO_2$ glass poled at 260 °C. Solid and dashed lines represent the experimental data and the fitted theoretical value, respectively.

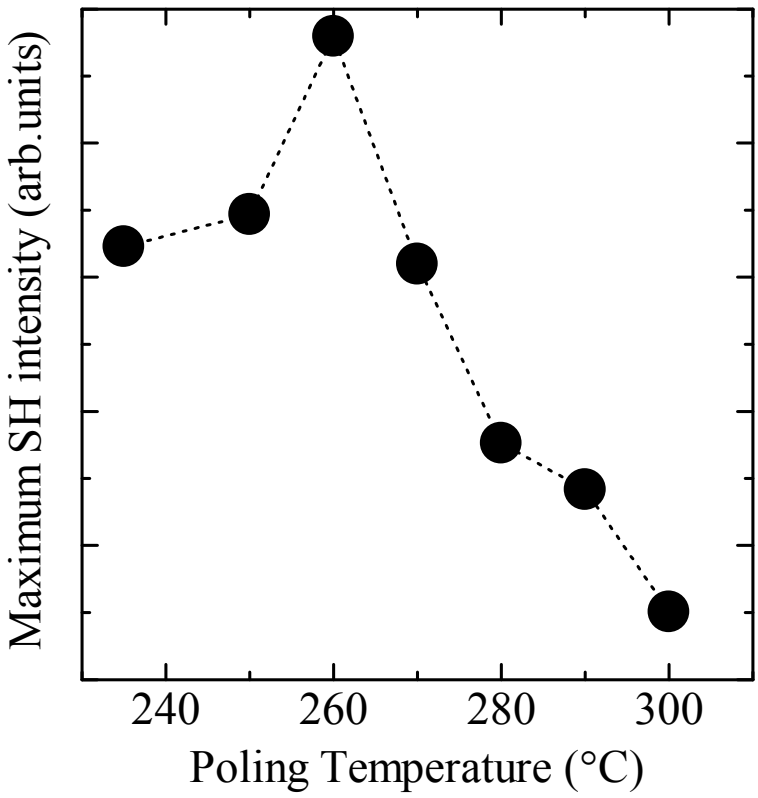

Figure 1.16 Poling temperature dependence of the maximum SH intensity generated in thermally/electrically poled $15Nb_2O_5 \cdot 85TeO_2$ glass.

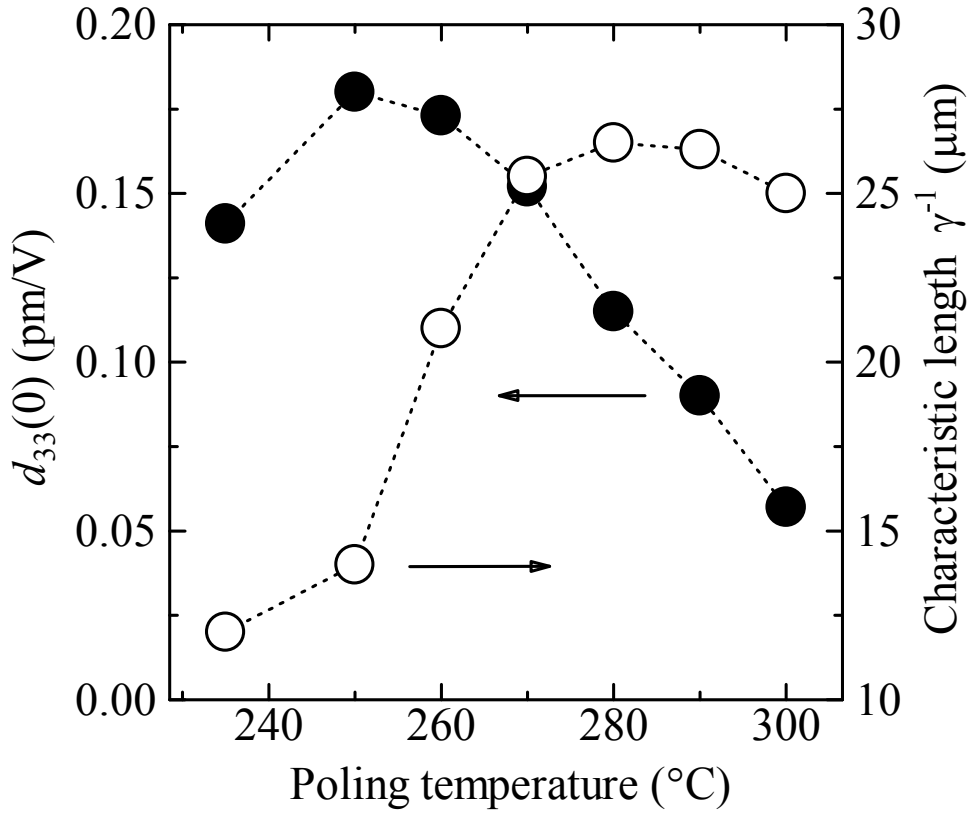

Figure 1.17 Induced d-value profile of the thermally/electrically poled $15Nb_2O_5 \cdot 85TeO_2$ glass samples under the assumption of $d_{33}(z) = d_{33}(0)\exp(-\gamma z)$, where z is the depth from the anode-side surface. $d_{33}(0)$ and γ^{-1} are denoted by closed and open circles, respectively.

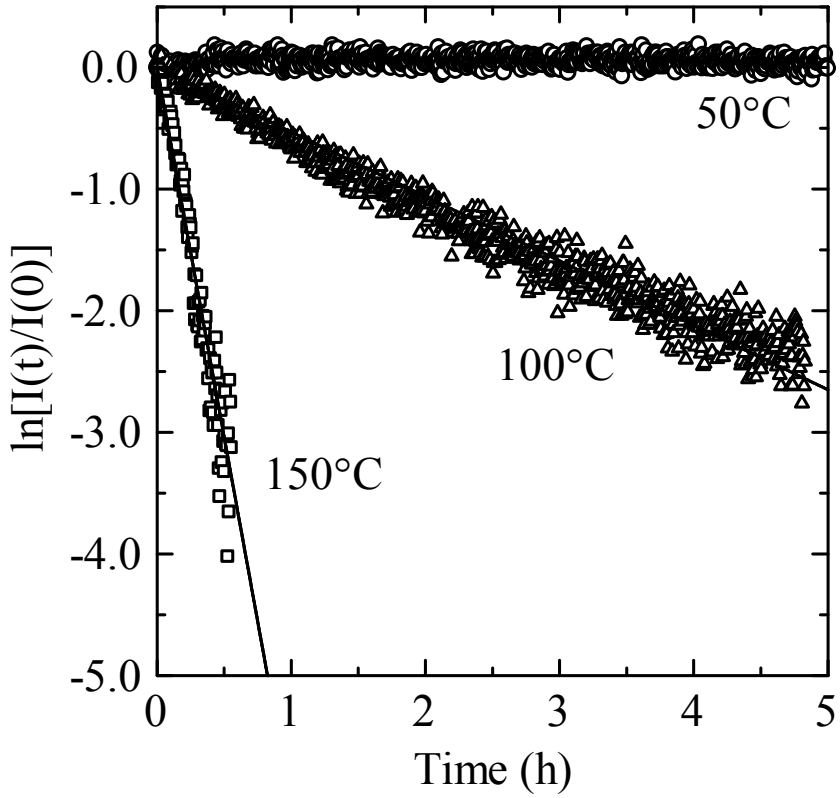

Figure 1.18 Decay in SH intensity for $15Nb_2O_5 \cdot 85TeO_2$ glass poled at 260°C. The measurement temperatures are denoted for each decay data. In the ordinate, $\ln[I(t)/I(0)]$, where I is the SH intensity and t is the time after the ceasing of thermal/electrical poling, is shown. The solid curves are the stretched exponential curves used for determining decay constants τ and β.

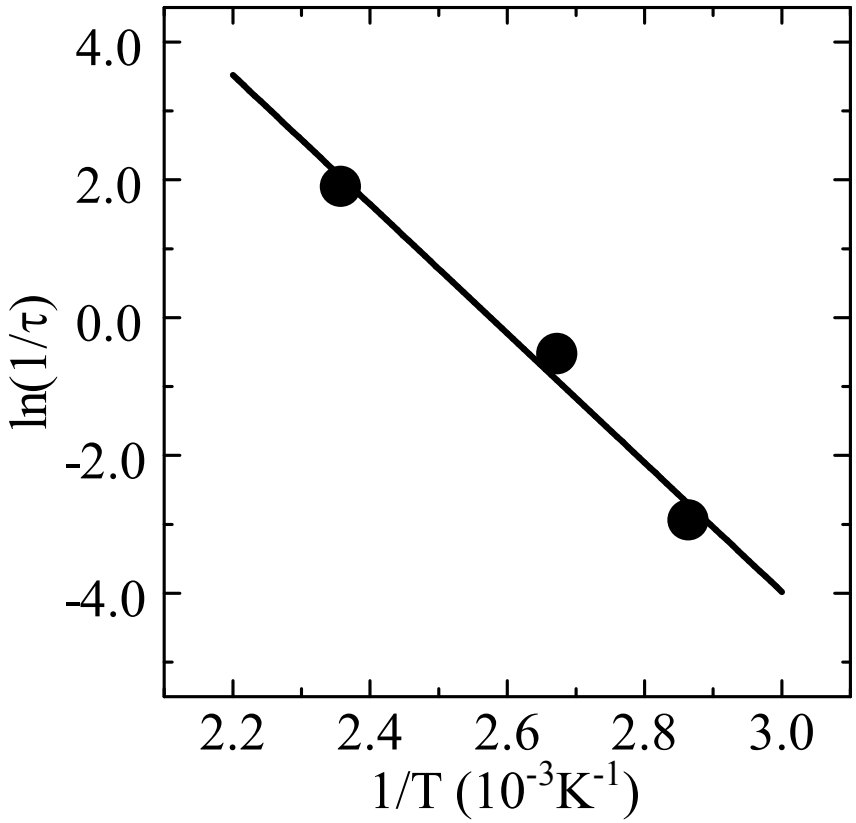

Figure 1.19 Temperature dependence of the relaxation time for observed SH intensity in $15Nb_2O_5 \cdot 85TeO_2$ glass poled at 260°C. The straight line is the Arrhenius straight line drawn by the least-squares method.

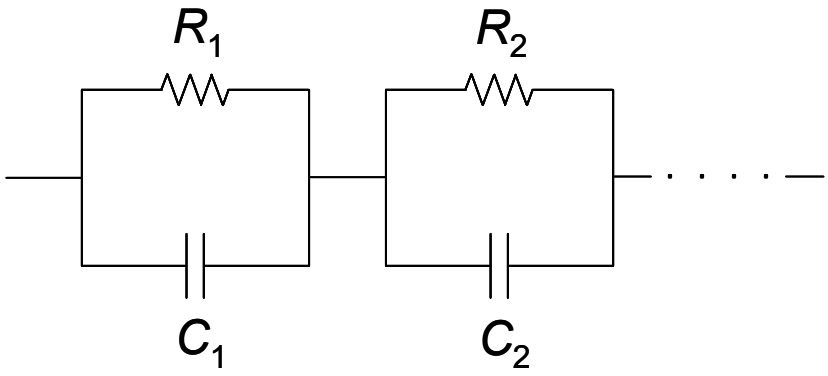

Figure 1.20 Equivalent circuit model typically used for estimating the electrical properties of insulating material.

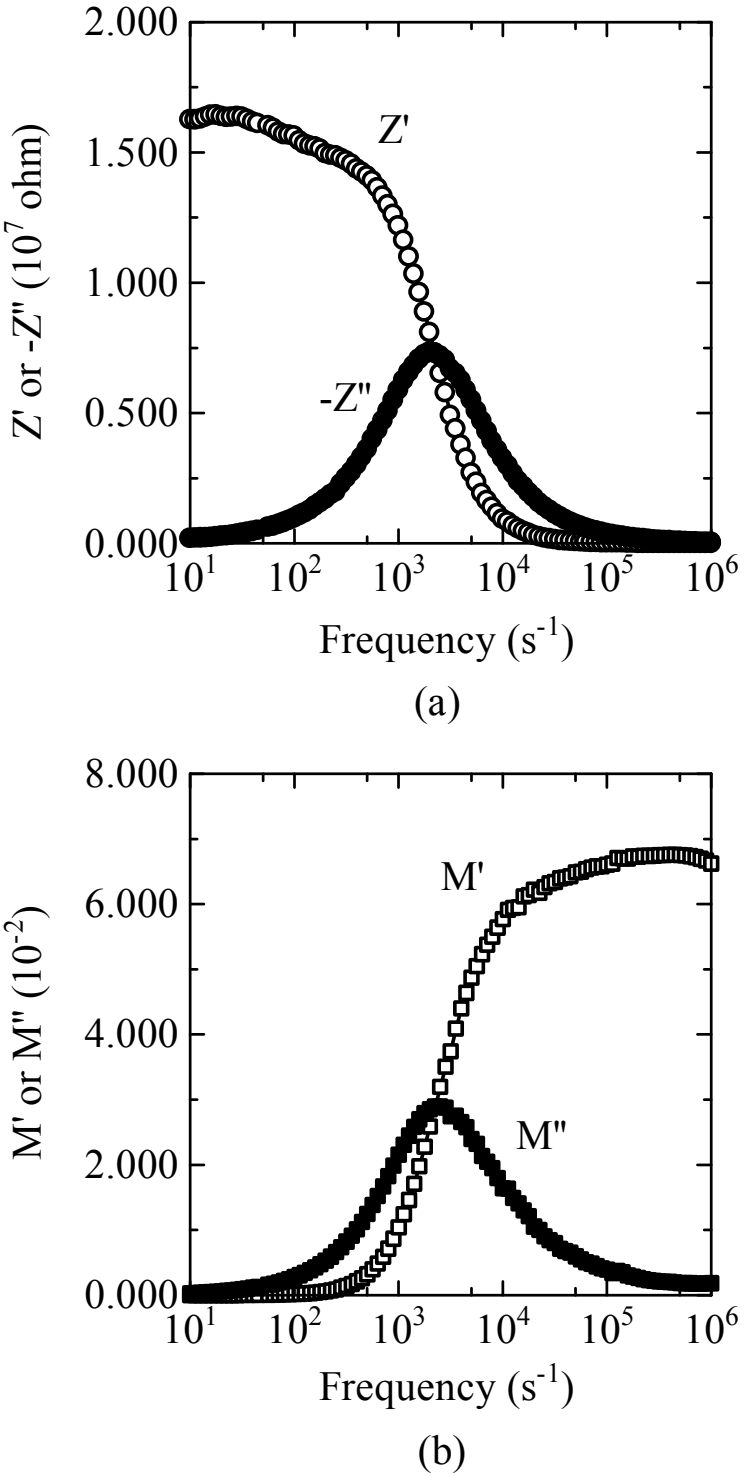

Figure 1.21 Impedance Z^* ($= Z' - iZ''$) and modulus M^* ($= M' + iM''$) spectroscopic plots for $15Nb_2O_5 \cdot 85TeO_2 \cdot 0.5Na_2O$ glass with 2.350 mm thick and the electrode area of 0.7472 cm^2. The data was collected at 370 ˚C.

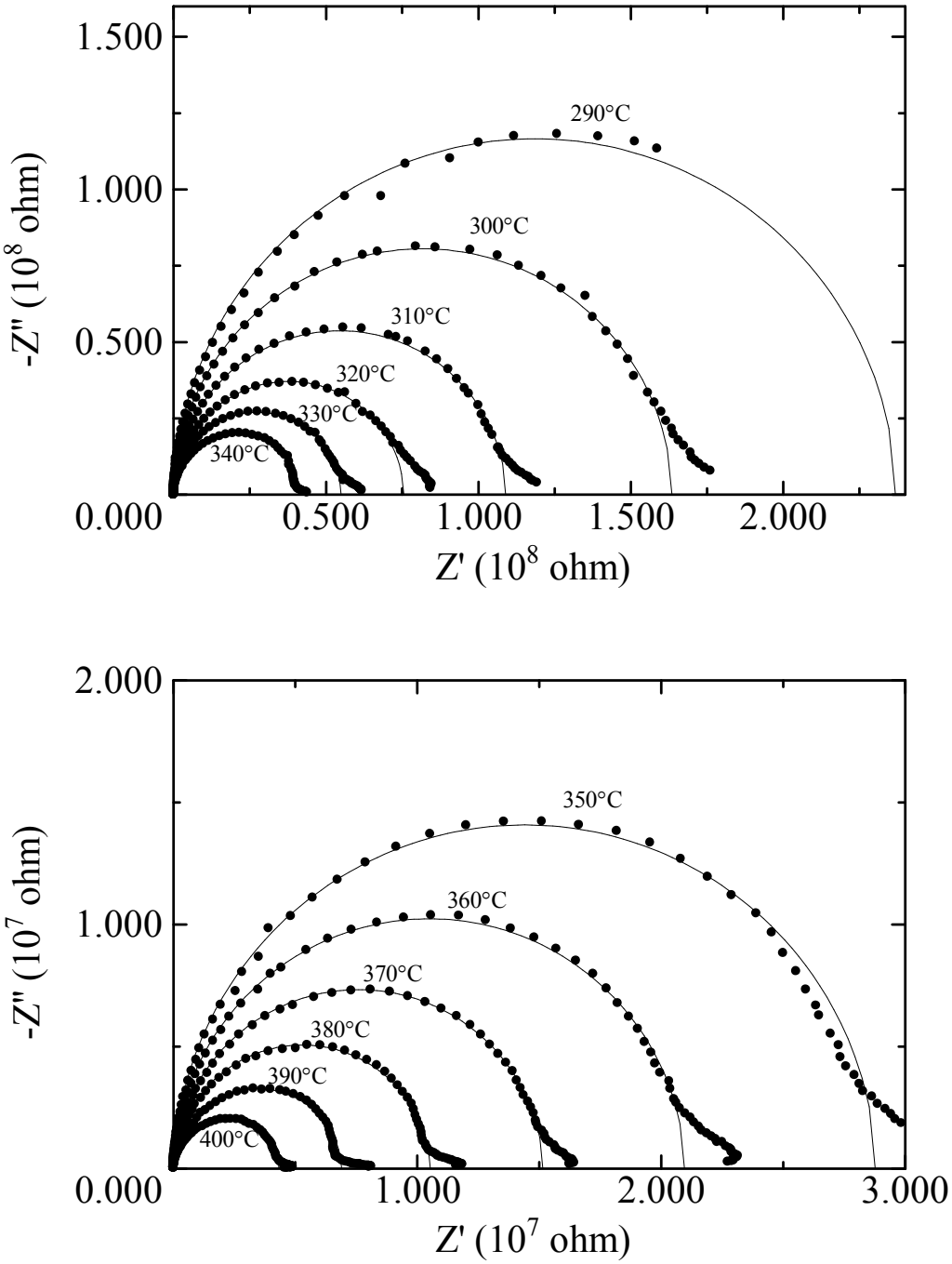

Figure 1.22 Complex impedance plots for $15Nb_2O_5 \cdot 85TeO_2 \cdot 0.5Na_2O$ glass with 2.350 mm thick and the electrode area of 0.7472 cm^2. The solid curves are the least squares line fits.

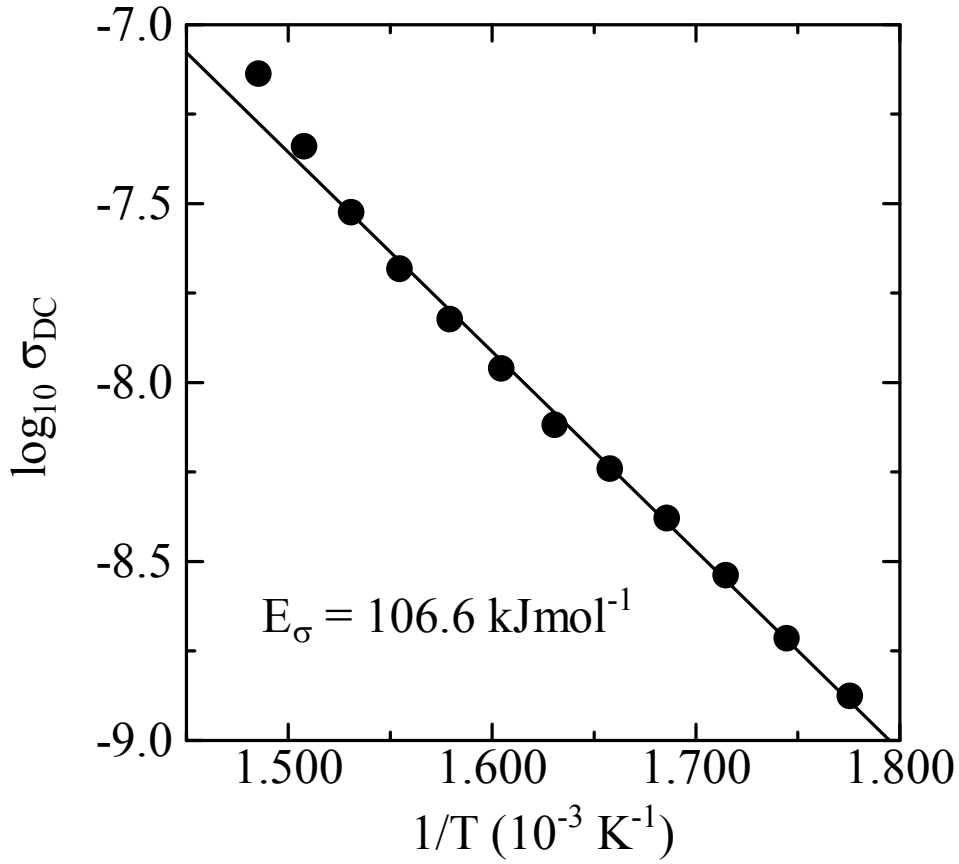

Figure 1.23 Temperature dependence of the DC conductivity for $15Nb_2O_5 \cdot 85TeO_2 \cdot 0.5Na_2O$ glass with the thickness of 2.350 mm and the electrode area of 0.7472 cm^2. The solid lines are the least squares straight line fit.

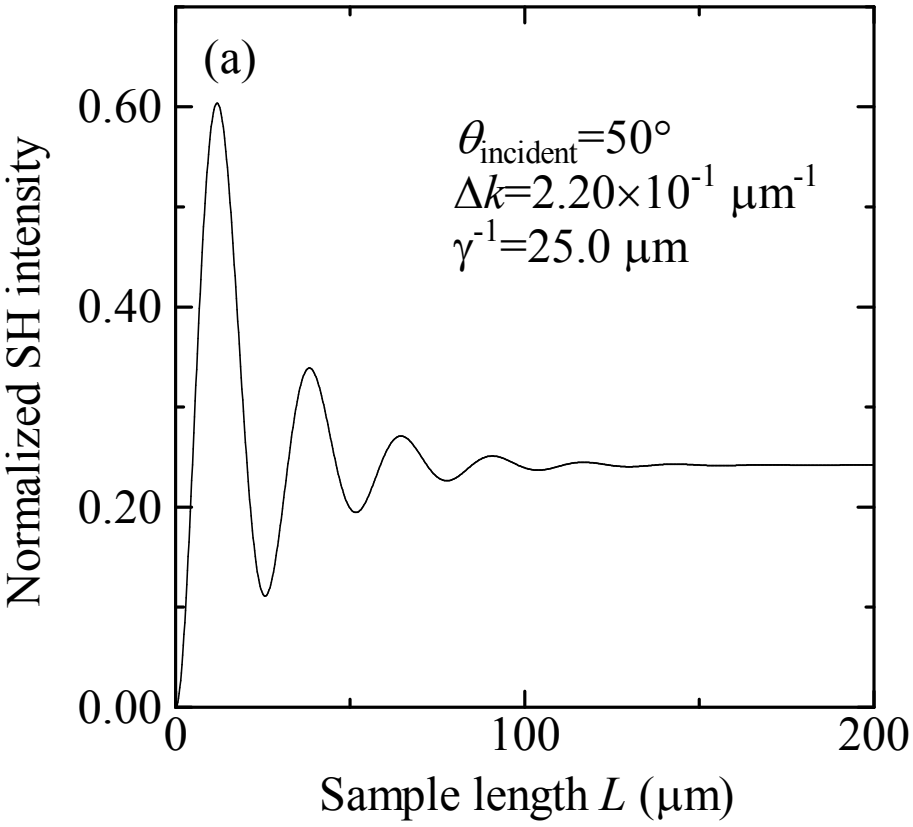

Figure 1.24 (a) SH intensity calculated as a function of L. The conditions used for the calculation are also shown. The SH intensity is normalized with the value obtained under the assumption that $d_{33}(0)$ is uniform over the sample and the thickness of the sample is equal to the coherence length.

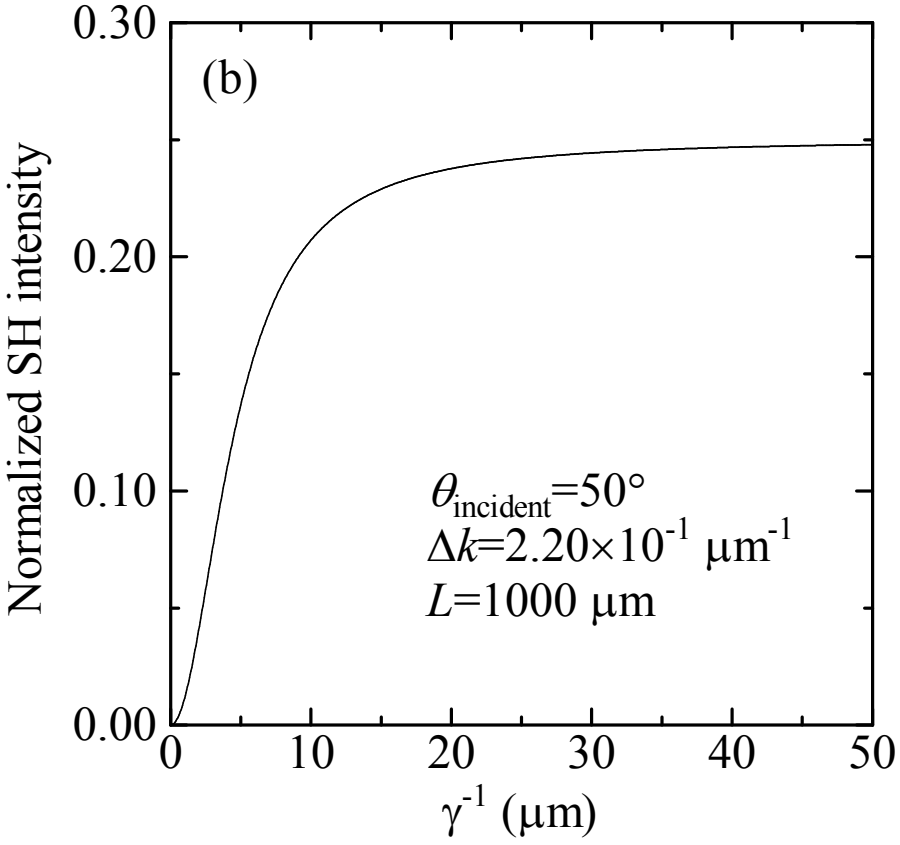

Figure 1.24 (b) SH intensity calculated as a function of γ^{-1}. The conditions used for the calculation are also shown. The SH intensity is normalized with the value obtained under the assumption that $d_{33}(0)$ is uniform over the sample and the thickness of the sample is equal to the coherence length.

Chapter 2 Polarized structure designed by interference laser field

2.1 Influence of optical poling treatment on $\chi^{(2)}$-encoding in V_2O_5-doped tellurite glasses

Introduction

In the previous chapter, $\chi^{(2)}$-induction by sodium-ion doping is demonstrated for $15Nb_2O_5 \cdot 85TeO_2$ glass. The basic policies are

i) Using a medium bearing large $\chi^{(3)}$

ii) Inducing large $\mathbf{E}_{dc}$

The doping procedure provides the second-order nonlinearity as much as $d_{33} \approx 0.2$ pm/V at the anode-side surface. The d-value is comparable with the d_{11} value for α-quartz. However, the output second-harmonic (SH) intensity is extremely low in comparison with the α-quartz despite the large d-value. It is mainly due to the high refractive index of the glass (rf. Eq. 1.28) and the inefficient interference among generated SH-waves (Fig. 1.24). Therefore, it is difficult to obtain a large SH intensity only by selecting a high-index medium from the viewpoint of increasing $\chi^{(3)}$. According to Deparis [1], there is also a limit in increasing $\mathbf{E}_{dc}$ because it is impossible to stabilize a DC field larger than the dielectric breakdown strength $\mathbf{E}_b$. In addition, there are other problems to be solved for practical use of thermally/electrically poled tellurite glass. The major difficulty is the high thermal-expansion coefficient (the order of 10^{-5}-10^{-6}) [2, 3] which causes the fracturing of the medium in a heating or cooling process inevitable for thermal/electrical poling. For these reasons, it is necessary to scheme a novel technique to obtain large output SH intensity. In this chapter, artificial velocity matching between relevant light waves is demonstrated as the second approach for $\chi^{(2)}$-activation.

· Phase-matching technique

The conversion efficiency from a fundamental to the higher-order harmonic wave

repeats a growth and decay against nonlinearly interacting length as shown in Fig. 1.3 with the thin solid line. The parameter l_c described in the figure is called coherence length, which corresponds to the minimum length showing the most intense SH output. Because l_c is determined only by n_ω and $n_{2\omega}$, it is the unique value for each material. In Eq. 1.28, the oscillation behavior is represented by the squared sampling function $\mathrm{sinc}^2(\Delta kL/2)$ which is called phase mismatch factor. Every l_c, a phase shift of π has accumulated in the phase mismatch factor. Since the mismatch factor exhibits rapid decay with increasing L, the benefit by elongating the interacting length L is completely canceled out. Such wasted factor originates in the fact that a finite Δk generates the continuous phase slip between incident ω and generated 2ω waves, so that a harmonic wave generated at a certain position is canceled out by another harmonic wave with opposite phase generated some distance ahead. Inversely speaking, if $n_\omega = n_{2\omega}$ ($\Delta k = 0$) is satisfied in some way, quadratical amplification is expected for the output SH intensity by elongating the interacting length. Franken et al. suggested such a phase corrective scheme called “phase matching” as a breakthrough against the limitation of artificially encoded $\chi^{(2)}$. Phase matching is categorized into i) perfect phase-matching or ii) quasi-phase-matching (QPM) by the way of correction.

Perfect phase-matching

Perfect phase-matching is a very powerful technique for an anisotropic crystal with a large birefringence. If suitable polarization and traveling direction are selected for each interacting light, the index-matching ($n_\omega = n_{2\omega}$) is accomplished [4]. Then, the generated SH field grows linearly with an increase in interacting length because the phase mismatching factor becomes unity. That is, SH intensity increases quadratically with the length as shown with the thick solid curve in Fig. 1.3. However, in most media, such a birefringent condition cannot be obtained. In glassy media, such a condition has never been satisfied because of the structural isotropy.

Quasi-phase matching

Quasi-phase matching (QPM) is a sophisticated technique applicable even for isotropic materials in which perfect phase-matching condition cannot be satisfied. This effect was separately suggested by Bloembergen et al. [5] and Franken et al. [6] and firstly observed in optical fibers [7,8]. Since the discovery, great progress has been achieved towards the fabrication of QPM materials [9-12]. Basic concept of QPM is to compensate the phase mismatch among relevant waves with periodic structure so that a constructive phase relationship is maintained. The periodic structure means the modulation of the sign or magnitude of nonlinear coefficient. One example is the structure with periodically-reversed spontaneous polarization P_s (step alternation of $\chi^{(2)}$, Fig. 2.1i)). In a vertical-incidence configuration, the most effective reversing period is the coherence length l_c given by the following equation;

$$\frac{\lambda}{4(n_{2\omega}-n_{\omega})}=\frac{\pi}{\Delta k}=l_c. \tag{2.1}$$

When the sign of $\chi^{(2)}$ is reversed every coherence length, the structure shows the sample-length dependence as in the dashed line of Fig. 1.3. The average efficiency is $(2/\pi)^2$ of the perfectly phase matching case. Higher order QPM conditions are also achieved by changing the d-value after a multiple distance of l_c. If the periodicity is $2n$-1 times of l_c, such condition is called nth-order quasi-phase matching. Complete sign reversal of $\chi^{(2)}$ is not necessarily required for QPM structure. The most important is to give a structural harmonic with the proper wave vector $\Delta k'$ satisfying Eq. 2.2.

$$k_{2\omega}-2k_{\omega}-(2n-1)\Delta k'=0 \tag{2.2}$$

The sufficient condition is the modulation of the nonlinear coefficient, and the sign reversal is a special (and the most efficient) case. Janz et al. reported on a reflective SHG in $Al_xGa_{1-x}As$ multi-layer structure using the modulation of the magnitude of the nonlinear coefficient [21]. The modulating structure is obtained by i) stacking polarized wafers with rotating alternate wafers by 180° as mentioned above [9, 13-16], ii) reflecting relevant light waves after they

have traversed a distance l_c (Fig. 2.1ii)), iii) inducing periodically alternated polarization by applying a periodically reversed electric field [10, 17-20], and iv) using Fabry-Perot interferometer structure [21,22]. In $LiNbO_3$, QPM structure accomplished a conversion-efficiency higher than that achieved by perfect phase-matching since the largest nonlinear coefficient d_{33} can be utilized in QPM. In 1980s, some research groups reported ingenious operation called "optical poling" for constructing periodically inverting structure [23-26]. It is regarded as a powerful technique for designing QPM structure easily. Detail on the optical poling is provided in the next section.

· Optical poling

Optical poling is a skillful technique by which periodically alternating DC field can be applied inside a transparent medium. When collinearly superimposed ω and 2ω beams are incident into a medium, static polarization P_{DC} emerges via a third-order nonlinear process as follows.

$$P_{DC} = \frac{3}{4}\chi^{(3)}(0,-2\omega,\omega,\omega)\left|E_{2\omega}{}^{*}E_{\omega}E_{\omega}\right|\cos(\Delta kz) \tag{2.3}$$

$$\Delta k = k_{2\omega} - 2k_{\omega} \tag{2.4}$$

This equation indicates that a spatially-sinusoidal DC field with $2\pi/\Delta k$ periodicity is applied along the whole laser path if the irradiated material has enough transparency. Because P_{DC} changes the sign every l_c, the optically-poled material automatically satisfies a first-order quasi-phase matching condition. Therefore, an intense SH output is expected for optically poled samples. Since optically poled region is restricted to the seeding-beam path, this procedure is useful for the integration of functional optical circuits and the design of optical memories. The optical poling was attempted for various glassy materials such as Ge-containing silica glass fiber, Ce-doped $PbO\text{-}GeO_2$, $BaO\text{-}B_2O_3\text{-}SiO_2$, $PbO\text{-}SiO_2$, $Bi_2O_3\text{-}B_2O_3\text{-}SiO_2$, and $GeAsS_3$ systems [27-33].

In this section, the effect of vanadium-ion doping on the second-order nonlinearity

encoded by optical poling is investigated for K_2O-Nb_2O_5-TeO_2 glass. The induced second-order nonlinearity is characterized as being related to the optical absorption originated in the doped ions.

Experimental

· Sample preparation

The prepared glass compositions are listed in Table 2.1. These glasses were prepared from reagent-grade TeO_2, Nb_2O_5, K_2CO_3, and V_2O_5 (purities were 99.9 %). The raw materials were mixed thoroughly and melted in a platinum crucible at 850 ˚C for 90 min in air. The melt was poured onto a stainless steal plate and cooled to obtain glass. After the glass thus obtained was annealed at 400 ˚C for 20 min, it was cut into a rectangular parallelepiped by means of a diamond-paste-coated saw. Both surfaces of the glass were polished with sandpaper and CeO_2 powder to obtain a glass sample 1.00 mm thick.

Table 2.1 Composition of V_2O_5-doped tellurite glasses prepared in the present study.

Notation	Composition (molar ratio)			
	Nb_2O_5	TeO_2	K_2O	V_2O_5
-	15.0	85.0		0.01
-	15.0	85.0		0.03
-	15.0	85.0		0.05
-	15.0	85.0		1.00
NTK0	14.9	84.6		0.50
NTK3	14.5	82.0	2.99	0.50
NTK5	14.2	80.3	4.98	0.50
NTK7	13.9	78.7	6.97	0.50
NTK10	13.4	76.1	9.95	0.50
NTK15	12.7	71.9	14.9	0.50

· Optical absorption spectra

Optical absorption spectra of the as-prepared samples were measured at room temperature using a spectrophotometer (Hitachi 330). The absorption coefficient obtained is used for evaluating d-value.

· Optical poling and SHG measurement

A schematic illustration of the setup for optical poling is shown in Fig. 2.2. Optical poling was performed using fundamental (1064 nm) and SH waves (532 nm) of a pulsed Nd-doped yttrium-aluminum-garnet (Nd:YAG) laser (COHERENT, infinity 40-100) which operated in a Q-switched mode. Both beams were, after coaxially superimposed, linearly polarized with a polarizer and used as seeding beams. The seeding beams were focused with a one-side converging lens and normally incident into a sample with the focal point situated slightly over the exit surface of the sample for optical poling. The pulse width and the repetition rate of the laser were 3 ns and 20 Hz, respectively. The laser powers were 5.70 $kWcm^{-2}$ at 1064 nm and 0.191 $kWcm^{-2}$ at 532 nm for the V_2O_5-doped $15Nb_2O_5{\cdot}85TeO_2$ glasses, and 143 Wcm^{-2} at 1064 nm and 15.0 Wcm^{-2} at 532 nm for the V_2O_5-doped K_2O-Nb_2O_5-TeO_2 glasses. Optical poling lasted for 10 min. The ecncoded second-order nonlinearity was characterized by SHG measurement using the same setup. Only the fundamental wave was incident into a sample for probing and generated SH signal was detected by a photomultiplier connected to an oscilloscope. The maximum SH intensity in a Y-cut α-quartz plate 1.046 mm thick was used for evaluating the optically encoded second-order nonlinearity using the next equation.

$$d_{\mathrm{s,surface}} = 2d_{\mathrm{eff,q}} \frac{L_{\mathrm{q}}}{L_{\mathrm{s}} \cos\theta_{2\omega,\mathrm{q}}} \frac{n_{\omega,\mathrm{s}}}{n_{\omega,\mathrm{q}}} \left(\frac{n_{2\omega\mathrm{s}}}{n_{2\omega,\mathrm{q}}} \right)^{\frac{1}{2}} \left(\frac{T_{\mathrm{q}}}{T_{\mathrm{s}}} \right)^{\frac{1}{2}} \frac{I_{\omega,\mathrm{q}}}{I_{\omega,\mathrm{s}}} \left(\frac{I_{2\omega,\mathrm{s}}}{I_{2\omega,\mathrm{q}}} \right)^{\frac{1}{2}} \tag{2.5}$$

T is transmittance. The subscripts s and q mean the value for the sample and the quartz, respectively. Equation 2.5 is valid only for the medium with the d-value profile of

$$d(z) = d(0)\exp\left(-\frac{\alpha z}{2}\right)\cos(\Delta kz + \phi), \tag{2.6}$$

which is satisfied in optically poled materials.

· Complex refractive index

In order to check the vanadium-derived abnormal dispersion in refractive index, ellipsometry was performed for the 0.7 mol% V_2O_5-doped $15Nb_2O_5{\cdot}85TeO_2$ glass sample at room temperature using the M-2000, Woollam. The Stokes parameters Ψ and Δ were measured across the UV-vis wavelength range (250-700 nm). Incident angle was fixed at 74.5°. The measured Ψ and Δ were converted to complex refractive indices using a Gaussian oscillator model which involves the contribution from strongly inhomogeneous broadening.

· Electron spin resonance (ESR) spectroscopy

To investigate the valence state of the doped vanadium ions, ESR spectroscopy was performed for the V_2O_5-doped samples at room temperature using a commercial measurement system (ESP300E, Bruker). The frequency and the power of microwave were 9.626 GHz (X-band) and 1.00 mW, respectively. To trace the electronic-state change during the optical poling, the bulky 1.00 mol% V_2O_5-doped $15Nb_2O_5{\cdot}85TeO_2$ glass was subjected to ESR measurement under the irradiation of the SH wave of a cw Nd-doped yttrium-lithium-fluoride (Nd:YLF) laser (523 nm). It is expected that the laser irradiation gives rise to the same situation as optical poling. ESR spectrum was measured every few minutes during the laser irradiation and after ceasing the irradiation. To check the composition dependence of the electronic state, 0.14 g of the milled V_2O_5-doped K_2O-Nb_2O_5-TeO_2 glass samples were subjected to ESR measurement without laser irradiation.

Results

Nb_2O_5-TeO_2 system

Optical absorption spectra

Figure 2.3(a) shows the optical absorption spectra for the $15Nb_2O_5 \cdot 85TeO_2$ glass samples. The intense absorption at less than 550 nm is attributable to the charge-transfer transition in V^{5+}-O^{2-} bond. Absorption lines ascribable to other valence states are not observed in the spectra. As V_2O_5 amount increases, the wavelength showing remarkable absorption becomes longer. The absorption coefficient at 2ω frequency linearly increases with V_2O_5 amount (Fig. 3.2(b)).

· Complex refractive index

The result of ellipsometry for the 0.7 mol% V_2O_5-doped sample is shown in Fig. 2.4. The above diagram (a) presents the measured Stokes parameters Ψ and Δ, and the below (b) is the simulated dispersion in complex refractive index $n + ik$. The abnormal dispersion in nonlinear susceptibilities cannot be observed. The obtained values were used for d-value calculation.

· Time variation in SH intensity

The vanadium-free sample scarcely showed SHG even when optical poling was performed for a long period. On the other hand, all the V_2O_5-doped samples became SHG-active after the optical poling. Figure 2.5 depicts the time variation in SH intensity relative to the standard. At a period shorter than 150 s, SH intensity becomes larger as V_2O_5-content increases. However, at a period longer than 200 s, SH intensity for the 1.00 mol% V_2O_5-doped sample is less than that for the 0.05 mol% doped one. Namely, the decay rate is more rapid for the sample containing much amount of V_2O_5. The inset of Fig. 2.5 shows the $d_{s,surface}$ calculated from Eq. 2.5. The sample doped with 1.00 mol% V_2O_5 exhibits the d-value as much as 1.6 pm/V.

· ESR spectroscopy

Figure 2.6 shows the ESR spectra for the 1.00 mol% V_2O_5-doped $15Nb_2O_5 \cdot 85TeO_2$ glass. The dashed and solid lines correspond to the data measured before and after the 10 min Nd:YLF laser irradiation. The whole signal seen in the figure is ascribed to VO^{2+} (V^{4+}) ion which is not recognized in the optical absorption spectrum. The inset of Fig. 2.6 is the difference spectrum. From these spectra, it is clarified that the Nd:YLF laser irradiation reduces the number of VO^{2+} ion.

Figure 2.7 shows the time variation in ESR peak area ascribable to VO^{2+} ion. The peak area is normalized with the initially measured value. During the laser irradiation, VO^{2+} peak area exponentially converges to a constant value. After ceasing the laser irradiation, it recovers to the level before the irradiation. Figure 2.8 is a laser-power dependence of the decrease in the VO^{2+} peak area which is normalized with the intensity before the laser irradiation. The dashed line is the least square curve fitted with

$$\Delta I / I \propto P_{523\mathrm{nm}}^{m}, \tag{2.7}$$

where $P_{523\mathrm{nm}}$ and m are laser power and the fitting parameter, respectively. From the fitting, $m = 2.0$ was obtained.

<u>K_2O-Nb_2O_5-TeO_2 system</u>

· Optical absorption spectra

Figures 2.9(a) shows the optical absorption spectra for the K_2O-Nb_2O_5-TeO_2 glass samples. In Fig. 2.9(b), the absorption coefficient at 2ω frequency (532 nm) is plotted against K_2O content. V_2O_5-doping brings about intense absorption at the wavelengths shorter than 550 nm which is attributable to the charge-transfer transition in V^{5+}-O^{2-} bond. Absorption lines ascribable to other valence states are not observed. As K_2O content increases, absorption edge shifts to shorter wavelength. In response to the blue-shift, the absorption coefficient at 532 nm decreases.

· Optical poling and SHG measurement

Figure 2.10 shows the SH intensity 30 s after ceasing the seeding 2ω beam. SH intensity is apt to increase with an increase in K_2O content below 5 mol% K_2O. As K_2O content increases, SH intensity starts to decrease.

· Electron spin resonance (ESR) spectroscopy

ESR spectra for the K_2O-Nb_2O_5-TeO_2 glass samples are shown in Fig. 2.11. A complicated peak attributed to VO^{2+} ion can be seen. In the inset of the figure, the peak area is plotted against K_2O content. The increase in K_2O ratio reduces VO^{2+} amount.

Discussion

<u>$15Nb_2O_5{\cdot}85TeO_2$ glass doped with V_2O_5</u>

As shown in Fig. 2.5, an intense SH intensity, as much as one hundredth of that for the α-quartz, is achieved in optically poled $15Nb_2O_5{\cdot}85TeO_2$ glasses by V_2O_5 doping. The relative SH intensity is two orders larger than the case of thermally/electrically poled samples in spite that the d-values are not so different. The amplification of SH output probably came from the pseudo-phase matching structure established by optical poling. Figure 2.5 shows that vanadium ion plays an important role in $\chi^{(2)}$-induction. From the optical absorption spectra, it is found that there are pentavalent vanadium ions in the tellurite glass matrix. Meanwhile, ESR spectra assure the existence of tetravalent vanadium ions. Even if pentavalent vanadium ions exist, they are undetectable with ESR spectroscopy because the pentavalent vanadium ion has no unpaired electron. On the other hand, tetravalent vanadium ion should be confirmed in the absorption spectra if exists because it causes the absorption lines at 420, 760-860, and about 1000 nm [34]. Despite the fact, the corresponding absorption is not confirmed in the present absorption spectra, which shows that in the $15Nb_2O_5{\cdot}85TeO_2$ glass matrix, most vanadium ions take pentavalent state and the remaining small amount is present as tetravalent state. The small amount of V^{4+} ion is further reduced by intense 523 nm light irradiation (Fig. 2.6). This means that the Nd:YLF laser irradiation

induces photo-oxidation of tetravalent vanadium ions by withdrawing an electron. The released electron was considered to be trapped at certain levels. A similar photochemical reaction is expected to occur during optical poling because the V_2O_5-doped samples also exhibit a small absorption at the wavelength of the seeding 2ω beam (532 nm). The generated electrons and the remaining V^{5+} ion, i.e., a positive hole trapped at the V^{4+} site can contribute to electric-dipole formation if they are oriented along with an applied filed. The time decay in SH intensity (Fig. 2.5) reflects the recovering in V^{4+} amount as in Fig. 2.7. Figure 2.8 shows that the decrease in ESR peak area for VO^{2+} ion caused by the Nd:YLF laser irradiation. The decreased area is approximately parabolic against laser power, which implies that the photochemical reaction from V^{4+} ion to V^{5+} ion is a two-step photon process. From the discussion so far, it is speculated that during optical poling, a two-step photon process which involves the charge-transfer transition in V^{5+}-O^{2-} bond occurs in parallel with the optical rectification process.

K_2O-Nb_2O_5-TeO_2 glass doped with V_2O_5

In Fig. 2.12, calculated $d_{s,surface}$ is plotted against absorption coefficient at 532 nm. This graph roughly shows that larger absorption coefficient leads to larger d-value. In intense absorption area, the d-value seems smaller than expected, which is possibly related with the decay rate of SH intensity. Because the decay rate is thought to be faster in intense absorptive media, the obtained d-values is underestimated.

In optically poled K_2O-Nb_2O_5-TeO_2 glass, the output SH intensity is influenced by two factors. One is related with optical absorption and the other is the amount of V^{4+} ion originally present in as-prepared glass. The former gives rise to the suppression of the optically poled volume (cf. Eq. 2.6) and re-absorption of the SH wave generated in the sample. In the low K_2O-containing samples, SH intensity seems weak compared with the d-value, which probably comes from the large optical absorbance. Meanwhile, the influence of the latter factor appears in high K_2O-containing composition. In general, multivalent cations such as transition-metal ions are apt to take oxidized states when the basicity of the glass increases. In the present case, K_2O increases the basicity of the glass. Hence, it is

considered that V^{4+} ion decreases as K_2O increases. This speculation is consistent with the results in the inset of Fig. 2.11. K_2O addition decreases the ESR peak area corresponding to VO^{2+} ion. The weak SH intensity observed for the high K_2O containing glass is partly due to the small concentration of V^{4+} ion as well as the small absorption coefficient.

· $\chi^{(2)}$-induction mechanism of optically poled V_2O_5-containing tellurite glass

The experimental results in this section give a possible mechanism of $\chi^{(2)}$-induction by optical poling as shown in Fig. 2.13. When a V_2O_5-containing glass is irradiated with the seeding 2ω beam, electrons are excited from the valence band presumably composed of 2p orbital of oxide ions to vacant 3d orbital of V^{5+} ions, and then further excited to the conduction band of the glass matrix (two-step photon process). The electrons and the positive holes thus appeared are, after drifting along with the DC field made by the seeding beams, trapped at certain sites and V^{4+} ions, respectively. The trapped charged species construct the polarized structure with the sinusoidal periodicity as in GeO_2-containing silica glass fiber [35,36]. It is predicted so far that the glass materials doped with multivalent rare-earth or transition-metal ions potentially led to large second-order nonlinearity caused by mixed-valence character of the ions [37,38]. Chen and coworkers found more direct relationship between optical absorption and second-order nonlinearity [39]. According to them, the theoretical expressions for $\chi^{(2)}$ and absorption coefficient have similar denominators. The commonality results in the similar behavior against wavelength; both increase or decrease simultaneously. Veres et al. also suggested the close relationship between optical absorption and $\chi^{(3)}$ [40]. These results are based on the explosive $\chi^{(2)}$ enlargement caused by abnormal dispersion. However in the present case, the experimental results prove the importance of electron release triggered by photochemical reaction. The fast decay in SH intensity was due to the short lifetime of the induced electronic structure. It is also considered that the relaxation was further accelerated by the irradiation of the fundamental wave used for probing SHG. Si et al. found that the decay in SH intensity for optically poled $10GeO_2 \cdot 90SiO_2$ glass was mainly due to the erasure of induced second-order nonlinearity by the fundamental-wave irradiation [41]. A similar phenomenon took place in

the V_2O_5-doped $15Nb_2O_5{\cdot}85TeO_2$ glass. In particular, the effect of heat was significant in this case because the nanosecond pulsed laser was used; an increase in temperature can accelerate the relaxation of electronic defects.

Conclusion

Large second-harmonic output coming from a pseudo-phase matching condition is successfully obtained from optically poled Nb_2O_5-TeO_2 and K_2O-Nb_2O_5-TeO_2 glass doped with V_2O_5, although the SH intensity decays rapidly. The SH intensity immediately after optical poling is two orders larger than the case of thermal/electrical poling. In addition, for the Nb_2O_5-TeO_2 glass, SH intensity increases with V_2O_5 increasing. The optically encoded SHG is attributable to the formation of a periodic polarized structure made of charged species appearing via a photo-ionization reaction of doped vanadium ions.

References in Section 2.1

[1] O. Deparis, F. P. Mezzapesa, C. Corbari and P. G. Kazansky, Proc. IEEE/LEOS, (2005) p. 177.

[2] J. E. Stanworth, Nature, 169 (1952) p. 581.

[3] Z. Congshan, L. Xiaojuan and Z. Zuyi, J. Non-Cryst. Solids, 144 (1992) p. 89.

[4] P. D. Maker, R. W. Terhune, M. Nisenoff and C. M. Savage, Phys. Rev. Lett., 8 (1962) p. 21.

[5] J. A. Armstrong, N. Bloembergen, J. Ducuing and P. S. Pershan, Phys. Rev., 127 (1962) p. 1918.

[6] P. A. Franken and J. F. Ward, Rev. Mod. Phys., 35 (1963) p. 23.

[7] U. Österberg and W. Margulis, Opt. Lett., 11 (1986) p. 516.

[8] U. Österberg and W. Margulis, Opt. Lett., 12 (1987) p. 57.

[9] M. Okada, K. Takizawa and S. Ieiri, Opt. Commun., 18 (1976) p. 331.

[10] J. Webjorn, V. Pruneri, P. St. J. Russell and D. C. Hanna, Electron. Lett., 31 (1995) p. 669.

[11] V. Pruneri, S. D. Butterwoth and D. C. Hanna, Opt. Lett., 21 (1996) p. 390.

[12] W. R. Bosenberg et al., Opt. Lett., 21 (1996) p. 1336.

[13] M. S. Piltch, C. D. Cantrell and R. C. Sze, J. Appl. Phys., 47 (1976) p. 3514.

[14] A. Szilagyi, A. Hordvik and H. Schlossberg, J. Appl. Phys., 47 (1976) p. 2025.

[15] D. E. Thompson, J. D. McMullen and D. B. Anderson, Appl. Phys. Lett., 29 (1976) p. 113.

[16] D. H. Jundt, G. A. Magel, M. M. Fejer and R. L. Byer, Appl. Phys. Lett., 59 (1991) p. 2657.

[17] B. F. Levine, C. G. Bethea and R. A. Logan, Appl. Phys. Lett., 26 (1975) p.375

[18] J. Webjorn, V. Pruneri, P. St. J. Russell, J. R. M. Barr and D. C. Honna, Electron. Lett., 30 (1994) p. 894.

[19] M. Yamada, N. Nada, M. Saitoh and K. Watanabe, Appl. Phys. Lett., 62 (1993) p. 435.

[20] E. J. Lim, M. M. Fejer and R. L. Byer, Electron. Lett., 25 (1989) p. 174.

[21] S. Janz, C. Fernando, H. Dai, F. Chatenoud, M. Dion and R. Normandin, Opt. Lett., 18 (1993) p. 589.

[22] T. Pertsch, U. Peschel and F. Lederer, Opt. Lett., 28 (2003) p. 102.

[23] M. E. Fermann, L. Li, M. C. Farries, L. J. Poyntz-Wright and L. Dong, Opt. Lett., 14 (1989) p. 748.

[24] M.-V. Bergot, M. C. Farries, M. E. Fermann, L. Li, L. J. Poyntz-Wright, P. St. J. Russell and A. Smithson, Opt. Lett., 13 (1988) p. 592.

[25] M. E. Fermann, L. Li, M. C. Farries and D. N. Payne, Electron. Lett., 24 (1988) p. 894.

[26] P. Chmela, Opt. Lett., 16 (1991) p.443.

[27] R. H. Stolen and H. W. K. Tom, Opt. Lett., 12 (1987) p. 585.

[28] H. Hosono, Y. Abe, D. L. Kinser, R. A. Weeks, K. Muta and H. Kawazoe, Phys. Rev. B, 46 (1992) p. 11445.

[29] E. M. Dianov, D. S. Starodubov and A. A. Izyneev, Opt. Lett., 19 (1994) p. 936.

[30] Y. Nageno, J. H. Kyung and N. M. Lawandy, Opt. Lett., 20 (1995) p. 2180.

[31] J. Si, K. Kitaoka, J. Qiu, T. Mitsuyu and K. Hirao, Opt. Lett., 24 (1999) p. 911.

[32] J. Si, Y. Kondo, J. Qiu, K. Kitaoka, N. Sugimoto, T. Mitsuyu and K. Hirao, Opt. Commun., 180 (2000) p. 179.

[33] J. Qiu, J. Si and K. Hirao, Opt. Lett., 26 (2001) p. 914.

[34] H. A. El Batal and N. A.Ghoneim, Nucl. Instrum. Methods Phys. Res. B, 124 (1997) p. 81.

[35] Stolen R. H. and Tom H. W. K., Opt. Lett., 12 (1987) p.585.

[36] Dianov E. M., Kazanskii P. G. and Stepanov D. Yu, Sov. J. Quantum Electron., 19 (1989) p. 575.

[37] D. M. Krol and J. R. Simpson, Opt. Lett., 16 (1991) p. 1650.

[38] E. Snitzer, J. Less-Common Met., 148 (1989) p. 45.

[39] Tian-Jie Chen, R. N. Zitter and R. Tao, Phys. Rev. A, 51 (1995) p. 706.

[40] G. Veres, S. Matsumoto, Y. Nabekawa and K. Midorikawa, Appl. Phys. Lett., 81 (2002) p. 3714.

[41] J. Si, K. Kitaoka, T. Mitsuyu and K. Hirao, Opt. Lett., 24 (1999) p. 911.

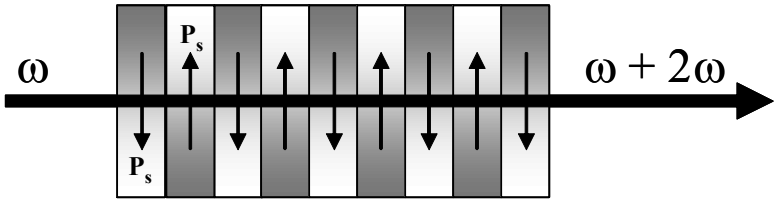

i) Stacking of nonlinear optical media, rotating every odd number of l_c thick.

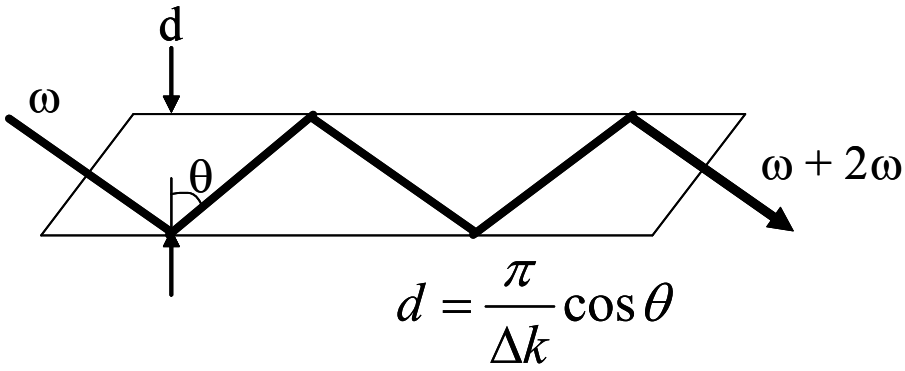

ii) Reflecting both light waves after they have traversed coherence length l_c. The generated harmonic wave undergo an phase shift of π on each reflection.

Figure 2.1 Method for achieving quasi-phase-matched condition.

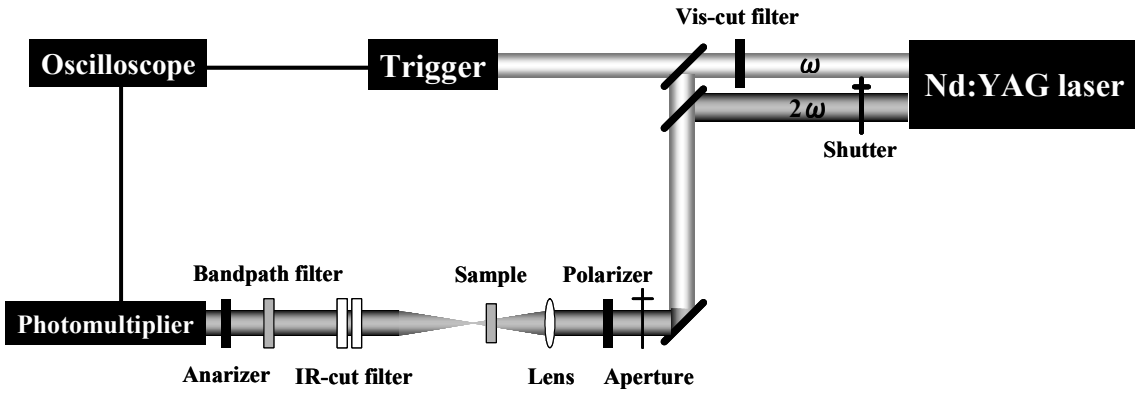

Figure 2.2 A schematic illustration of the setup for optical poling and SHG measurement.

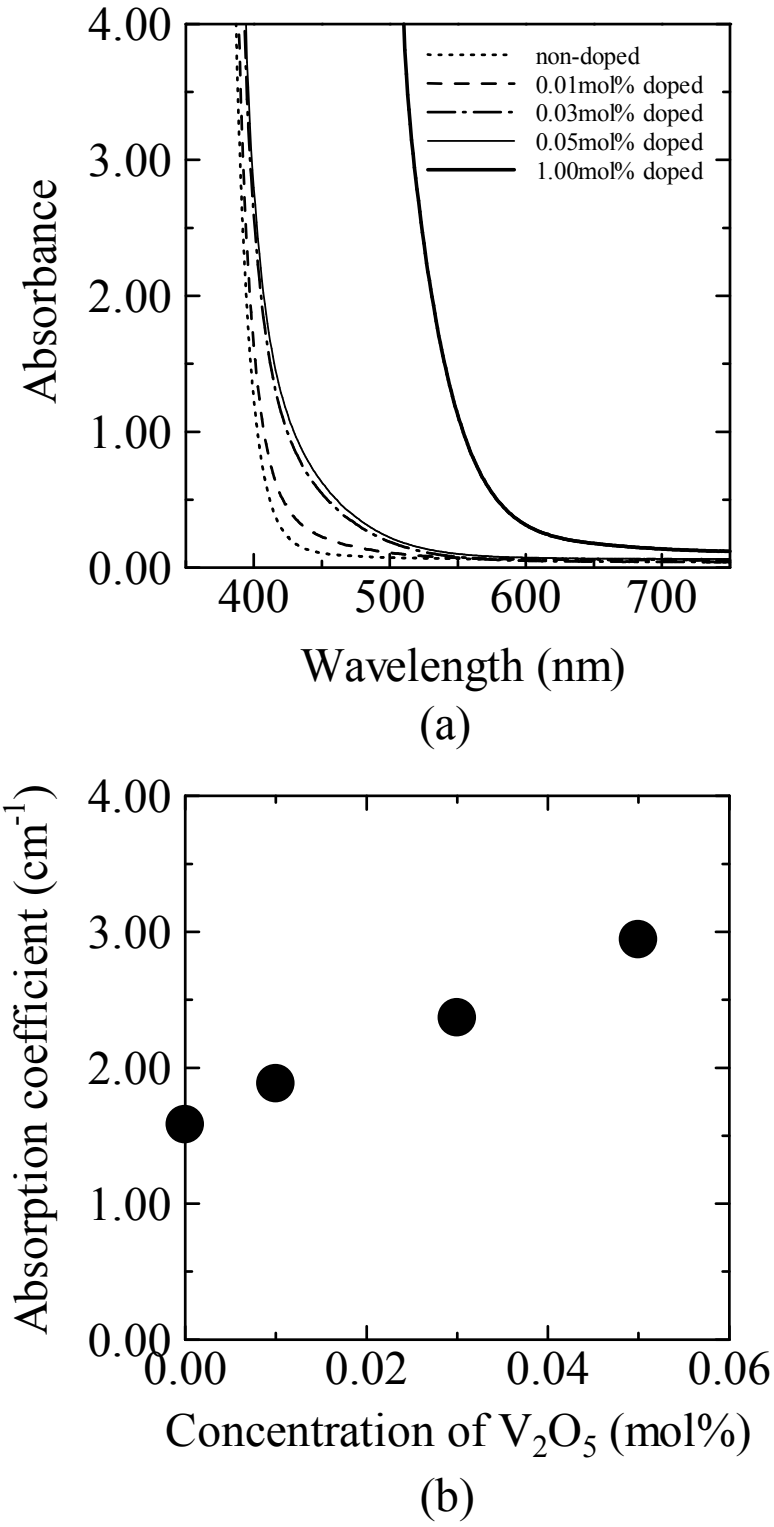

Figure 2.3 Optical absorption properties of V_2O_5-doped $15Nb_2O_5{\cdot}85TeO_2$ glass. (a) is the optical absorption spectra and (b) absorption coefficient at 2ω wavelength (532 nm).

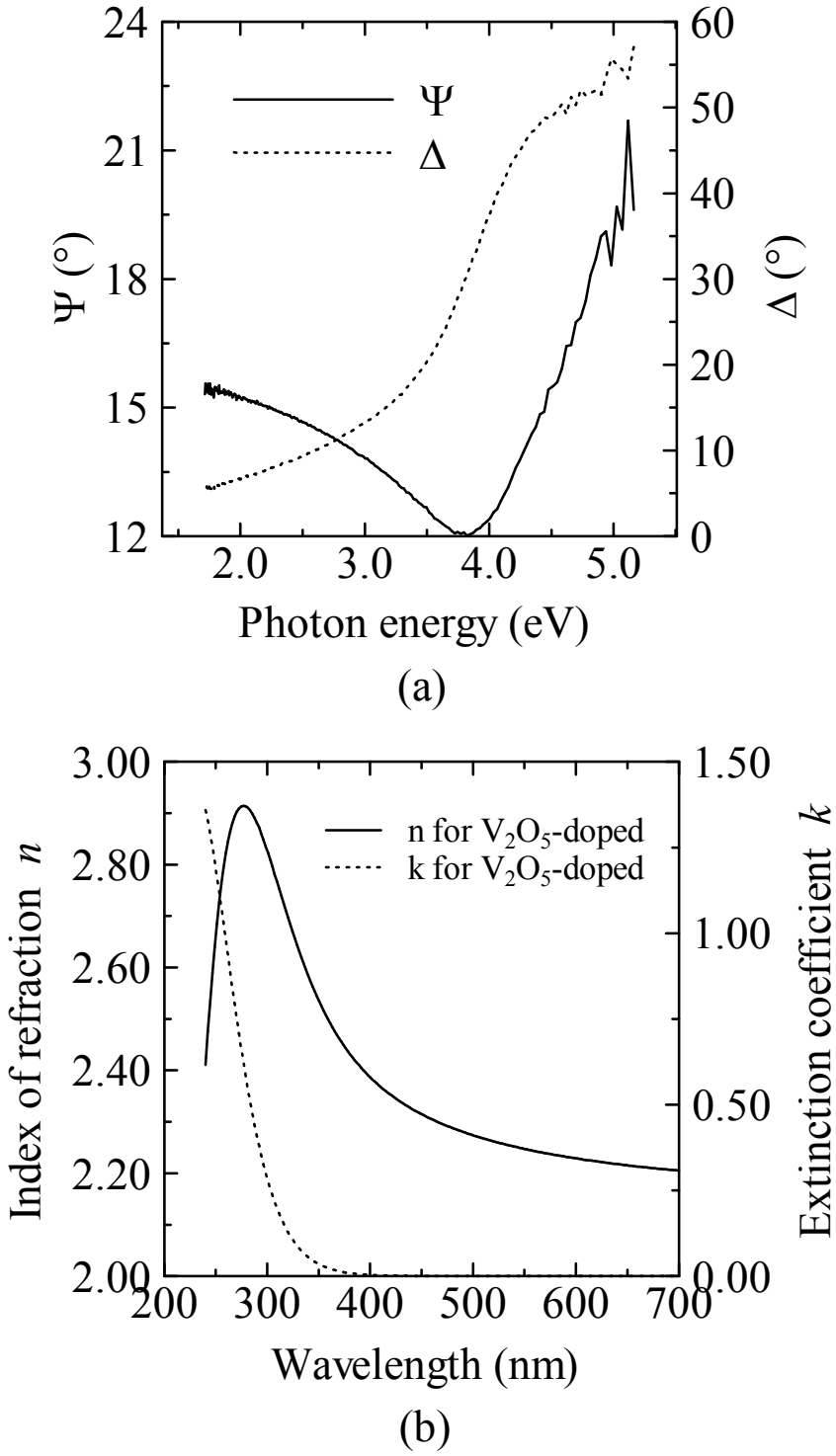

Figure 2.4 The results of ellipsometry measurements for the 0.7 mol% V_2O_5-doped $15Nb_2O_5{\cdot}85TeO_2$ glass sample. The above diagram (a) shows the Stokes parameters Ψ and Δ and the below (b) wavelength dispersion in complex refractive indices $n + ik$.

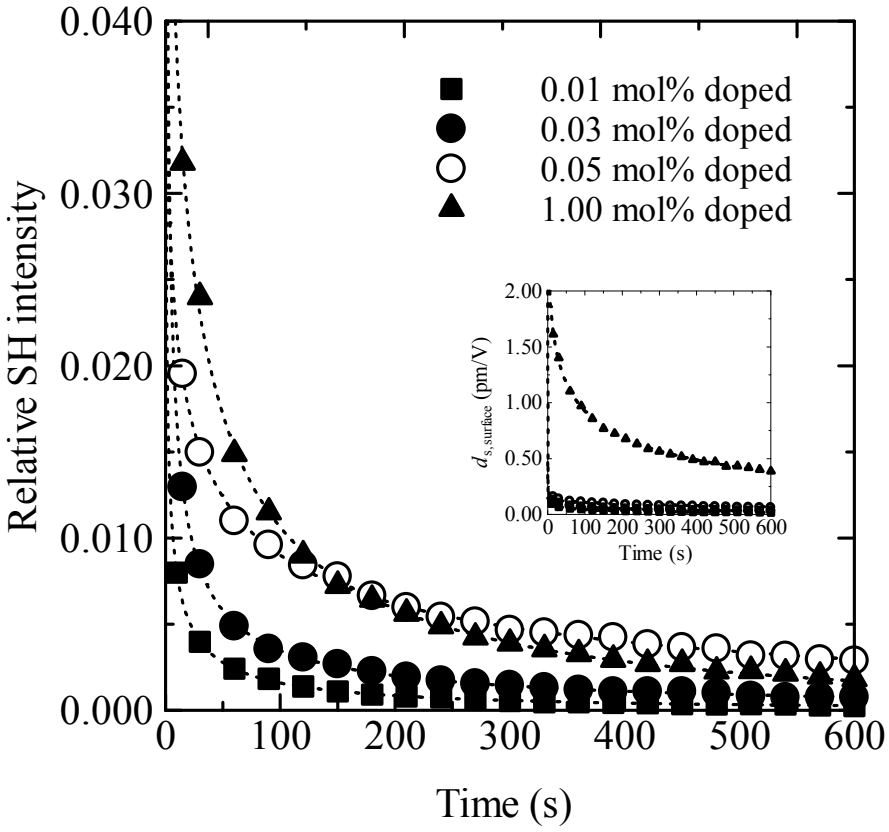

Figure 2.5 Time variation of SH intensity from the V_2O_5-doped $15Nb_2O_5 \cdot 85TeO_2$ glass samples after ceasing optical poling. Relative SH intensity to the maximum SH intensity in Y-cut α-quartz is taken in the vertical. The inset is the effective d-value at the incidence surface which is calculated from the relative SH intensity.

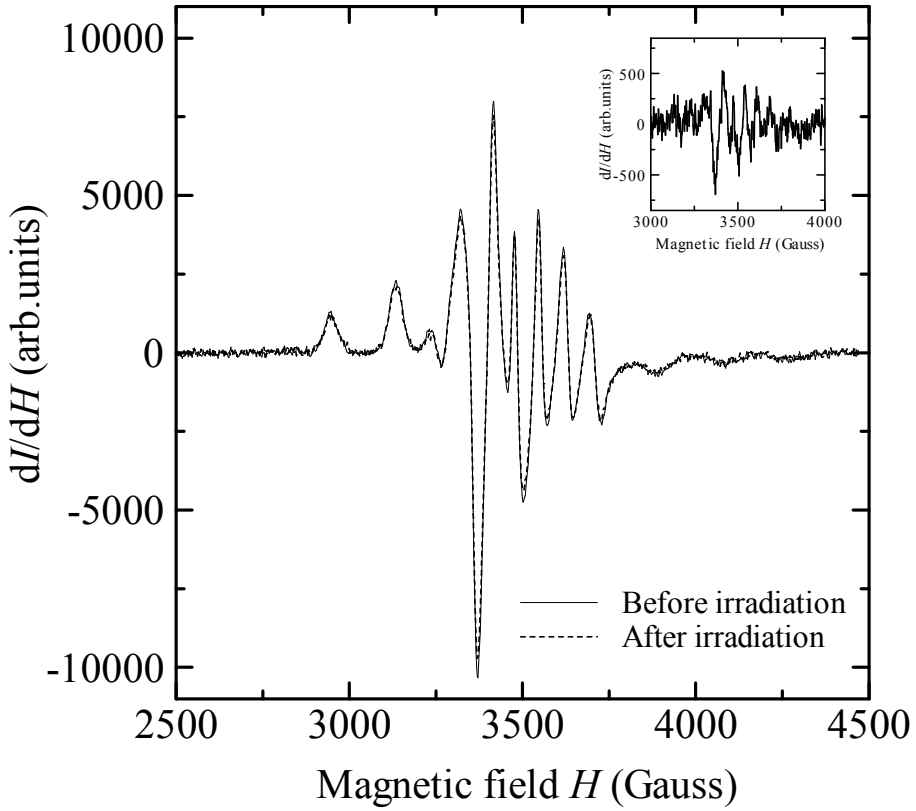

Figure 2.6 ESR spectra for the 1.00 mol% V_2O_5-doped $15Nb_2O_5 \cdot 85TeO_2$ glass sample. The solid line corresponds to the data for a raw sample, and the dashed line to the sample exposed to Nd:YLF laser. The inset shows the differential spectrum between them.

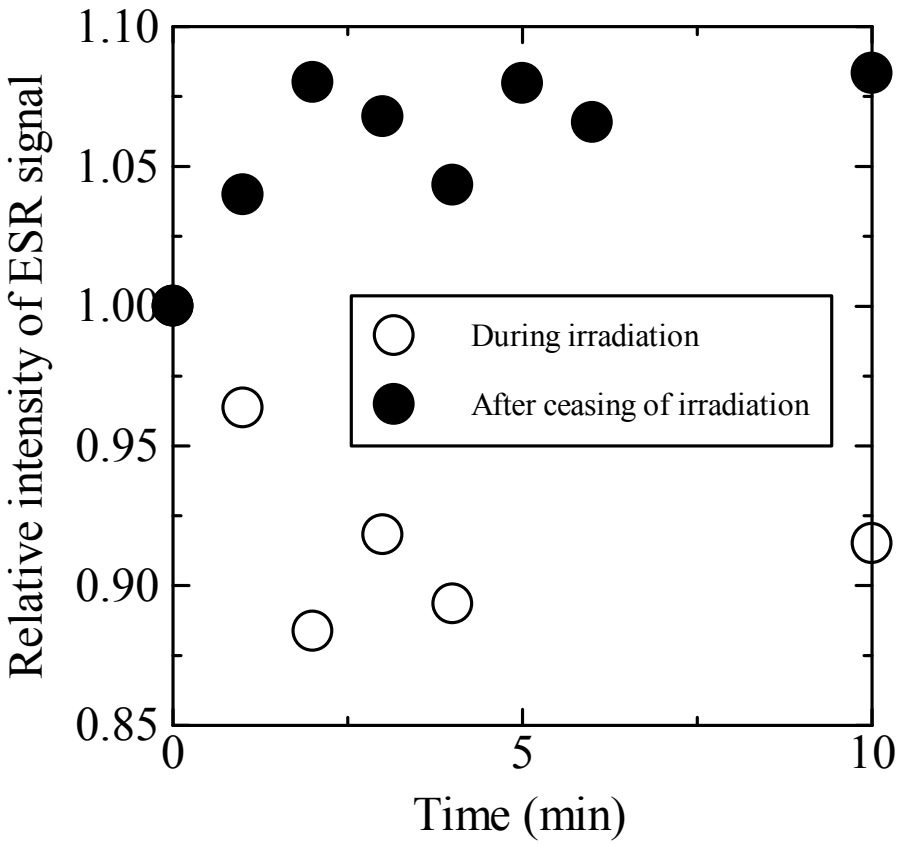

Figure 2.7 Time variation of ESR peak area for VO_4^{2+} ions in 1.00 V_2O_5-doped $15Nb_2O_5 \cdot 85TeO_2$ glass sample. Open circle shows the variation during Nd:YLF laser irradiation, and closed circles that after 10 min irradiation.

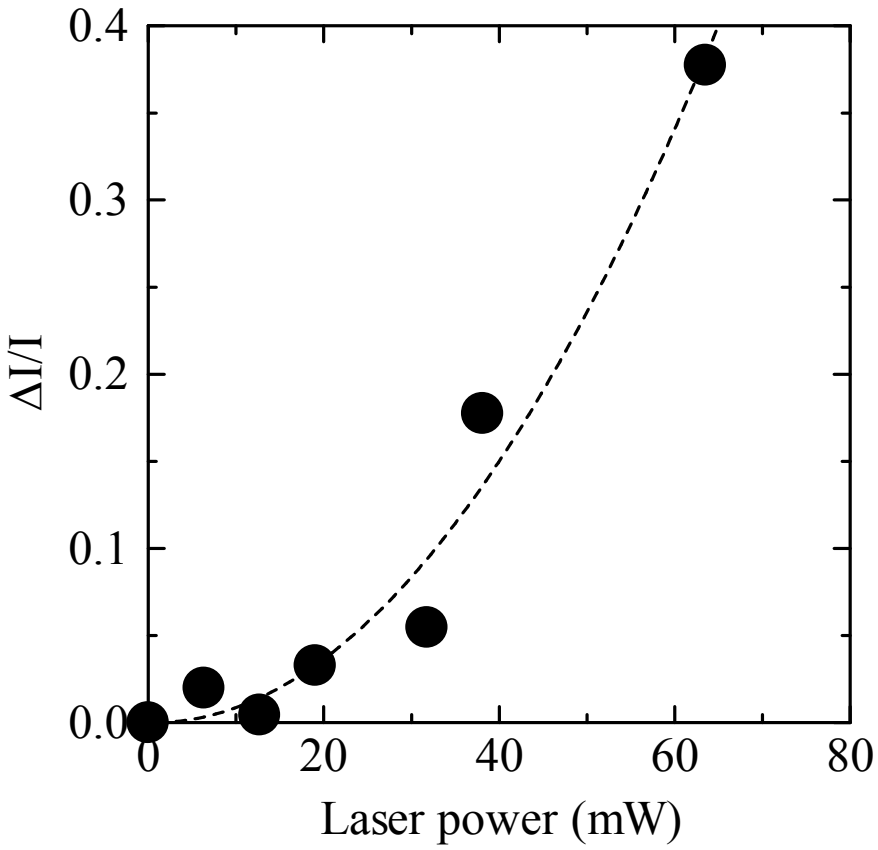

Figure 2.8 Nd:YLF laser power dependence of the decrease in ESR peak area corresponding to VO^{2+} ion in the 1.00 V_2O_5-doped $15Nb_2O_5 \cdot 85TeO_2$ glass sample. The dashed line is the fitted power function curve.

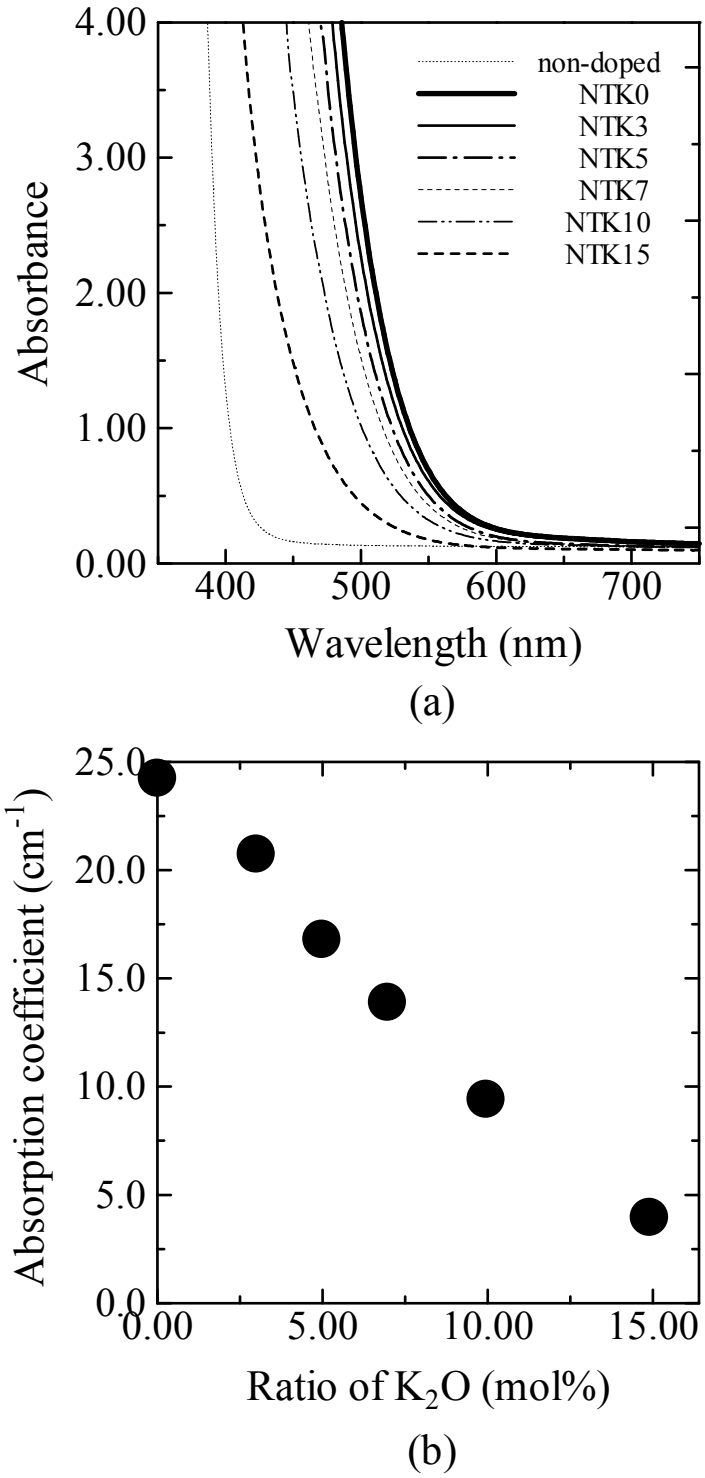

Figure 2.9 Optical absorption properties of the 0.5 mol% V_2O_5-doped K_2O-Nb_2O_5-TeO_2 glass samples. (a) is optical absorption spectra and (b) is absorption coefficient at 2ω wavelength (532 nm).

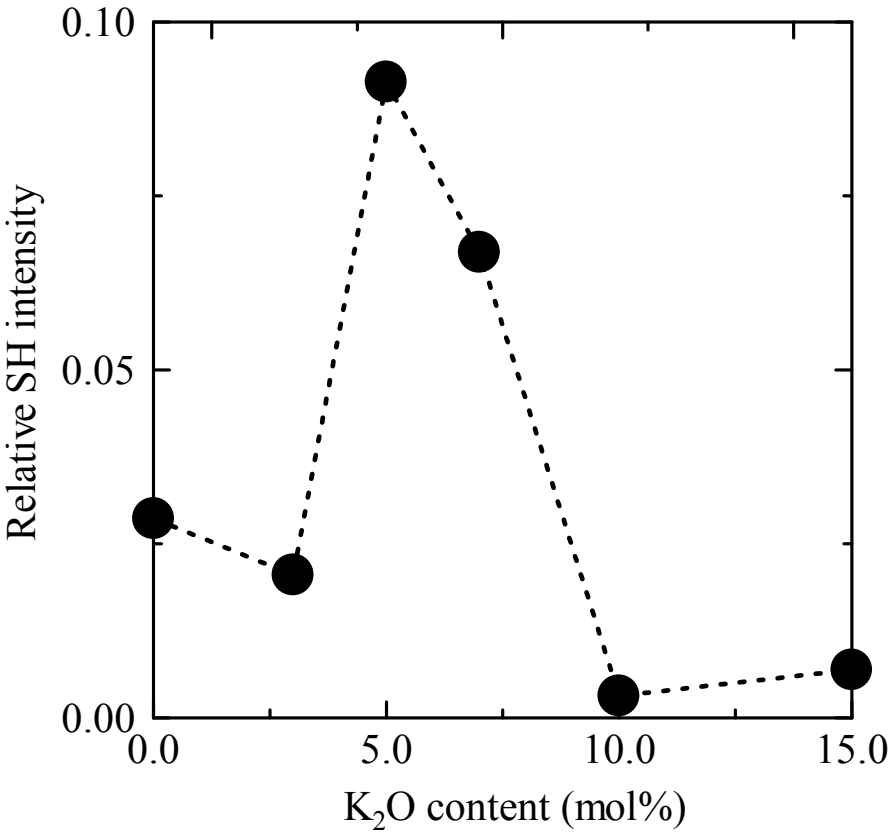

Figure 2.10 K_2O content dependence of SH intensity for the optically poled K_2O-Nb_2O_5-TeO_2 glasses. These values were monitored 30 s after ceasing the seed SH wave.

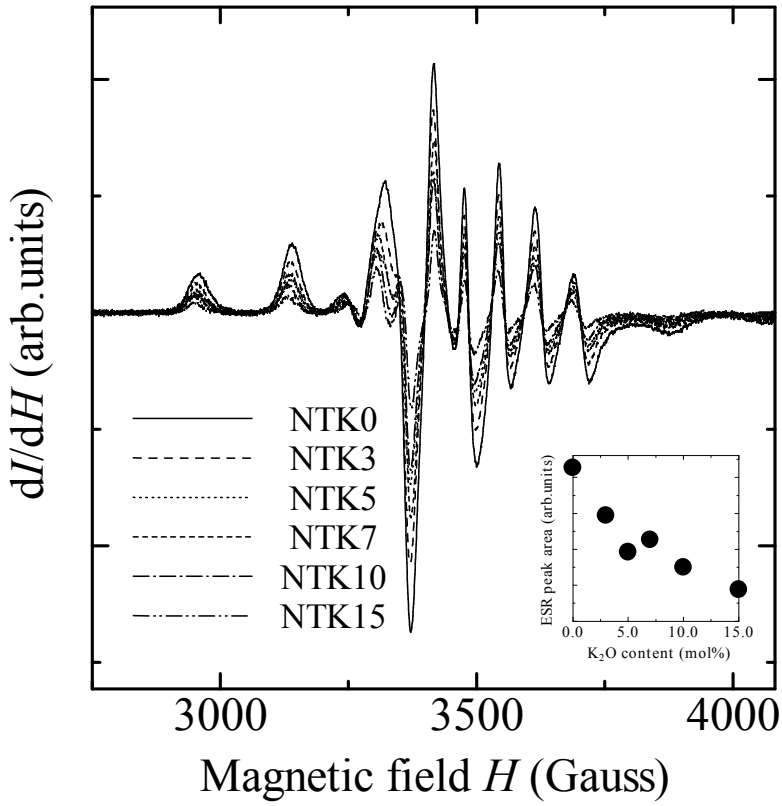

Figure 2.11 ESR spectra for VO^{2+} ion in K_2O-Nb_2O_5-TeO_2 glass doped with 0.5 mol% V_2O_5. The inset shows ESR peak area derived from the spectra plotted against K_2O content.

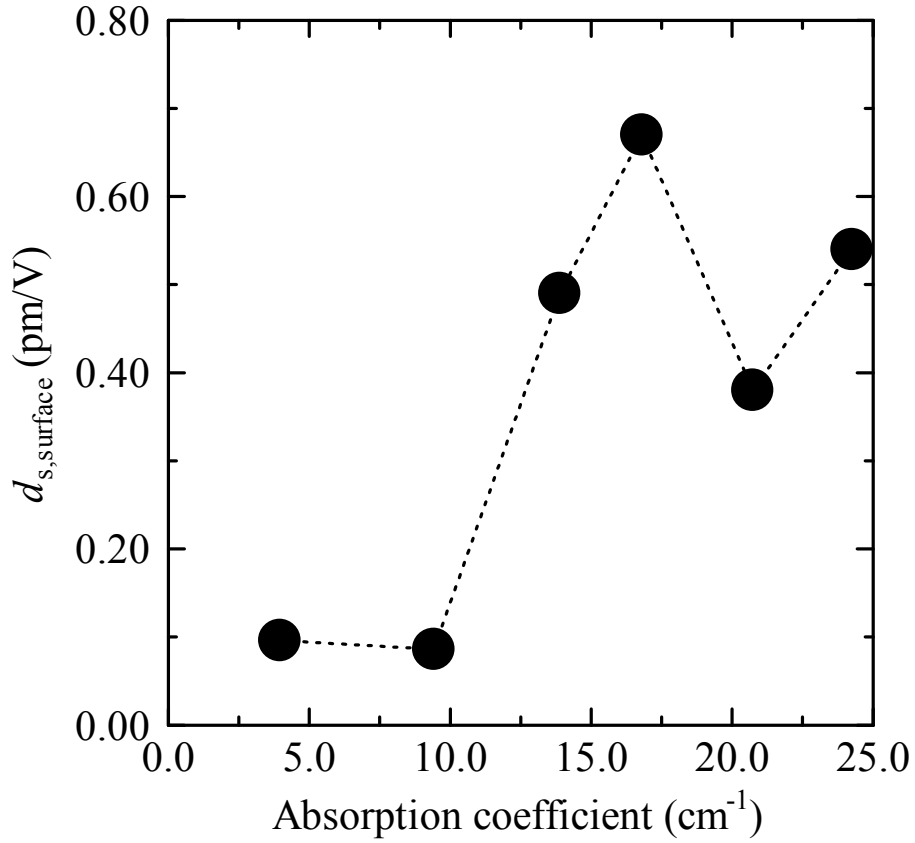

Figure 2.12 Optically encoded d-value at the incident surface vs. absorption coefficient at 532 nm for K_2O-Nb_2O_5-TeO_2 glass.

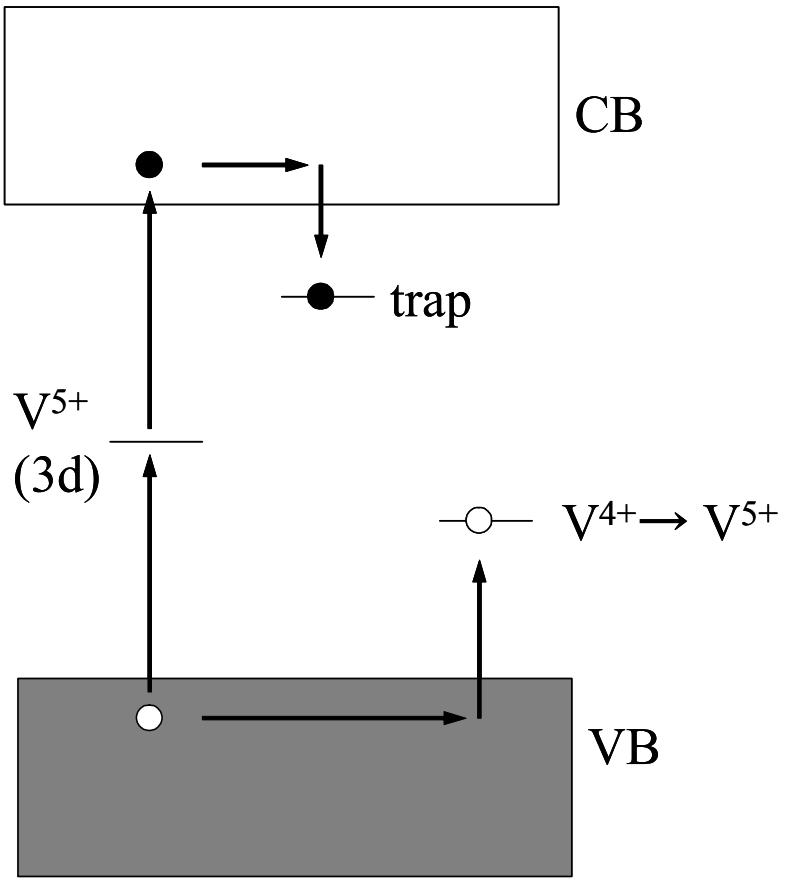

Figure 2.13 A schematic illustration of the generation mechanism of charged species, leading to the construction of polarized structure.

2.2 Tb-ion enhancement of optically encoded second-order nonlinearity in V_2O_5-doped $15Nb_2O_5 \cdot 85TeO_2$ glass

Introduction

This dissertation focuses on oxide glass as a candidate for second-order nonlinear optical media because they are easily prepared and have chemical and mechanical stability. However, the isotropic structure forbids second-order nonlinear optical effects. Therefore, the isotropic structure should be broken for $\chi^{(2)}$-induction. In section 2.1, to obtain a large second-harmonic (SH) output, pseudo-phase-matching structure was designed for Nb_2O_5-TeO_2 and K_2O-Nb_2O_5-TeO_2 glasses by optical poling. As a result, a large d-value, as much as 1.5 pm/V, was accomplished. Additionally, the obtained SH intensity was two-orders larger than that for thermally/electrically poled one. Some spectroscopic observation clarifies that the optical-poling $\chi^{(2)}$-induction is composed of two stages, i) the seeding 2ω beam used for optical poling creates positive holes and electrons through two-step photon absorption, and ii) the resultant charged species are oriented along with the internal DC field constructed by optical rectification among two ω photons and one 2ω photon. The resultant polarized structure serves an effective $\chi^{(2)}$. In the induction process, vanadium ion is necessary. Meanwhile, the vanadium-related optical absorption brings about some disadvantages as shown in Fig. 2.14. Because optical poling is performed via interference between ω and 2ω beams [1], when a target material does not have sufficient transmittance at these wavelengths, optically poled region is restricted, which limits the nonlinearly interacting length. Furthermore, SH wave generated in the optically poled medium is re-absorbed if optical absorbance is large at 2ω wavelength. In optically encoded $\chi^{(2)}$, there is another deficient point that it decays within 2-3 min. It is considered that the decay comes from the recombination of trapped positive hole and electrons. Hence, the optical absorption should be suppressed as much as possible in spite of its indispensability. In this part, an additional doping of rare-earth metal ions into vanadium-containing $15Nb_2O_5 \cdot 85TeO_2$ glass is attempted for increasing the active center without decreasing the transparency. Some of rare-earth ions take multivalent states. Such ions are expected to

play a role of a carrier trap center by changing its valence state. If trap sites exist around destination of released charge carrier, the carriers become stable at the trapped site. It is known that terbium ion takes either trivalent or tetravalent state. The tetravalent terbium ion may efficiently act as an electron trap center. Moreover, doped terbium ions do not show optical absorption at the SH wavelength. These characteristics are helpful for obtaining efficient harmonic-signal output.

Experimental

· Sample preparation

Reagent-grade (99.9 %) TeO_2, Nb_2O_5, V_2O_5 and Tb_4O_7 were used as starting materials for glass preparation. The chemical compositions of the prepared samples were $15Nb_2O_5{\cdot}85TeO_2$ (mol%) doped with several concentrations of V_2O_5 and Tb_2O_3. Note that Tb^{3+} and Tb^{4+} coexist in the raw material of Tb_4O_7 and that V^{4+} and V^{5+} also coexisted in tellurite glass matrices. That is, these compositions were nominal ones. Mixed batches were melted in a platinum crucible at 850 ˚C for 90 min in air. The melts were poured onto a stainless steel plate and cooled to room temperature to obtain glass. After the resultant glass was annealed at approximately 400 ˚C in air, it was cut into plates and both surfaces of the plate were polished with sandpaper and CeO_2 powder to become 1.00 mm thick.

· Optical absorption spectra

An optical absorption spectrum was measured for the as-prepared samples at room temperature using a spectrophotometer (Hitachi 330) to investigate the influence of dopant ions on the absorbance at 2ω wavelength. The measured value was used for the evaluation of d-value.

· Optical poling and SHG measurement

The glass samples were optically poled using linearly polarized fundamental (at 1064 nm) and double-frequency (at 532 nm) beams of a Q-switched Nd-doped

yttrium-aluminum-garnet (Nd: YAG) pulsed laser (Spectra Physics, GCR-11) as seeding beams. The pulse width and repetition rate of the laser were 7 ns and 10 Hz, respectively. A schematic illustration of the setup is already shown in Fig. 2.2. The coaxially aligned seeding beams were focused with a one-side converging lens and normally incident into the sample with the focal point situated slightly over the exit surface of the sample for poling. The irradiation lasted for 10 min. The peak laser intensities were 3.6 GWcm^{-2} for ω wave and 5.4×10^2 MWcm^{-2} for 2ω wave.

SHG measurement was performed using the same setup. After the poling process, only the ω beam was incident into the poled sample for probing SHG. The generated SH intensity was detected by a photomultiplier connected to an oscilloscope. The maximum SH intensity of a Y-cut α-quartz plate 1.046 mm thick was also measured as a standard under the same conditions in order to evaluate second-order nonlinearity using Eq. 2.5.

Results

· Optical absorption spectra

The optical absorption spectra for the prepared samples are shown in Fig. 2.15. In V_2O_5-containing sample, absorption peak due to the charge-transfer transition in V^{5+}-O^{2-} bond extends to over 600 nm. Since the magnitude is considerably larger than the sample containing only terbium ions, the influence of the terbium ions is buried in that of the pentavalent vanadium ions. Therefore, the whole shape of the spectrum is mainly dominated by the amount of vanadium ion.

· Time decay in SH intensity

Each glass sample exhibited observable SHG after optical poling. Figure 2.16 shows the time variations in SH intensity for a part of optically poled samples. The dotted line, thin solid line and thick solid line correspond to the data obtained from 0.05 mol% Tb_2O_3-containing glass, 0.05 mol% V_2O_5-containing glass and the glass containing both dopants, respectively. SH intensity for the V, Tb-codoped sample is approximately 4-fold

that of the V-doped sample, while SH intenstiy of the Tb-doped sample is one-fifth of the V-doped one. Unfortunately, the observed SH intensity exponentially decreases with time.

Figure 2.17 shows the dopant-concentration dependence of SH intensity. These data were measured 30 s after ceasing the irradiation of the seeding 2ω wave. SH intensity decreases with increasing vanadium concentration. A comparison among the samples containing equal amount of V_2O_5 reveals that as the amount of terbium ion increases, SH intenstiy increases, reaches the maximum value and decreases to the level without terbium ion.

Discussion

The mechanism of the optical encoding of $\chi^{(2)}$ into V_2O_5-doped tellurite glass is as follows [2-7]; Optical rectification induced by a $\chi^{(3)}(0,\omega,\omega,-2\omega)$ process makes the spatially coherent polarized structure in response to the difference in phase velocities between ω and 2ω light. After blocking the seeding 2ω beam, the polarization is left. Since the periodicity of the polarized structure automatically satisfies a pseudo-phase-matching condition, intense SH output is available. For V_2O_5-doped tellurite glass, a positive hole is possibly trapped by V^{4+} ion. As shown in Fig. 2.16, optically poled V, Tb-codoped samples explicitly manifests SHG, whereas SH intensity from the sample doped only with terbium ions is noise level. Because the chemical compositions of the prepared glass matrices were identical with each other, the difference in SH intensity reflects the range and quantity of dopants. One of the differences between vanadium and terbium ions is photosensitivity for the seeding beams, particularly for the 2ω wave (Fig. 2.15). The transparency of the vanadium-free samples leads to less intermediate energy levels through which electrons in the valence band are excited to the conduction band. It hinders the subsequent generation of charged species and the construction of polarized structure. Meanwhile, in the presence of vanadium ions, the terbium ions make a significant contribution to the output SH intensity in spite of its insensitivity to the seeding beams. This fact implies that terbium ion functions not as a source of charge carriers but as a trap center for them. Rare-earth elements are

predominantly present as trivalent state in glass, but some of them can take other valence states because of their electron configurations. Terbium ion has one electron in addition to the half-filled 4f shell in trivalent state, and can have a stable half-filled 4f shell configuration by releasing one 4f electron (i.e., tetravalent state). Such multiple stability is appropriate for a carrier trap site. Considering that the optical absorption peaks corresponding to V^{4+} ions are screened by the V^{5+}-dericed absorption, most vanadium ions seems to take pentavalent state. Therefore, the number of positive hole-trap site is not so large in V-doped tellurite glasses. The incorporation of terbium ions increases the hole-trap center because Tb^{3+} ion can trap a positive hole by changing its valence state. Moreover, Tb^{4+} ion possibly plays a role of electron-trap center, although their number is not so large. The increase of trap centers results in the enhancement of optically encoded $\chi^{(2)}$.

Figure 2.17 represents that SH intensity decreases monotonically with the increase in V_2O_5 amount due to the intense optical absorbance. Also, the comparison among the samples containing equal amount of vanadium ion shows that SH intensity increases initially with an increase of terbium ion. However, when the concentration exceeds 0.5 mol%, SH intensity decreases to the level when terbium ions are not doped. The maximum SH intensity is achieved for the sample containing 0.3 mol% V_2O_5 and 0.3 mol% Tb_2O_3. The reason excess terbium ions reduces SH intensity is unclear at this moment.

The decay in SH intensity for the V, Tb-doped sample means the instability of the induced DC field E_{dc} (Fig. 2.16). Although there seems to be many factors leading to the instability, two possible origins are suggested here. One is the recombination of charge carriers. The charge carriers at the trap sites are released by thermal or optical activation, and recombined with each other. The magnitude of the induced E_{dc} is then decreased. This instability is associated with the ligand field around the transition metal ions. According to the $\chi^{(2)}$-induction mechanism suggested above, the V^{4+} ion traps a positive hole and is converted to V^{5+} ion. It is thought that the ligand field around the resultant V^{5+} differs significantly from that of the V^{5+} ion originally present in the glass matrix. The latter V^{5+} ion is fully stabilized by the ligand field constructed during the glass forming process. On the other hand, the V^{5+} ion formed by accepting a positive hole is more unstable. Hence,

such a V^{5+} site can readily release the positive hole, resulting in the reduction of E_{dc}. Another possibility for the decay in SH intensity is the breakdown of the pseudo-phase-matching condition due to thermal shrinkage. A part of absorbed light energy is accumulated as heat, which causes local thermal expansion during optical poling. Because the pseudo-phase-matching condition is satisfied for the expanded medium, after seeding 2ω light is turned off, the periodicity of the matching condition shortens with decreasing the local temperature. The shrinkage yields insufficient phase-matching of generated SH wave and decreases output SH intensity. Unfortunately, tellurite glass is known as a medium with a high thermal expansion coefficient. The contribution of the thermal expansion is not negligible.

Conclusion

V, Tb-codoped $15Nb_2O_5 \cdot 85TeO_2$ glass becomes SHG-active by optical poling using the fundamental and the SH beam of a Nd:YAG laser. Observed SH intensity exceeds that for the glass containing only equal amount of vanadium ion. The Tb-enhancement mainly comes from the amplification in encoded d-value and reduced optical absorption. Meanwhile, there is an optimum concentration ratio for both dopants. The present study clarifies that terbium ion potentially increases the optically encoded $\chi^{(2)}$, although the decay in SH intensity cannot be suppressed.

References in Section 2.2

[1] K. Tanaka, K. Kashima, K. Hirao, N. Soga, A. Mito and H. Nasu, Jpn. J. Appl. Phys., 34 (1995) p. 173.

[2] R. H. Stolen and H. W. K. Tom, Opt. Lett., 12 (1987) p. 585.

[3] D. Z. Anderson, V. Mizrahi and J. E. Sipe, Opt. Lett., 16 (1991) p. 796.

[4] D. M. Krol and J. R. Simpson, Opt. Lett., 16 (1991) p. 1650.

[5] Y. Nageno, J. H. Kyung and N. M. Lawandy, Opt. Lett., 20 (1995) p. 2180.

[6] J. Si, K. Kitaoka, J. Qiu, T. Mitsuyu and K. Hirao, Opt. Lett., 24 (1999) p. 911.

[7] J. Si, Y. Kondo, J. Qiu, K. Kitaoka, N. Sugimoto, T. Mitsuyu and K. Hirao, Opt. Connum., 180 (2000) p. 179.

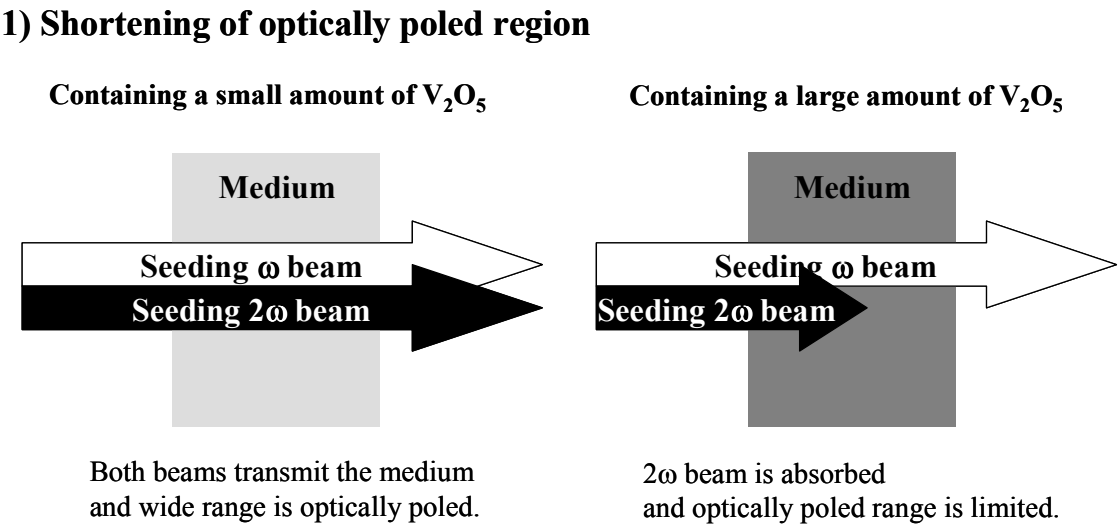

Figure 2.14 1) Schematic illustration of the disadvantages in $\chi^{(2)}$ induction and $P^{(2)}$-interaction caused by intense absorption. Intense absorption in visible range interrupts the penetration of seeding 2ω beam, which limits the optically poled region.

2) Reabsorption of generated SH wave

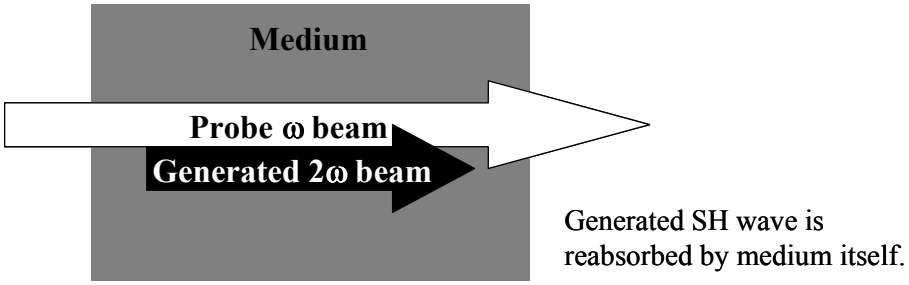

Figure 2.14 2) Schematic illustration of the disadvantages in $\chi^{(2)}$ induction and $P^{(2)}$-interaction caused by intense absorption. Intense absorption in visible range reduces output SH intensity due to reabsorption of generated SH wave.

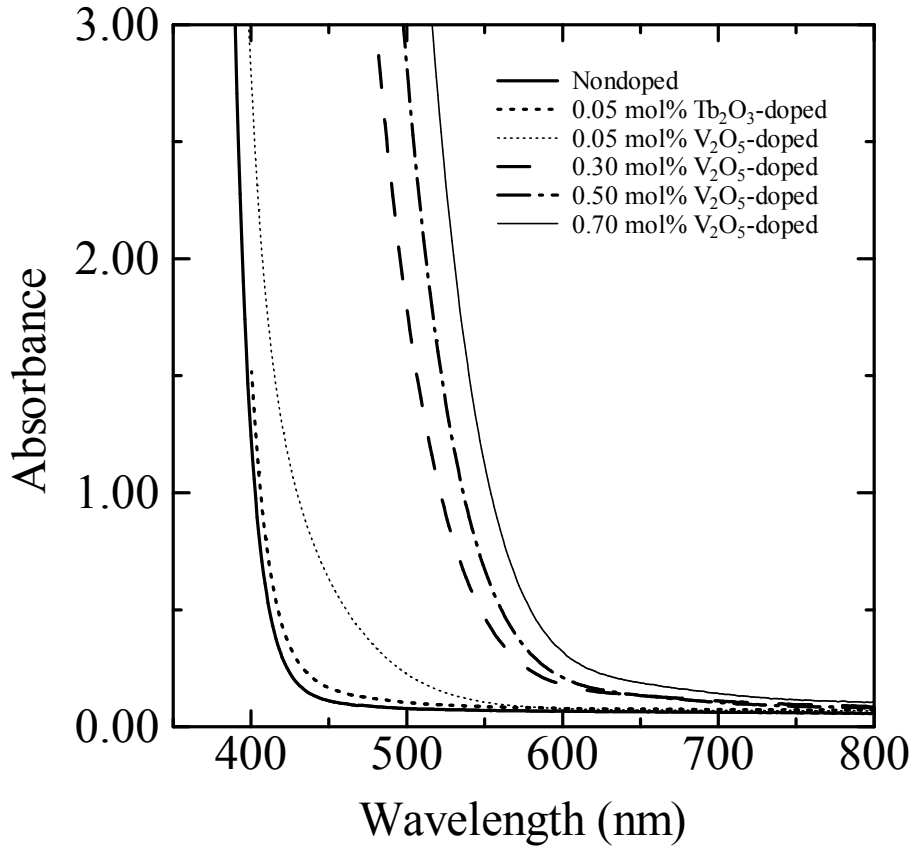

Figure 2.15 Optical absorption spectra for $15Nb_2O_5 \cdot 85TeO_2$ (mol%) glasses doped with V_2O_5 or Tb_2O_3. Because the absorbance is largely dominated by vanadium ions, the absorption peaks caused by terbium ion are barely observed.

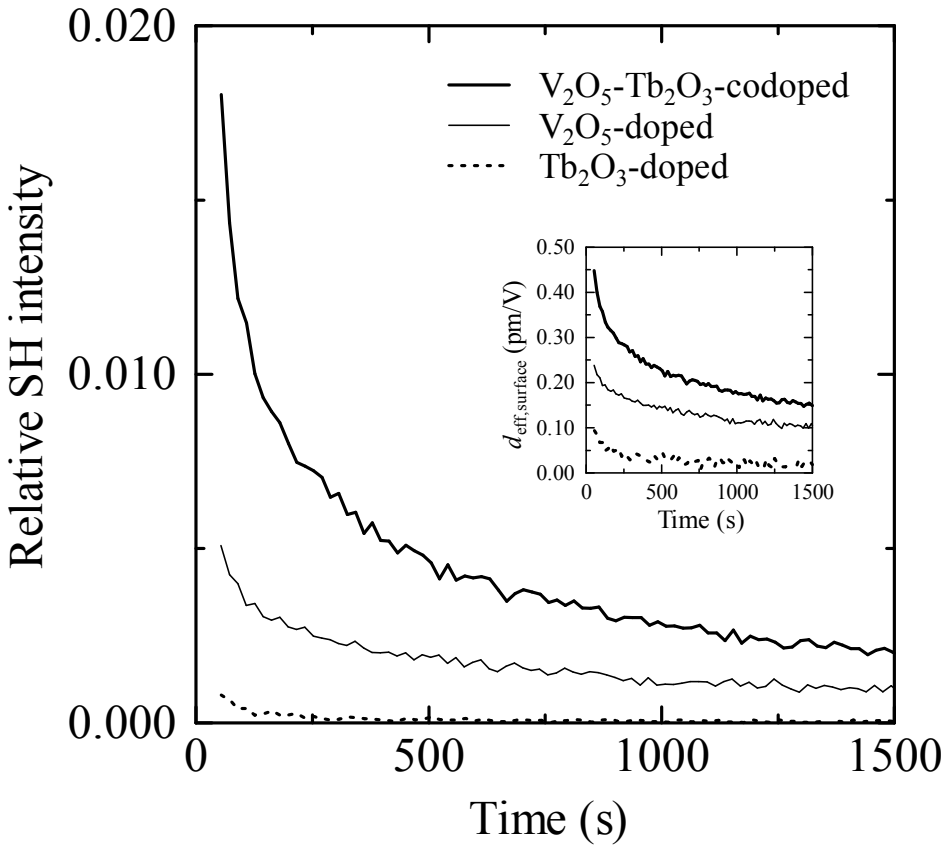

Figure 2.16 Time variation in SH intensity for the optically poled $15Nb_2O_5 \cdot 85TeO_2$ (mol%) glasses containing only 0.05 mol%-V_2O_5 (thin solid curve), only 0.05 mol%-Tb_2O_3 (broken curve) and both of them (thick solid curve). The inset shows the transition in effective d-value.

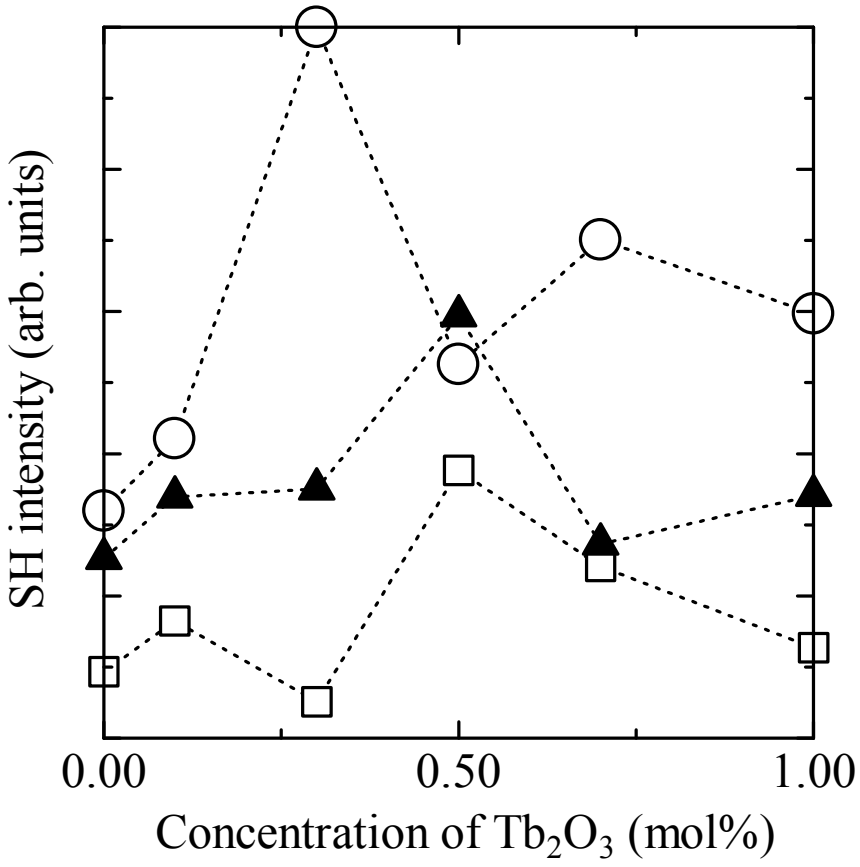

Figure 2.17 SH intensity for the optically poled V, Tb-codoped $15Nb_2O_5 \cdot 85TeO_2$ glass samples. They were monitored 30 s after blocking the seeding 2ω wave. Open circle, closed triangle and open square denote 0.30, 0.50 and 0.70 mol% V_2O_5-doped sample, respectively.

Chapter 3 Space-selective precipitation of nonlinear optical crystals by near-infrared femtosecond laser irradiation

Introduction

Laser-induced crystallization or permanent refractive-index changes in a transparent medium have attracted much attention because the space-selective functionalization is applicable to the fabrication of optical waveguides, photonic crystal, Bragg gratings, and so forth [1-18]. Sato et al. [12] have made dot patterns composed of polycrystalline $Sm_2Te_6O_{15}$ on a BaO-Sm_2O_3-TeO_2 glass using a fundamental wave of a cw neodymium-doped yttrium-aluminum-garnet (Nd:YAG) laser. They proposed that the absorption due to 4f-4f transition of Sm^{3+} ions and the subsequent nonradiative relaxation induced local heating responsible for the crystallization. A similar phenomenon was observed in Sm_2O_3-Bi_2O_3-B_2O_3 glasses [13,15]. Macienta et al. [14] have succeeded in forming highly oriented lines made of single-domain β-BaB_2O_4 on the surface of a BaO-B_2O_3-TiO_2 glass using a CO_2 laser. In each case, laser-derived heat supply accelerated the structural modification. However, the crystallization was localized on the surface because the heat supply was accomplished via linear absorption of the irradiated medium. Recently, Miura et al. reported space-selective growth of second-order nonlinear optical crystal (β-BaB_2O_4) *inside* a BaO-Al_2O_3-B_2O_3 glass using near-infrared femtosecond-laser pulses [8]. When the femtosecond-laser beam is tightly focused, the power density at the focal point is high enough to bring about nonlinear absorption leading to high-density electron plasma generation. Subsequently, structural modification including crystallization occurred by excess energy release from the plasma into the surrounding glass network [16]. Since the plasma generation is localized at the laser-focal region, the crystallization process is superior in terms of the internal modification of a transparent material compared with the case utilizing linear absorption or heat treatment. In this chapter, the formation of frequency-conversion crystal, such as $LiNbO_3$ and $BaTiO_3$, inside some silicate glasses is demonstrated using a tightly-focused near-infrared femtosecond-pulsed laser. To clarify the crystallization mechanism, elemental analysis at the laser-focal area is performed by means of electron probe

microanalysis (EPMA). The analysis reveals that the radial migration of glass-constituting cations facilitates the precipitation of nonlinear optical crystal.

Experimental

· Glass preparation

The chemical compositions of the prepared glasses are listed in Table 3.1. The glass samples were prepared from reagent-grade SiO_2, B_2O_3, TiO_2, Nb_2O_5, Al_2O_3, $BaCO_3$, Na_2CO_3 and Li_2CO_3. The purity was 99.9 %. The raw materials were mixed thoroughly and melted in a platinum crucible at 1400-1550 °C for 1 h in air. The melt was poured onto a stainless plate and quenched with another stainless plate to obtain a bulk glass. In order to check the thermal stability against crystallization, glass transition temperature T_g and crystallization onset temperature T_c were determined by differential thermal analysis (DTA) at the heating rate of 10 K/min. The obtained values are summarized in Table 3.2. The resultant glass was annealed at around T_g for 2 h and cut into a rectangular parallelepiped with a thickness of about 2 mm. All the surfaces of the glass thus obtained were polished with sandpaper and CeO_2 powder to get mirror surfaces.

Table 3.1 Chemical compositions of glasses prepared in the present study (mol %).

Sample	Li_2O	Na_2O	BaO	Al_2O_3	Nb_2O_5	TiO_2	SiO_2	B_2O_3
1	32.5				27.5		40.0	
2	30.0				10.0		60.0	
3			32.5			32.5	35.0	
4		5.0	36.0			39.0	20.0	
5 [a]			47.5	5.0				47.5

[a] The composition of sample 5 is the same as that reported in Ref. [8].

· Femtosecond-laser irradiation and characterization

As a light source, regeneratively-amplified pulses from a mode-locked Ti:sapphire laser (wavelength 800 nm, repetition rate 200 kHz, pulse duration ~120 fs, average power ~600 mW) were used. A glass sample was placed on the stage of an optical microscope. The near-infrared laser beam reflected by a dichroic mirror inside the microscope was focused at ~500 μm below the surface of the sample through a 50× microscope objective lens with the numerical aperture of 0.5. The focused laser beam had the waist of ~2 μm in diameter. For making it easier to characterize the laser-modified structure, a laser irradiation point was repeatedly swept at regular intervals to produce a plane composed of laser-modified line patterns 2.5 mm long. The irradiated sample was polished to the depth of the beam waist so that the modified region coming on a surface.

· X-ray diffraction analysis

To identify crystalline phases if precipitated, X-ray diffraction (XRD) measurements were performed for the polished samples with CuKα radiation at room temperature. The identification is performed by comparing the obtained pattern and JCPDS cards.

Table 3.2 Glass transition temperature T_g and onset temperature of crystallization T_c determined by DTA[a]. Laser-irradiation time required for crystallization is also shown.

Sample	T_g (ºC)	T_c (ºC)	Time required for crystallization
1	560	700	2-3 min.
2	533	754	10 min.
3	741	849	1-2 min.
4	593	660	immediately after the laser irradiation
5	520	613	30 min.

[a] The heating rate in DTA was 10 K·min^{-1}

· Elemental analysis

In order to investigate the change in chemical composition caused by the laser irradiation, scanning electron microscope (SEM) observation and electron probe microanalysis (EPMA) were carried out for a laser-induced dot pattern.

Results

Li_2O-Nb_2O_5-SiO_2 glass

Samples 1 and 2 exhibited a laser-induced refractive-index change immediately after the femtosecond-laser irradiation. Figure 3.2 depicts typical optical-microscope images for the laser-irradiated samples (sample 1); the top- and side-views at around the focal region, respectively. The cross section perpendicular to the beam propagation direction has a circular shape due to refractive-index change, which reflects a Gaussian intensity profile of the incident beam, while the modified region looks elongated in the laser propagation direction. The anisotropy is due to the filamentation which comes from a dynamic balance between two competitive nonlinear processes: self-focusing induced by an optical Kerr effect and defocusing mainly caused by plasma formation [19]. After 120 s irradiation, intense blue light suddenly appeared from the vicinity of the focal spot as shown in Fig. 3.3. XRD analysis of the emitted area confirms the precipitation of $LiNbO_3$ which is famous for the large d_{33}-value (Fig. 3.4(a)). The spectrum of the blue emission, measured by introducing it into an optical fiber connected with a spectrometer, is shown in Fig. 3.3(b). The emission has a sharp peak at the wavelength of 400 nm which is just half the wavelength of the incident beam (800 nm). Therefore, the blue light is considered to be second-harmonic wave from the precipitated $LiNbO_3$. Hereafter, the irradiation time required for crystallization is defined as the period from the start of the laser irradiation until the appearance of the blue light. As seen in Table 3.2, $30.0Li_2O{\cdot}10.0Nb_2O_5{\cdot}60.0SiO_2$ glass (sample 2) requires more time to crystallize than sample 1.

Figure 3.5(a) depicts a SEM image around a laser-focal region in $32.5Li_2O{\cdot}27.5Nb_2O_5{\cdot}40.0SiO_2$ glass (sample 1). The elemental analysis was performed

along the white dotted line in the SEM photograph. The spatial distributions of Si and Nb elements are shown in Fig. 3.5(b). One can see that the concentration of silicon is higher in the center of the irradiated area than the outside. In contrast, Nb element migrates outside, which brings about a decrease in Nb element at the center.

Na_2O-BaO-TiO_2-SiO_2 glass

Laser-induced precipitation of nonlinear optical crystals was also observed in samples 3 and 4. Required irradiation time for crystallization is drastically decreased from a few minutes to 1 s or so by adding Na_2O in glass matrix (Table 3.2). In sample 4, the laser irradiation precipitates $BaTiO_3$ and $Ba_2TiSi_2O_8$ (Fig. 3.4(b)) those are known as ferroelectric compounds at room temperature. Although $BaTiO_3$ is reported to be sometimes present as cubic phase at room temperature within the glass-ceramics where T_g exceeds the Curie temperature, it seems that the $BaTiO_3$ observed in this experiment has tetragonal structure because they are under a high pressure condition caused by sonic wave propagation. As for $Ba_2TiSi_2O_8$, Takahashi et al. reported SHG from a transparent surface-crystallized glass containing the phase [20]. Therefore, this crystal was also responsible for the blue emission.

BaO-Al_2O_3-B_2O_3 glass

Laser-induced precipitation followed by SHG was also observed for the $47.5BaO{\cdot}5.0Al_2O_3{\cdot}47.5B_2O_3$ glass (sample 5). This result was consistent with that of Miura et al. [8] The SHG came from laser-precipitated β-barium borate (β-BaB_2O_4, β-BBO). The laser-irradiation time required for the crystallization was 30 min.

Figures 3.6(a) and (b) show the spatial distributions of constituent cations immediately after the laser irradiation and after 30 min irradiation, respectively. Short-time irradiation exhibits nothing more than the migration of Al species from outside to inside. The irradiation for 30 min results in the β-BBO precipitation. At that time, the spatial contrasts of constituting cations become clearer. The gradient of the Ba concentration is less prominent.

Discussion

As seen in Fig. 3.2, femtosecond laser irradiation influences an area (~20 μm in diameter) larger than the beam waist of tightly-focused laser (~2 μm in diameter). In addition, there is a tendency that the irradiation time required for crystallization is shorter as the temperature difference $T_c - T_g$, a measure of thermal stability of glass, decreases (Table 3.2). These results imply that the laser-induced structural change involves a thermal diffusion process. In order to check the thermal effect, samples 1 and 4 were subjected to heat treatment at the crystallization temperature. Figures 3.7(a) and 3.7(b) correspond to the XRD patterns of heat-treated samples 1 and 4, respectively. The crystalline phases appeared after the heat treatment are coincident with those after the long-time femtosecond-laser irradiation, which represent a thermal contribution during the laser irradiation, indirectly. Meanwhile, the elemental analysis at the laser-focal region reveals that the laser irradiation makes elemental migration as well as the thermal effect. In Fig. 3.6, the elemental migration is observed even just after the irradiation. Similar behavior was reported for tellurite glasses exposed to a femtosecond laser pulses [16]. The migration affects the crystallization and the morphology of induced structure. In the sample 1, it is necessary for $LiNbO_3$ precipitataion that Nb species gather at a region since the Nb/Li ratio of the original glass is much smaller than that in stoichiometric $LiNbO_3$. The elemental profile shown in Fig. 3.5(b) shows the increase in Nb species at the surrounding region in response to the decrease at the center. From the profile, it is reasonable to consider that polycrystalline $LiNbO_3$ appeared with a ring shape. The ring-shaped precipitation area was also expected for the β-BBO appeared in the sample 5 because the concentration of Al species which do not participate in β-BBO formation increases at the central part of the focal area. From the discussion, it is concluded that the laser-induced structural modification or crystallization is driven by local heating (thermal gradation) and elemental migration (chemical gradation). Why the multiple effects are induced by femtosecond-laser pulses is explained from the viewpoint of microexplosion [4,16]. According to Mazur et al., the microexplosion is explained as follows: Tightly-focused femtosecond-laser pulses generate electrons at the focal volume where the laser intensity exceeds a threshold of multiphoton excitation (nonlinear absorption). After

being accelerated by subsequent laser pulses through an inverse bremsstrahlung process, the electrons collide with surrounding atoms to derive secondary electrons. As this process repeats, high-density plasma is created (electron avalanche). When the excess energy accumulated as plasma is explosively released to the surrounding glass network, local heating occurs. Simultaneously, the glass medium around the focal region expands rapidly because of the abrupt heating. Then, the impact propagates to the outside as shock waves or pressure waves. Considering the mechanism, temperature gradient should occur with the highest temperature region at the focal volume where plasma appeared (thermal gradient). According to Sakakura and Terazima [21], the refractive-index change induced by the femtosecond-laser pulses is attributed to the propagation of the pressure waves accompanied by microexplosion. Meanwhile, Sundaram et al. observed the elemental migration riding on the pressure waves triggered by the explosion (chemical gradient) [16]. It is thus presumable to conclude that the space-selective crystallization observed in this study was also related to the thermal and chemical gradation caused by microexplosion. From the discussion, the mechanism of the crystallization using a femtosecond laser is speculated as illustrated in Fig. 3.8. The combination of the thermal and chemical gradient associated with the shock-wave propagation is responsible for the laser-induced space-selective crystallization inside glasses. Since the inside of the ring-shaped region is poor in crystal-constituting species, the central part is thought to be an amorphous state. After a nucleation is stimulated by the thermal and chemical gradient, the seed crystals grow toward the inside. When the laser irradiation is stopped, the driven species are fixed because they do not have enough time or energy to redistribute or diffuse back. As a result, a ring pattern made of nonlinear optical crystals is obtained. Although in sample 4, the dominant crystalline phases are different between the laser-used case (Fig. 3.4(b)) and the heat-treated case (Fig. 3.7(b)), it is possibly due to the chemical gradient. The SHG observed in response to the precipitation might be related to the nonlinear optical crystal in frozen pressure waves. Even if a laser-induced spot have a circular pattern, the scanning of femtosecond laser beam allows the modified region to grow continuously into a crystalline tube, as Miura and coworkers reported earlier [8]. They also demonstrated the growth of single-domain crystal by adjusting the laser scanning speed.

It is conceivable that once crystal is precipitated in an irradiated spot, they work as seed, which is similar to a zone-melting method for single-crystal growth.

Conclusion

The precipitation of second-order nonlinear optical crystals inside some oxide glasses is successfully demonstrated using tightly focused femtosecond laser pulses. Femtosecond-laser pulses impose chemical gradient as well as thermal gradient, which results in ring-shaped modified structure. The laser-irradiation period necessary for crystallization is closely related to the thermal stability of original glass.

The femtosecond laser technique is applicable to three-dimensional microfabrication of transparent materials. The feasibility of single-crystalline-line forming inside a transparent glass medium offers us unique opportunity for producing all-optical circuits.

References in Chapter 3

[1] B. C. Stuart, M. D. Feit, A. M. Rubenchik, B. W. Shore, M. D. Perry, Phys. Rev. Lett., 74 (1995) p. 2248.

[2] K. M. Davis, K. Miura, N. Sugimoto, K. Hirao, Opt. Lett., 21 (1996) p. 1729.

[3] E. N. Glezer, M. Milosavljevic, L. Huang, R. J. Finlay, T.-H. Her, J. P. Callan, E. Mazur, Opt. Lett., 21 (1996) p. 2023.

[4] E. N. Glezer, E. Mazur, Appl. Phys. Lett., 71 (1997) p. 882.

[5] K. Miura, J. Qiu, H. Inouye, T. Mitsuyu, K. Hirao, Appl. Phys. Lett., 71 (1997) p. 3329.

[6] D. Homelle, S. Wielandy, A. L. Gaeta, N. F. Borrelli, C. Smith, Opt. Lett., 24 (1999) p. 1311.

[7] L. Sudrie, M. Franco, B. Prade, A. Mysyrewicz, Opt. Commun., 171 (1999) p. 279.

[8] K. Miura, J. Qiu, T. Mitsuyu, K. Hirao, Opt. Lett., 25 (2000) p. 408.

[9] A. M. Streltsov, N. F. Borrelli, Opt. Lett., 26 (2001) p. 42.

[10] C. B. Schaffer, A. Brodeur, J. F. Garcia, E. Mazur, Opt. Lett., 26 (2001) p. 93.

[11] J. W. Chan, T. R. Huser, S. Risbud, D. M. Krol, Opt. Lett., 26 (2001) p. 1726.

[12] R. Sato, Y. Benino, T. Fujiwara, T. Komatsu, J. Non-Cryst. Solids, 289 (2001) p. 228.

[13] T. Honma, Y. Benino, T. Fujiwara, R. Sato, T. Komatsu, Opt. Mater., 20 (2002) p. 27.

[14] A. F. Maciente, V. R. Mastelaro, A. L. Martinez, A. C. Hernandes, C. A. Carneiro, J. Non-Cryst. Solids, 306 (2002) p. 309.

[15] T. Honma, Y. Benino, T. Fujiwara, T. Komatsu, Appl. Phys. Lett., 82 (2003) p. 892.

[16] S. K. Sundaram, C. B. Schaffer, E. Mazur, Appl. Phys. A, 76 (2003) p. 379.

[17] H. Sun, S. Matsuo, H. Misawa, Appl. Phys. Lett., 74 (1998) p. 786.

[18] K. O. Hill, B. Malo, F. Bilodeau, D. C. Johnson, J. Albert, Appl. Phys. Lett., 62 (1993) p. 1035.

[19] L. Luo, D. Wang, C. Li, H. Jiang, H. Yang, Q. Gong, J. Opt. A, 4 (2002) p. 105.

[20] Y. Takahashi, Y. Benino, T. Fujiwara, T. Komatsu, J. Appl. Phys., 95 (2004) p. 3503.

[21] M. Sakakura, M. Terazima, Opt. Lett., 29 (2004) p. 1548.

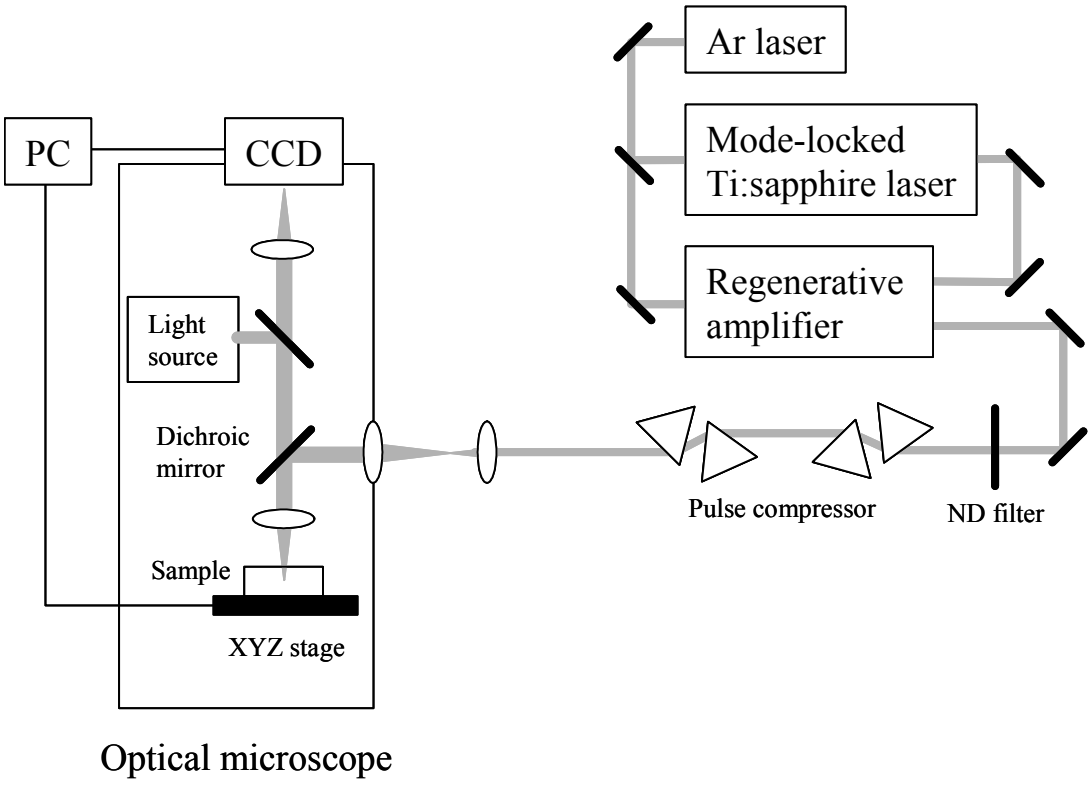

Figure 3.1 Schematic illustration of the setup for femtosecond-laser irradiation.

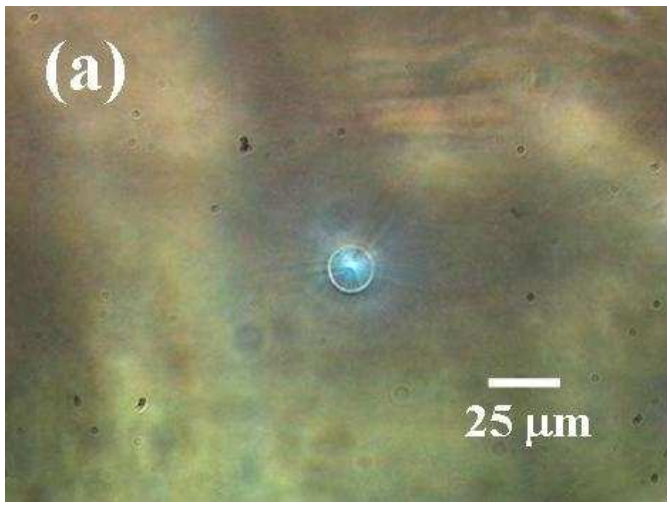

Figure 3.2 Optical-microscope photographs of the $32.5Li_2O{\cdot}27.5Nb_2O_5{\cdot}40.0SiO_2$ glass (sample 1) immediately after the femtosecond-laser irradiation [(a) : top view, (b): side view].

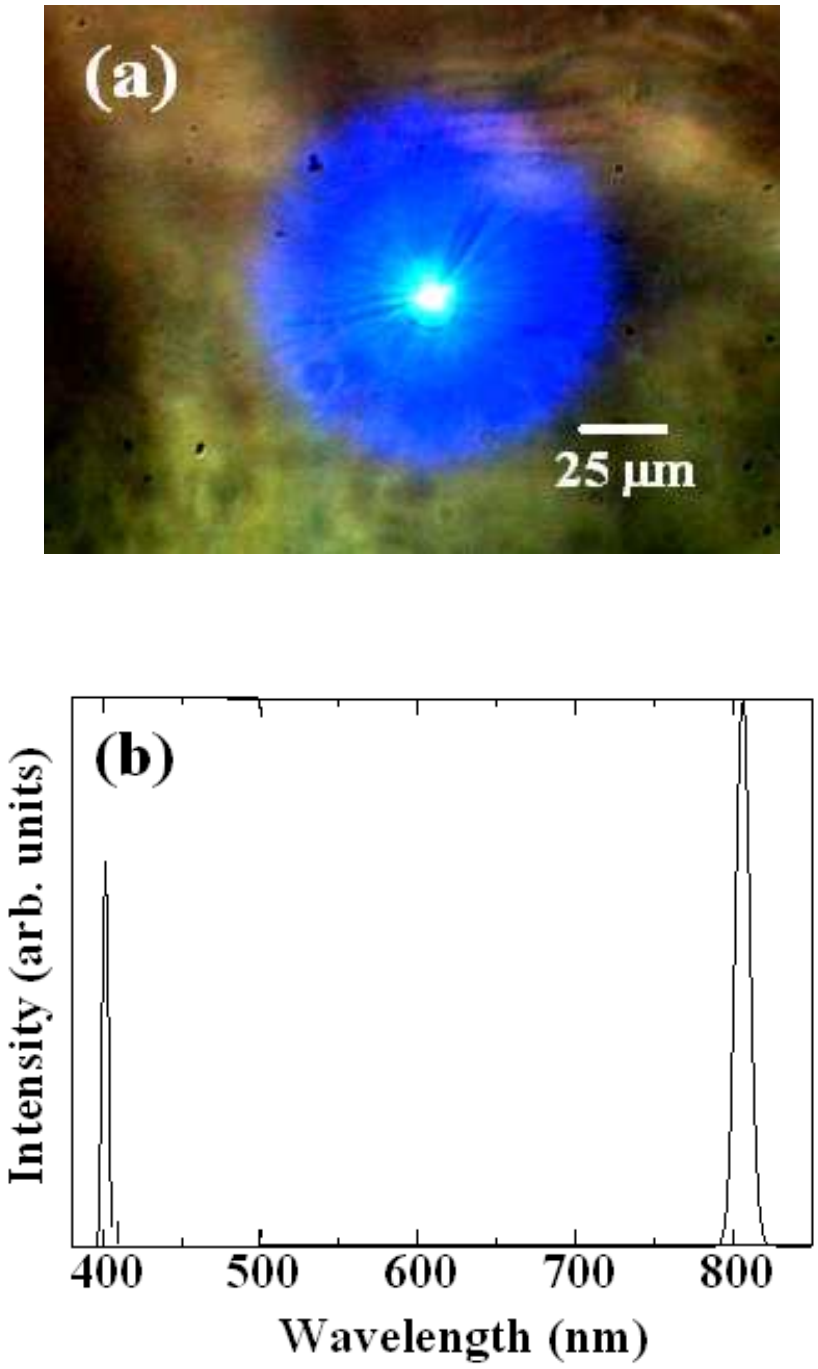

Figure 3.3 Optical-microscope photographs of blue emission in $32.5Li_2O{\cdot}27.5Nb_2O_5{\cdot}40.0SiO_2$ glass (sample 1) and the spectrum. The emission was observed 120 s after laser irradiation [top view]. The emission peak at 800 nm corresponds to the incidence.

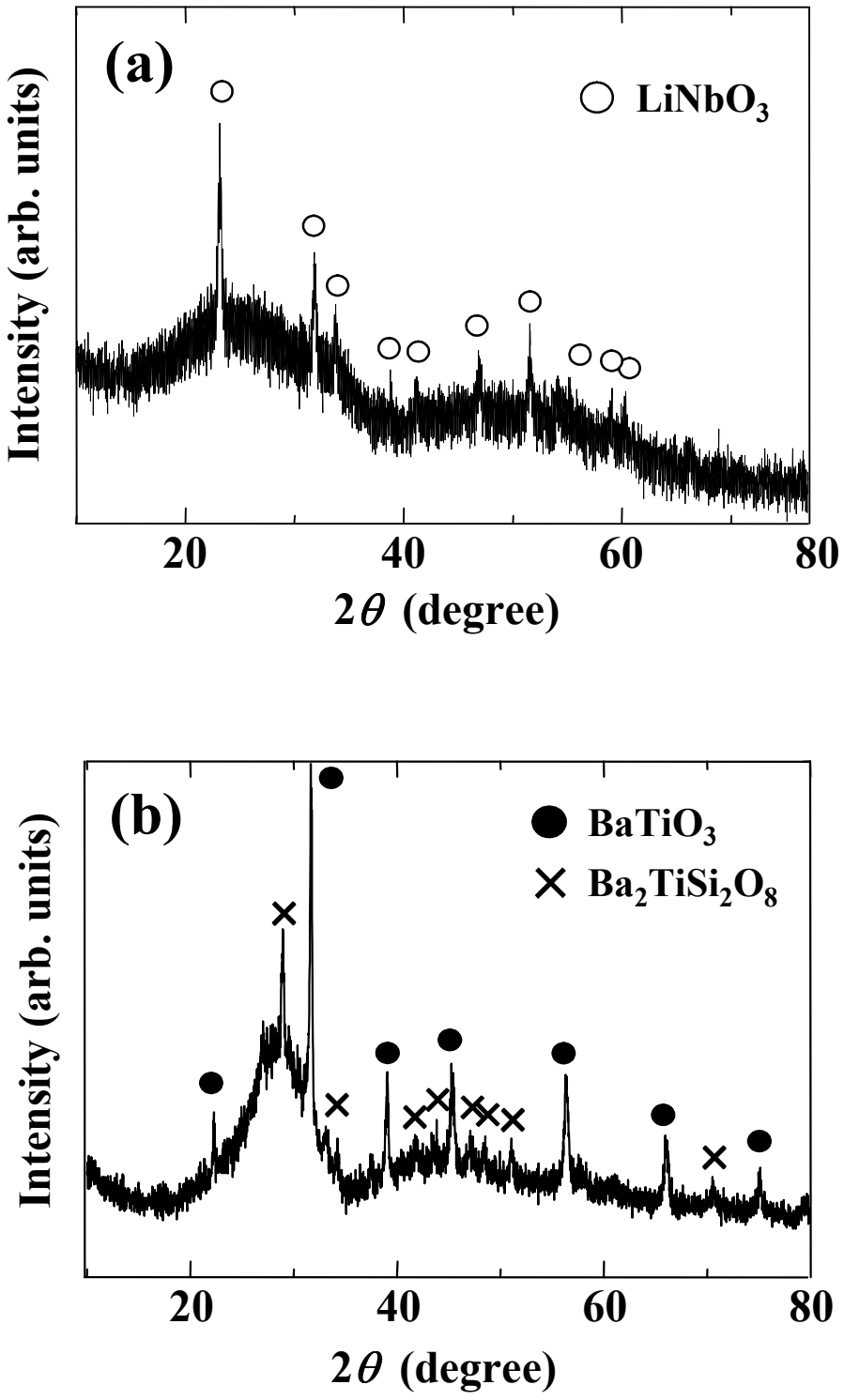

Figure 3.4 X-ray diffraction patterns for laser-induced precipitates (a) in $32.5Li_2O{\cdot}27.5Nb_2O_5{\cdot}40.0SiO_2$ glass (sample 1) and (b) in $5.0Na_2O{\cdot}36.0BaO{\cdot}39.0TiO_2{\cdot}20.0SiO_2$ glass (sample 4).

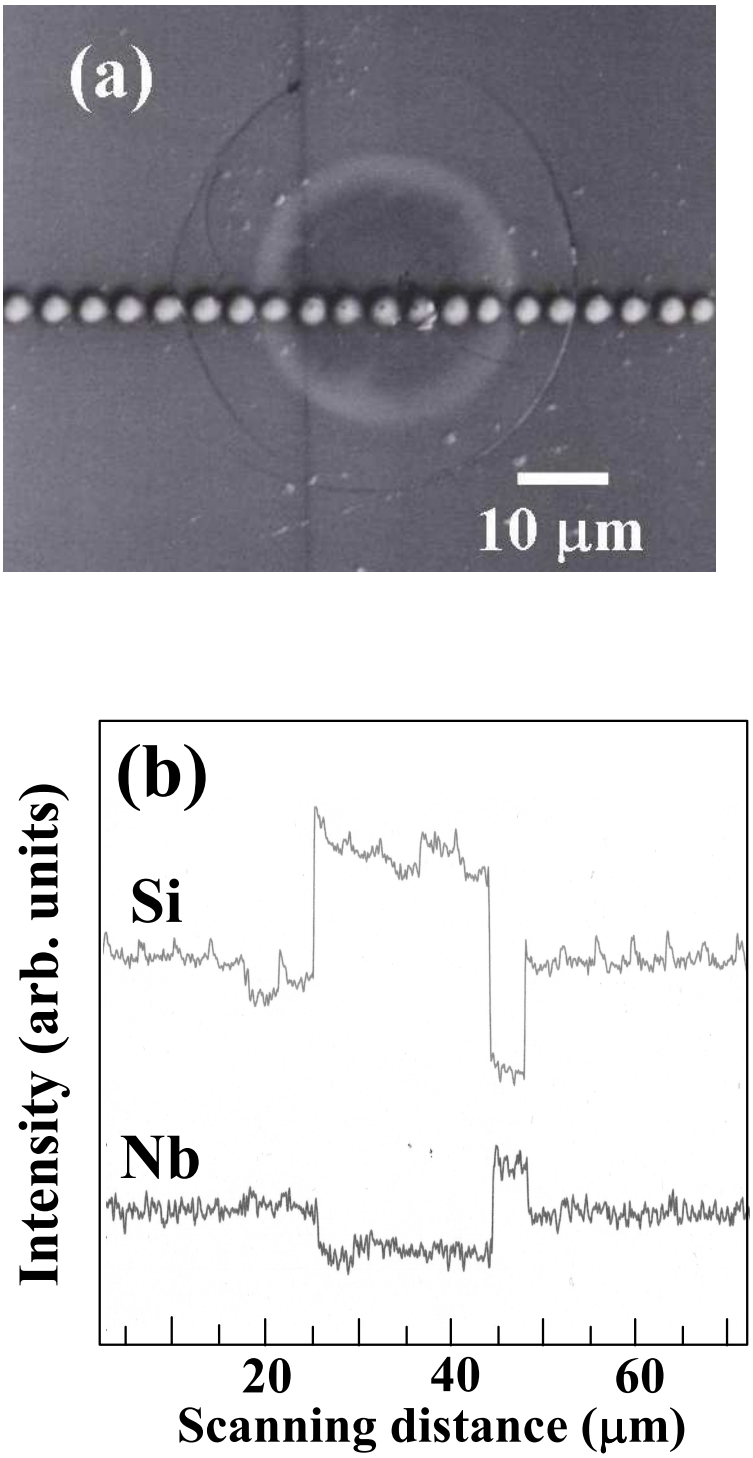

Figure 3.5 SEM photograph and the spatial profile of Si and Nb species around the laser focal point for $32.5Li_2O{\cdot}27.5Nb_2O_5{\cdot}40.0SiO_2$ glass (sample 1). White dots show the regions probed by electron beam.

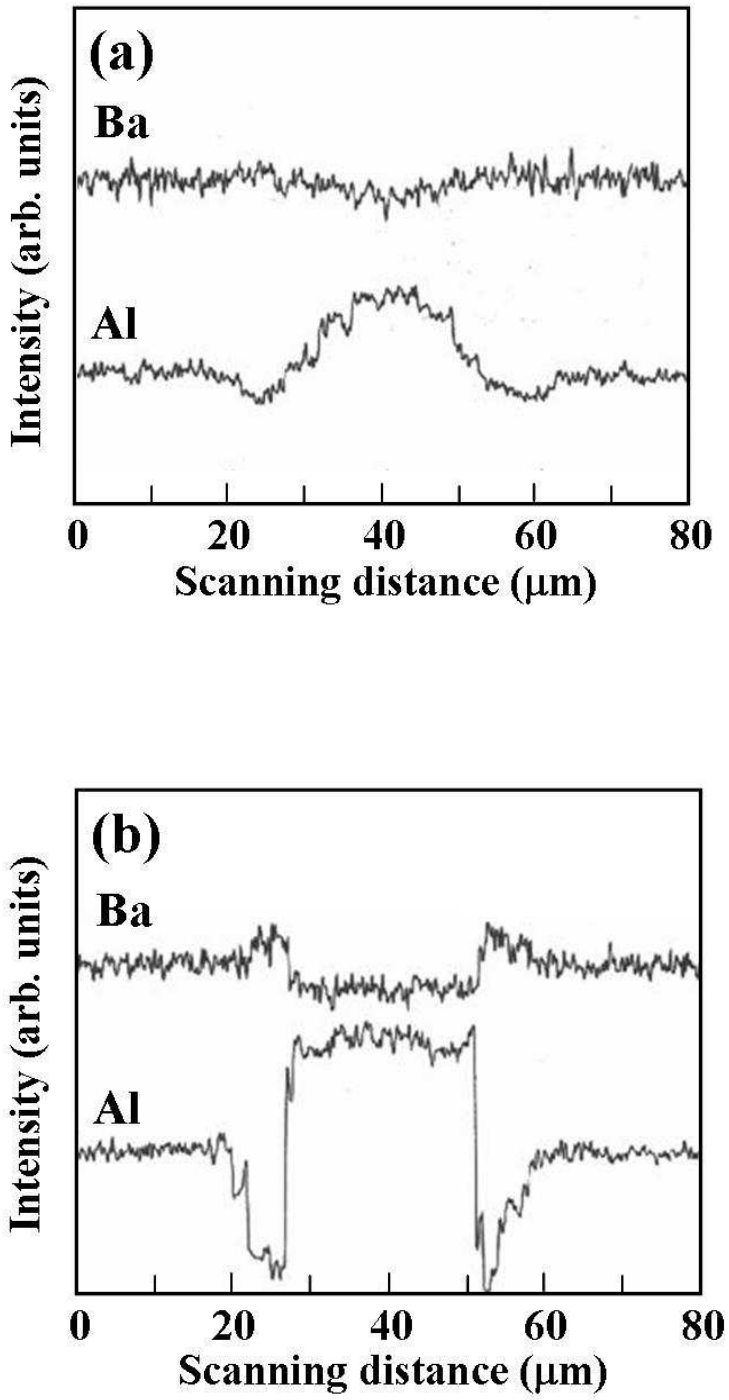

Figure 3.6 Spatial profile of Ba and Al species around the laser focal point for $47.5BaO{\cdot}5.0Al_2O_3{\cdot}47.5B_2O_3$ glass (sample 5): Figures (a) and (b) correspond to the data immediately after the laser irradiation and after the irradiation for 30 min or so, respectively.

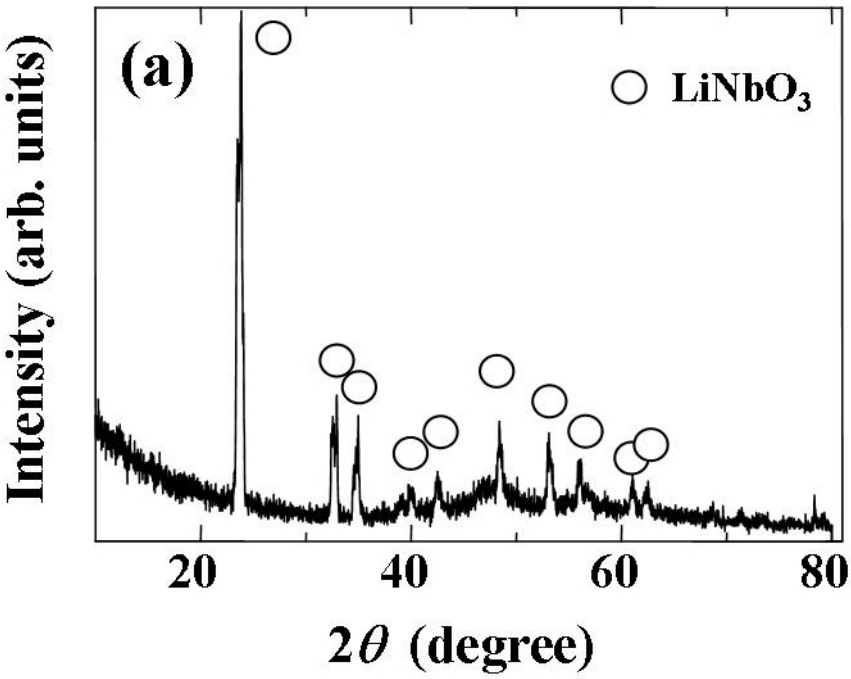

Figure 3.7(a) X-ray diffraction patterns for heat-treated $32.5Li_2O{\cdot}27.5Nb_2O_5{\cdot}40.0SiO_2$ glass (sample 1).

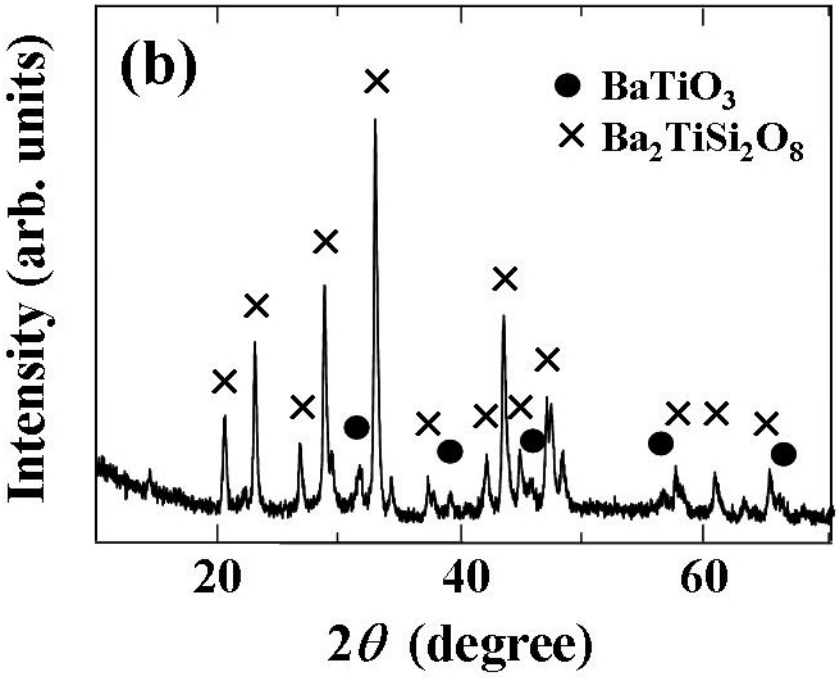

Figure 3.7(b) X-ray diffraction patterns for $5.0Na_2O{\cdot}36.0BaO{\cdot}39.0TiO_2{\cdot}20.0SiO_2$ glass (sample 4).

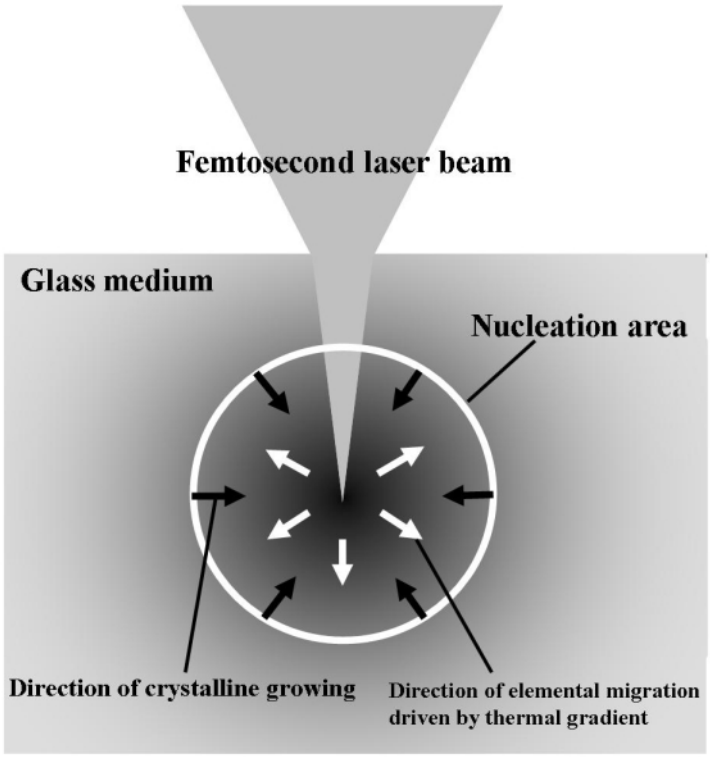

Figure 3.8 Schematic illustration of the space-selective crystallization induced by tightly-focused femtosecond laser pulses. Microexplosion induces a thermal gradient and radial migration of the constitutes to make the chemical gradient. The thermal gradient at the focal volume is represented by the gradation of color: thicker color corresponds to the higher temperature region. Nucleation takes place at a certain distance from the focusing point due to the thermal and chemical gradients. Because the inside of the nucleation area has higher temperature than the outside, the precipitated seed crystals grow toward the inside.

Summary

The present dissertation has presented important experimental results on the construction of polarized structure inside oxide glasses. A more detailed understanding on space-selective poling by an external stimulus such as electric field and laser interference field was developed. The induced polarized structure gives much amount of useful application for optical devices. The results of the respective chapter are summarized as follows.

In section 1.1, theoretical backgrounds on nonlinear optical phenomena and on the relevance to structure were explained in terms of classical electromagnetism. A general Maker-fringe equation, by which the second-order nonlinearity is evaluated, was firstly introduced. The verification of the theoretical equation showed that the Maker-fringe theory was valid for Y-cut α-quartz but not for thermally/electrically poled tellurite glass. The difference was originated in the non-uniform d-value distribution. The second-order nonlinearity induced by thermal/electrical poling was localized beneath the anode-side surface. At the intermediate between the activated and the non-activated regions, d-value decays gradually and not in a stepwise way. To characterize such non-uniform d-value, modified Maker-fringe theory was introduced. The modified Maker-fringe pattern drastically increased the goodness of fit with the experimental.

In section 1.2, second-order nonlinearity was induced into $15Nb_2O_5 \cdot 85TeO_2$ glass by inhomogeneous doping of a trace amount of sodium-ion. The thermal/electrical poling with a sample contact on sodium borosilicate glasses brought about the injection of sodium-ions at the anode-side surface, which led to the construction of a frozen-in electrostatic field $\mathbf{E}_{dc}$. A detailed analysis of the Maker-fringe patterns for the sodium-implanted samples revealed that SHG-active region beneath the anode-side surface expanded with the increase in poling temperature, and above 270 ˚C, it became substantially constant. On the other hand, d_{33} at the anode-side surface ($d_{33}(0)$) attained the maximum when poled at 250 ˚C. An electrochemical approach confirmed that $d_{33}(0)$ was linearly related with Na/Te at the anode-side surface. These results supported the effectiveness of sodium-ion implantation on $\chi^{(2)}$-induction.

Summary

In section 2.1, the internal poling of vanadium-doped tellurite glasses was demonstrated using a sinusoidal DC field designed by ω and 2ω beams of a Nd:YAG laser (optical poling). The period of the DC field satisfying a pseudo-phase matching condition led to a large SH output. In optically poled $15Nb_2O_5 \cdot 85TeO_2$ glass, output SH intensity increased with the increase in V_2O_5-concentration, which indicated that vanadium ions played an important role in the $\chi^{(2)}$-induction. For K_2O-Nb_2O_5-TeO_2 system, SH intensity took a maximum when K_2O content was 5.00 mol%. From ESR spectroscopy, it revealed the existence of tetravalent vanadium ions in the tellurite glass matrices and its oxidation caused by the 2ω beam irradiation. The laser-induced oxidation was due to a photochemical reaction from tetravalent to pentavalent state, leading to the generation of one electron. The optically encoded polarized structure was found to be constructed by the orientation of the positive hole at tetravalent vanadium ion and the electrons released by the photochemical reaction.

In section 2.2, V-Tb co-doping was attempted for $15Nb_2O_5 \cdot 85TeO_2$ glass to enhance the output SHG accomplished by optical poling. The SH intensity from the co-doped sample exceeded that for the samples doped only with vanadium ions. From the fact that the sample containing only terbium ions scarcely exhibited SHG, it is speculated that terbium ions had a role of charge-trap site. Also, terbium ions show little absorption at the visible region longer than 450 nm, leading to the reduction of re-absorption of generated SH wave.

In chapter 3, space-selective precipitation of second-order nonlinear optical crystals inside some silicate glasses was demonstrated using tightly-focused femtosecond-laser pulses with a near-infrared wavelength. Intense blue light corresponding to the second-harmonic wave of the incidence was confirmed in response to the precipitation of the crystals. Electron probe microanalysis revealed that the chemical composition in the vicinity of the laser-focal region had a radial profile from the focal center to the outside. The local composition change and the resultant crystallization can be explained from the viewpoint of thermal and chemical gradient induced by microexplosion. Therefore, irradiation period necessary for the precipitation depends on the thermal stability of the original glass.

The present dissertation has focused on the construction of polarized structure inside inorganic oxide glasses and on the nonlinear optical properties provided by the induced structure. The author believes that the polarization techniques treated here contribute to future electronic/optical-material design.

List of publications

Chapter 1

Section 1.1

"Effect of sodium-ion doping on second-order nonlinearity in tellurite glass"

Yoshinori Yonesaki, Takahiro Takei, Nobuhiro Kumada, Nobukazu Kinomura, Katsuhisa Tanaka and Kazuyuki Hirao

to be submitted to Journal of Applied Physics.

Section 1.2

"Relaxation phenomena in second-order nonlinearity of thermally and optically poled Nb_2O_5-TeO_2 glasses"

Yoshinori Yonesaki, Katsuhisa Tanaka, Aiko Narazaki, Jinhai Si and Kazuyuki Hirao

Journal of Physics D: Applied Physics, 35 (2002) pp. 2026-2031.

"Poling-induced structural change and second-order nonlinearity of Na^+-doped Nb_2O_5-TeO_2 glass"

Katsuhisa Tanaka, Aiko Narazaki, Yoshinori Yonesaki and Kazuyuki Hirao

Journal of Physics: Condensed Matter, 12 (2000) L513-L518.

"Second-harmonic generation in thermally/electrically poled transparent $BaTiO_3$ thin films prepared by dip-coating method"

Iwao Sakaihara, Katsuhisa Tanaka, Takashi Wakasugi, Rikuo Ota, Yoshinori Yonesaki and Kazuyuki Hirao

Materials Science Research International, 8 (2002) pp. 85-86.

Chapter 2

Section 2.1

"Second-harmonic generation in optically poled tellurite glasses doped with V_2O_5"

Yoshinori Yonesaki, Katsuhisa Tanaka, Jinhai Si and Kazuyuki Hirao

Journal of Physics: Condensed Matter, 14 (2002) pp. 13493-13503.

"Second-harmonic generation in optically poled Y52 filter glass"

Katsuhisa Tanaka, Yoshinori Yonesaki, Jinhai Si and Kazuyuki Hirao

Optics Communications, 225 (2003) pp. 387-391.

Section 2.2

"Enhancement of optically encoded second-order nonlinearity in $15Nb_2O_5 \cdot 85TeO_2$ glass by doping with V and Tb"

Yoshinori Yonesaki, Katsuhisa Tanaka and Kazuyuki Hirao

Journal of the Ceramic Society of Japan, 114 (2006) pp. 110-113.

Chapter 3

"Precipitation of second-order nonlinear optical crystals inside silicate glasses by femtosecond laser irradiation"

Yoshinori Yonesaki, Kiyotaka Miura, Ryuhei Araki, Koji Fujita and Kazuyuki Hirao

Proceedings of XX International Congress on Glass (2004) O-08-013.

"Space-selective precipitation of non-linear optical crystals inside silicate glasses using near-infrared femtosecond laser"

Yoshinori Yonesaki, Kiyotaka Miura, Ryuhei Araki, Koji Fujita and Kazuyuki Hirao

Journal of Non-Crystalline Solids, 351 (2005) pp. 885-892.

"Crystal structure of $BaCa_2MgSi_2O_8$ and the photoluminescent properties activated by Eu^{2+}"
Yoshinori Yonesaki, Takahiro Takei, Nobuhiro Kumada and Nobukazu Kinomura
Journal of Luminescence, 2008, in press

"Crystal structure of Eu^{2+}-doped $M_3MgSi_2O_8$ compounds and their emission properties"
Yoshinori Yonesaki, Takahiro Takei, Nobuhiro Kumada and Nobukazu Kinomura
to be submitted to Journal of Luminescence.

Acknowledgements

The present dissertation has been carried out under the direction of Professor Kazuyuki Hirao at Graduate School of Engineering in Kyoto University.

Many talented people enriched my life as a researcher, and any effort to mention all who contributed to this dissertation remains incomplete. However, the author is grateful for the opportunity to mention at least a few of them by name. First of all, the author wishes to express his sincere gratitude to Professor Kazuyuki Hirao for his continuous encouragement, guidance and valuable advice all through the duration of the present work. He has been a constant source of inspiration in the field of research. He has showed me how to present results in a more appealing way. His generous support gave me the opportunity to present my research results at various conferences. The author would also like to express his grateful appreciation to Professor Katsuhisa Tanaka at Graduate School of Engineering in Kyoto University for his priceless discussion and pertinent suggestions. Most part of the present dissertation is composed of the experimental results with the help of him. Many of his suggestions have influenced how I work, and I would not be where I am today without him. The author also thanks Associate Professor Kazuki Nakanishi and Associate Professor Koji Fujita in Kyoto University for their helpful suggestions and guidance on the present thesis. The suggestions from Professor Teiichi Hanada and Professor Toshinobu Yoko in Kyoto University are also gratefully acknowledged.

The author is particularly thankful to Dr. Jinhai Si, Dr. Aiko Narazaki and Dr. Jun Sasai whose help with preparing samples and measuring SHG was invaluable. Special thanks as well to Professor Jianrong Qiu, Associate Professor Kiyotaka Miura and Mr. Ryuhei Araki for providing kind help in using a femtosecond pulsed laser and for its maintenance. The experimental results with the help of them have made it into this dissertation. The author is deeply grateful for having had the opportunity to work with all the students and staffs in Hirao's laboratory. Thanks, especially, to Mr. Atsushi Itagaki, Dr. Kazuyoshi Kanamori, Dr. Masayuki Nishi and Mr. Takeshi Tamaoka for making my work enjoyable and for the many shared hours spent in Kyoto University. Special mention has to go to Ms. Miki

Tahara, Ms. Reiko Tomita and Ms. Yumi Ishikura for their administrative support and for many other things.

Finally, the author is greatly indebted to Professor Nobukazu Kinomura, Professor Nobuhiro Kumada and Dr. Takahiro Takei in University of Yamanashi for welcoming the author into their research group, their encouragement and experimental supports.

Kyoto, 2008 Yoshinori Yonezaki